ACOUSTIC EMISSION MONITORING OF REINFORCED CONCRETE SYSTEMS RETROFITTED WITH CFRP

by

Sandeep Degala

Bachelor of Engineering, Osmania University, 2006

Submitted to the Graduate Faculty of

Swanson School of Engineering in partial fulfillment

of the requirements for the degree of

Master of Science

University of Pittsburgh

2008

UNIVERSITY OF PITTSBURGH

SWANSON SCHOOL OF ENGINEERING

This thesis was presented

by

Sandeep Degala

It was defended on

March 24, 2008

and approved by

Dr. Kent A. Harries, Assistant Professor,
William Kepler Whiteford Faculty Fellow,
Department of Civil and Environmental Engineering

Dr. Julie M. Vandenbossche, Assistant Professor,
Department of Civil and Environmental Engineering

Thesis Advisor: Dr. Piervincenzo Rizzo, Assistant Professor,
Department of Civil and Environmental Engineering

ACOUSTIC EMISSION MONITORING OF REINFORCED CONCRETE SYSTEMS RETROFITTED WITH CFRP

Sandeep Degala, M.S.

University of Pittsburgh, 2008

Debonding of externally bonded carbon fiber reinforced polymer (CFRP) materials used for repair of reinforced elements is commonly observed and is often the critical limit state for such systems. This thesis presents an acoustic emission (AE) study performed during laboratory tests of concrete slab specimens strengthened with CFRP strips. Several specimens having different CFRP details were monitored. An AE paradigm to monitor damage initiation, progression, and location in the test specimens is demonstrated. An algorithm to classify the cracks in concrete, the disbond of the CFRP strips from the soffit of the slab, and the eventual failure (debonding or concrete shear) is also presented. The proposed general approach can be applied to large scale CFRP-concrete systems.

This thesis also presents an AE study carried out to characterize the loading to failure response of steel reinforcing bars of three different sizes (#4, #5, and #6) subjected to quasi-static tensile load.

TABLE OF CONTENTS

LIST OF TABLES

LIST OF FIGURES

ACKNOWLEDGEMENTS

I would like to express my sincere gratitude to Dr. Piervincenzo Rizzo, my academic advisor and thesis committee chair, for his continued support, guidance, encouragement and immense patience during the course of this research work. I am indebted to him for his timely advice and positive energy towards me throughout this journey at the University of Pittsburgh.

I am extremely thankful to Dr. Kent A. Harries for his advice, appropriate guidance, and getting me acquainted with the laboratory during the experimentation. I would also like to thank Dr. Julie M. Vandenbossche for her constructive input and contribution as my thesis committee member.

In addition, I would like to thank my fellow graduate student and best friend Mr. Karthik Ramanathan, for being with me for past six years in terms of help and advice. Special thanks to him for equally enduring all the concrete dust with me. Appreciation is also extended to Mr. Andrew Peck, Mr. Derek Mitch and Mr. Louis Gualtieri for all the help. Many thanks to Mr. Marcello Cammarata for all the help and support during my research period. I feel lucky and happy for having great lab mates, whom I cherish for the rest of my life.

I would like to express my gratitude to my parents for their hard work and continuous support, which helped me in pursuing higher studies. Special thanks to my Undergraduate College Professors and all my close friends for their constant support and encouragement throughout my educational endeavors.

And finally, I thank the Almighty for guiding me in the right direction and blessing me with all the good fortune to accomplish my dreams.

NOMENCLATURE

ACI	American Concrete Institute
AE	Acoustic Emission
ASTM	American Society for Testing and Materials
b_f	width of FRP strip
CFRP	carbon fiber reinforced polymer
DWT	draw wire transducers
FRP	fiber reinforced polymer
HDT	hit definition time
HI	historic index
HLT	hit lockout time
IA	intensity analysis
K, J	empirical constants based on material under investigation
N	number of hits up to time t
PA	parameter analysis
PCA	principal component analysis
PDT	peak definition time
PZT	piezo-electric transducer
RC	reinforced concrete
s	FRP spacing in slab systems
S_{oi}	signal strength of the i^{th} event

S_{om}	signal strength of the m^{th} hit, where order of m is based on signal strength magnitude.
S_r	severity index

This thesis reports all values in US units throughout and reports SI units in a secondary fashion. The following "hard" conversion factors have been used:

1 inch = 25.4 mm

1 kip = 4.448 kN

1 ksi = 6.895 MPa

Reinforcing bar sizes are reported using the designation given in the appropriate reference. A bar designated using a "#" sign (e.g.: #4) refers to the standard inch-pound designation used in the United States where the number refers to the bar diameter in eighths of an inch.

1.0 INTRODUCTION

Over the past two decades the field of structural repair and strengthening have received considerable emphasis due to the unavoidable aging of existing infrastructure and the need for upgrading structural elements to meet more stringent design requirements. In order to enhance the structural capability of reinforced concrete (RC) members, fiber reinforced polymer (FRP) composites showed promise. Carbon FRP (CFRP) laminates offer, for instance, superior performance in terms of corrosion resistance, environmental durability and stiffness-to-weight ratio over conventional steel plate retrofitting. Moreover, the ease of application makes CFRP extremely attractive for use in civil infrastructure applications, especially in cases where dead weight, space, or time restrictions exist.

In concrete rehabilitation applications, FRP laminates are externally bonded to the substrate structure by the wet lay-up method or by direct adhesive application of preformed strips. Alternatively, FRP sheets may be wrapped around RC elements. Although FRP retrofitting has been fairly well established on a structural basis, aspects related to materials selection and use, design detailing, fracture and failure mechanisms, and durability are still not well understood (Karbhari 2001).

The critical issue in concrete externally retrofitted with FRP is bond, or rather the mechanism of debonding, which represents the most commonly observed mode of failure (Oehlers 2004). Typical examples of defects at the bond interface are voids between the laminate and the substrate, and delaminations. Both defects may affect the integrity, performance, life expectancy (ACI 440.2R-02), and the flexural strength (Shih et al. 2003) of the retrofitted system. Defects may originate at the manufacturing process, during installation, or can be triggered by high temperature gradient during curing (Gros et al. 2000). They may also be the result of aggressive environmental conditions.

To ensure the proper functioning of concrete systems reinforced with CFRP, an efficient and accurate nondestructive testing (NDT) technique is necessary to detect damage at the earliest possible stage.

Active NDT techniques such as infrared thermography, microwave testing, and ultrasonic testing have been used in RC members retrofitted with FRP.

In this thesis however a passive NDT method based on the acoustic emission (AE) principle is proposed. In general, AEs are defined as "the class of phenomena whereby transient elastic waves are generated by the rapid release of energy from localized sources within a material" (ASTM E1316). The elastic energy propagates as a stress wave (AE event) in the structure that is detected by one or more sensors attached to or embedded in the structure. AE differs from most other NDT techniques in two key respects. First, the signal has its origin in the material itself, not in an external source. Second, AE detects movement, while most other methods detect existing geometrical discontinuities. Different AE sources may produce different AE waveforms. The AE source mechanism results in different received signals if the source is oriented differently with respect to the geometry of the medium or the propagation path to the detector.

The study carried out in this thesis is aimed at developing three AE analysis approaches devoted to the detection, location, and classification of the different failure mechanisms in RC members retrofit with CFRP strips. These approaches are the parameter analysis (PA), the intensity analysis (IA), and the principal component analysis (PCA). Moreover, the PA and IA approaches were used to characterize the failure mechanisms in steel rebar during tensile loading to failure tests.

1.1 THESIS OUTLINE

This thesis comprises of eight chapters. Following this introductory chapter, Chapter 2 contains a detailed discussion on the background of failures occurring in concrete systems externally bonded with FRP

materials and a review of the nondestructive evaluation (NDE) methods proposed for such systems. Chapter 3 contains an introduction to the AE technique and a detailed literature review of a few data analysis practices used for CFRP bonded concrete members. Chapter 4 details on the experimental program conducted in this study. The experimental results from the monitoring of the RC systems retrofitted with CFRP are presented in Chapter 5 and thoroughly discussed in Chapter 6. The experimental setup and results from monitoring the steel rebar are presented and discussed in Chapter 7. Finally, the work's summary along with the recommendations for future research constitutes Chapter 8.

2.0 REINFORCED CONCRETE RETROFITTED WITH CFRP

The following sections provide a literature review of the failure mechanism in RC slabs retrofitted with CFRP and the NDE techniques employed to inspect/monitor these structures.

2.1 LIMIT STATES

Failure of FRP strengthened RC flexural members may take place through one or more mechanisms depending on the member and strengthening parameters (Buyukozturk et al., 2004). The typical failure modes of beams or slabs can be classified into seven main categories:

(a) flexural failure by FRP rupture;

(b) flexural failure by crushing of compressive concrete;

(c) shear failure;

(d) concrete cover separation;

(e) plate end interfacial debonding;

(f) intermediate flexural crack induced by interfacial debonding;

(g) intermediate flexure-shear crack induced by interfacial debonding.

Mode (a) failure can result in sudden and catastrophic failure of the member. Plate end interfacial debonding failures occur due to high interfacial shear and normal stresses that result near the end of the retrofitting plate. When these stresses exceed the strength of concrete, debonding propagates from the plate end with a thin layer of concrete remaining attached to the debonded strip. Often, the failure plane

will migrate to the first layer of internal reinforcing steel resulting in complete cover concrete delamination reminiscent of a splitting failure. When a flexure (b) or flexure-shear crack (c) is formed in the concrete, the tensile stresses released by the cracked concrete are transferred to the FRP strips. As a result, high local interfacial Mode-II (shear) stresses between the CFRP strips and the concrete are induced adjacent to the crack. At a flexure-shear crack in the shear span, additional Mode I (peeling) stresses are developed at the crack opening (tensile on the side of the crack having "lower moment" and compressive on the other side). As the applied loading increases, the tensile stresses in the CFRP strip and the interfacial Mode-I and II stresses between the CFRP strip and the concrete near the crack also increase. When these stresses reach critical values, debonding initiates at the crack and propagate in the direction of decreasing moment gradient, i.e. towards the nearest support. CFRP debonding will occur in sudden bursts and not as a continuous process (Giurgiutiu et al., 2003). It will usually initiate in areas of stress concentrations, which are commonly due to material inconsistencies and/or the location of existing cracks in the concrete substrate. Figure 2-1 shows the behavior of a flexural member having bonded reinforcement on the soffit. Generally, modes (d) and (e) are referred to as plate end debonding failures. Mode (f), although theoretically possible is not observed in practice. Mode (g) occurring in the shear span is always observed to dominate over mode (f) (Oehlers 2006).

.

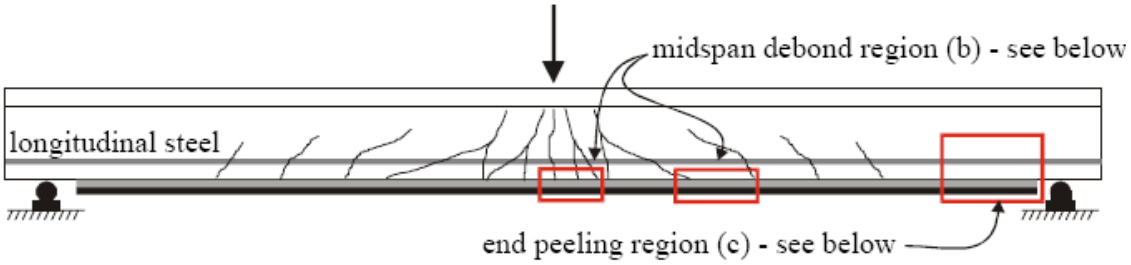

(a) behavior of flexural member having bonded reinforcement on soffit

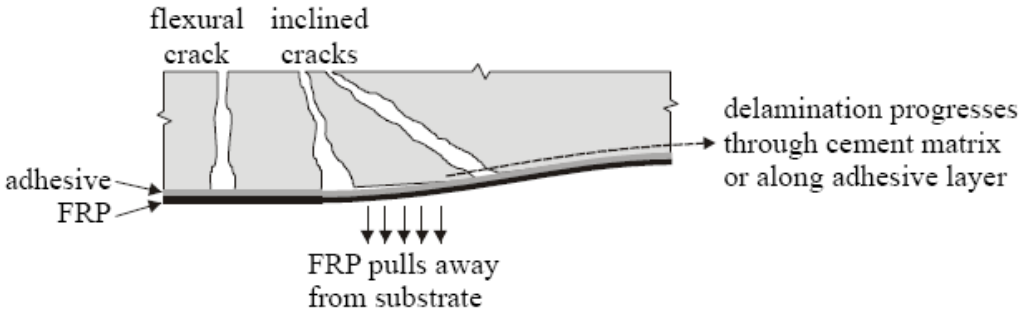

(b) midspan debond initiated by flexural and/or shear cracks

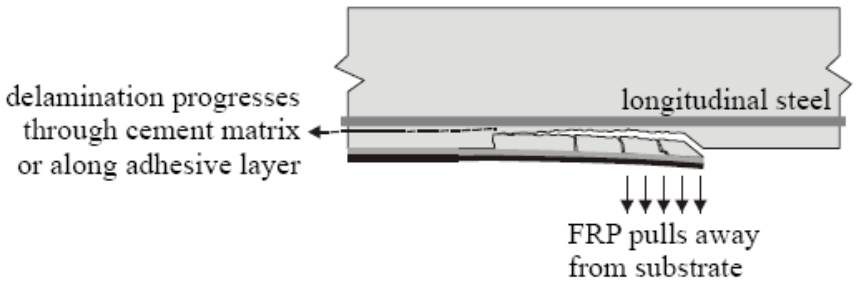

(c) end peeling initiated high bond shear stresses at end of bonded reinforcement

Figure 2-1 Failure mechanisms in RC systems reinforced with externally bonded CFRP (figure adapted from Aidoo, 2004 and modified)

2.2 INSPECTION METHODS

In the last decade different approaches have been proposed to inspect the bond between CFRP and concrete. Infrared thermography (IRT) has been used to monitor FRP wrapped reinforced concrete

columns of a bridge structure (Jackson et al. 2000). The IRT technique is found to be effective in detecting disbonds, blisters, and delaminations but not reliable on the identification of defects located deep within concrete. The IRT technique has also been used to detect delaminations in composite-concrete bondlines (Nokes et al. 2001, Hu et al. 2003). Nokes and co-authors also performed field-testing on two concrete deck bridges. The bond characteristics between FRP composites and concrete on small scale specimens, and on full scale AASHTO Type II girders using active IRT were evaluated (Brown et al. 2003). This study is found to have shown good potential in evaluating bond between FRP systems and concrete. Active thermographic approach has been used to (a) detect the artificially induced blisters in the bond-line between FRP components and the RC beams and (b) evaluate the influence of air-voids on the flexural performance of FRP strengthened RC elements (Shih et al. 2003). Digital infrared thermography has been used for subsurface defect detection in FRP bridge decks (Halabe et al. 2007). Air-filled and water-filled debonds and simulated subsurface delaminations are created at the flange-to flange junction between two FRP deck modulus. Surface temperature–time curves were established for different sizes of delaminations and debonds. However this method suffered limitations from accuracy of the pixel resolution of the infrared camera in detecting the boundaries of the delaminations.

Microwave testing has been used for the detection of disbonds and delaminations between CFRP laminate and the concrete substrate (Buyukozturk et al. 2003, Ekenel et al. 2004, Akuthota et al. 2004, and Stephen et al. 2004). Akuthota and co-authors introduced defects of various size, geometry, and thickness by injecting air between the CFRP laminate and mortar substrate. The microwave testing is found to be effective in detecting the disbond regions but experienced signal scattering by individual aggregates in concrete substrates and also the presence of reinforcing steel rebars caused hindrance in using this technique. Buyukozturk and co-authors inspected FRP-reinforced RC panels artificially damaged during the manufacturing process. The air voids in the FRP-concrete region were detected using data focusing scheme and image reconstruction algorithm. The FRP layers in the images were not shown well due to the maximum frequency used for detecting the voids. Ekenel and co-authors monitored the influence of cyclic loading on delaminations in RC beams fabricated and strengthened with CFRP

laminates. By applying pressured air beneath CFRP sheets, the delaminations were created when the epoxy was in a fresh state. In this study, the scanning images from microwave testing could detect the delaminations but failed to give an idea of the magnitude of the delamination size. Finally, Stephen and co-authors detected delaminations in CFRP concrete members in a bridge. A number of artificial delaminations were manufactured in these laminates by injecting air between the concrete substrate and the CFRP laminates when the epoxy adhesive was in its fresh state. The capability of microwave testing method to provide quick and informative images of the bonded CFRP abutment (in-field) was clearly demonstrated.

Methods based on the propagation of stress waves were used to inspect RC retrofitted with FRP. These methods can be classified in active (ultrasonic testing) and passive (AE). An ultrasonic pulse echo technique was used (Bastianini et al. 2001) to inspect composite materials (CFRP and GFRP) applied to different substrates (concrete, masonry, polyurethane). The authors measured the amplitude echo reflected from the interface between the FRP and the underlying material. Acousto-Ultrasonic technique has been used for inspection of FRP wrapped concrete structures for identifying the artificially created delaminations in the FRP and disbonds between concrete and FRP (Godinez-Azcuaga et al. 2004). Cracks were introduced in the concrete by three-point bending before applying the FRP wrap. Ultrasonic pulse velocity (UPV) has been used to quantify the extent and progression of damage in concrete filled FRP-tubes (Mirmiran et al. 2001). A structural health monitoring scheme has been demonstrated using piezoelectric transducers and the CFRP strip as a wave guide to identify CFRP-debonding (Giurgiutiu et al. 2003, Kim et al. 2007).

Acoustic Emission (AE) testing is a passive inspection technique employed to monitor the behavior of materials (structures) under deformation. The applicability of AE technology to hybrid CFRP tubes filled with concrete (hybrid columns) and to correlate the AE parameters to the state of stress in concrete was investigated by Mirmiran et al. (1999). The AE signatures of hybrid columns were studied over 40 specimens with different lengths, cross sections, jacket types, and jacket thicknesses. AE tests were combined with three series of feasibility experiments on concrete-filled FRP tubes and fiber-

wrapped columns i.e., length effect series, shape effect series and bond effect series. The specimens were loaded to failure to monitor their entire AE signature at various stages of loading. The study showed that (1) rate of change of cumulative AE counts with respect to the applied load correlates well with the degree of damage sustained by the concrete core; (2) longer specimens, thicker jackets, and un-bonded tubes display higher AE activities; and (3) the Kaiser effect (described in section 3 of this thesis) was not present in hybrid columns. AE was used to monitor six full scale glass FRP bridge deck panels with nominal cross-sectional depths varying from 152 mm (6 in.) to 800 mm (30 in.) (Gostautas et al. 2005). A special loading profile consisting of load increases, holds, and load decreases was applied to assess certain AE signature characteristics, such as the Kaiser effect and the Felicity ratio. These characteristics along with intensity analysis (IA) were investigated for use in damage evaluation of FRP composite structures. Very recently a case study concerning both numerical modeling and in-situ monitoring of a retrofitted RC beam with non-rectangular cross section was presented (Carpinteri et al. 2007). AE was used to investigate the beam's creep effects and micro-cracking phenomena before retrofitting. After retrofitting the beam with CFRP sheets a load to failure test was performed in order to monitor the crack propagation and CFRP debonding by means of AE.

3.0 ACOUSTIC EMISSION (AE)

3.1 BACKGROUND

As introduced in Chapter 1, an AE is a transient elastic wave generated by the rapid release of energy from a localized source or sources within a material (ASTM E 1316). Such sources are produced by moving dislocations, crack onset growth and propagation, plastic deformation, or by some change in the internal structure of the material. In materials like CFRP sources of emissions can be fiber breakage, matrix cracking, delamination, fiber pullout, or stress redistribution.

The AE activity is used as a qualitative indication to identify some damage or degradation. For this approach to be successful, it is critical that little or no extraneous noise such as electro-magnetic interference exist. Early studies performed by Kaiser (1950) demonstrate that AE is an irreversible phenomenon. He showed that many materials under load in the elastic regime emit acoustic waves only after a primary load level is exceeded. This particular behavior is known as Kaiser Effect and it is defined as the absence of detectable acoustic emissions at a fixed sensitivity level, until previously applied stress levels are exceeded (ASTM E1316-05b). On contrary, the presence of detectable acoustic emissions at a fixed sensitivity level with stress levels below those previously applied is defined as Felicity Effect (ASTM E1316-05b). If the Kaiser effect is permanent for a certain material, very little or no AE will be recorded before the previous maximum stress level is reached. Above the previous maximum value, existing damage may propagate or new damage may initiate, both of which produce AE.

The typical behavior of a material that experiences the Kaiser effect is shown in Figure 3-1 that schematizes the cumulative number of AE events as a function of the applied load. Emissions are

observed upon initial loading from 1 to 2, but not upon unloading (2 to 3). Upon reapplying the load, there is no emission (line is horizontal) until 2 is reached again; this is due to the Kaiser Effect. The load is increased to 4, with more emission, and another unload-reload cycle is applied. On raising the load again for the last time, significant emissions begin to emit at point 6, below the previous maximum load. This behavior is known as the Felicity Effect.

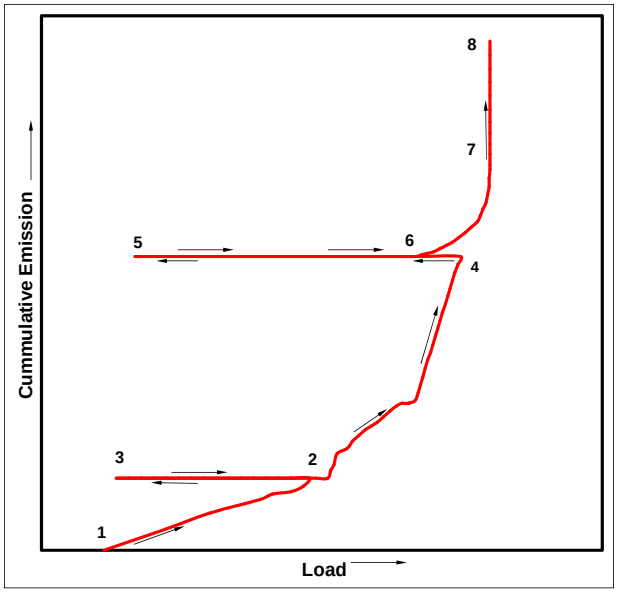

Figure 3-1 Cumulative number of AE events as a function of applied load.

3.2 INSTRUMENTATION AND EQUIPMENT

The main elements of a modern AE instrumentation system are shown schematically in Figure 3-2 and they consist of:

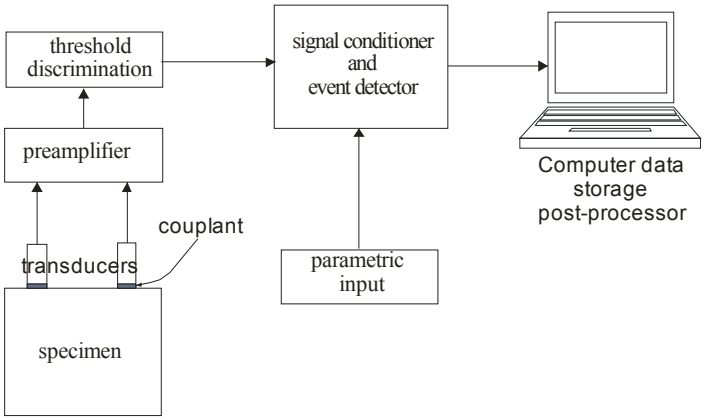

Figure 3-2 Elements of modern AE detection system.

1. ***AE sensors*** that detect the propagating stress waves and convert the surface displacements associated with the elastic waves into electric signals.
2. ***Preamplifiers*** that provide gain to boost signals amplitude.
3. ***Data acquisition system*** that digitizes the analog signals and allows the real-time processing of AE waveforms.
4. ***Dedicated software*** that allows to manage all the acquisition, graphing and analysis of the AE system. In this study the PAC AEwin 2.1 software was used.

3.3 DATA ANALYSIS APPROACHES

The main objectives of AE are the detection, characterization, and location of an event. In order to accomplish one or more of these objectives several methods of AE analysis have been proposed. The parameter analysis (PA) is the most traditional approach. Other approaches combines the PA with advanced signal processing like wavelet transforms (Mizutani et al. 2000, Qi 2000), neural networks

(Chen et al. 2000, Huguet et al. 2002), "b-value analysis" (Colombo et al. 2003), and moment tensor inversion (Grosse et al. 2003).

In this thesis the results from three analysis methods are presented, namely PA, intensity analysis (IA), and Principal Component Analysis (PCA). The parameter analysis evaluates AE features such as counts, amplitude, risetime, energy to identify the AE's source and to locate the origin of such source by using mathematical methods based on the arrival time of the ultrasonic signal. IA evaluates the structural significance of an event by calculating two values called historic index and severity and evaluating their change in time. Finally, the PCA is a statistical approach, generally used for data reduction that projects a data vector into a new set of Cartesian coordinates called the principal components (Rippengill et al. 2003).

For the sake of completeness, a basic overview of each of these three analysis methods is provided.

3.3.1 Parameter Analysis (PA)

A typical AE signal is shown in Figure 3-3. In the PA, carried out in this study the signal features adopted are defined as (PAC μDiSP with AEwin user's manual, 2005):

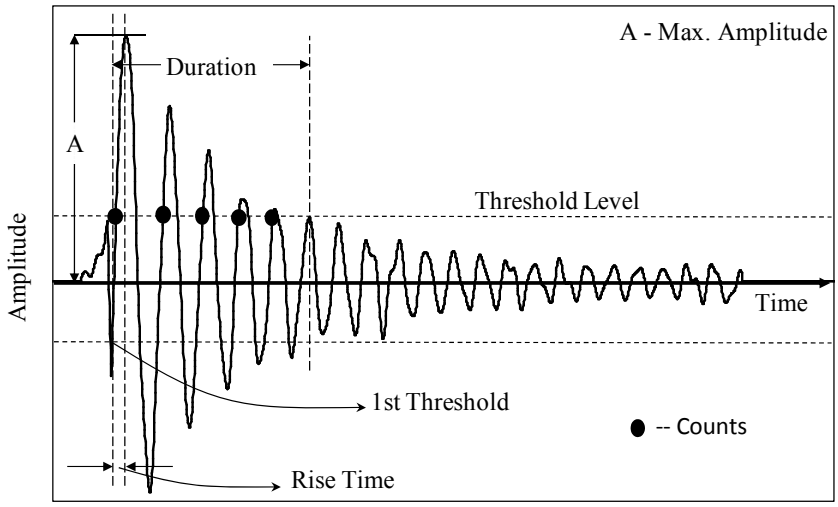

Figure 3-3 AE signal features

1. ***Amplitude*** is the peak voltage measured in a waveform and is typically expressed in decibels (dB).
2. ***Risetime*** is the time interval between the first threshold crossing and the maximum peak amplitude of the AE waveform.
3. ***Duration*** is the time difference between the first and last threshold crossings.
4. ***Energy*** is the measured area under the envelope of the rectified linear voltage time signal from the transducer.
5. ***Counts*** are the number of pulses emitted by the measurement circuitry if the signal amplitude is greater than the threshold.
6. ***Peak frequency*** is defined as the point in the power spectrum at which the peak magnitude occurs.
7. ***Centroidal frequency*** is the result of the following algebraic computation:

   Centroidal frequency = Σ (FFT amplitude*frequency)/ Σ (FFT amplitude)

8. ***Signal strength*** is mathematically defined as the integral of rectified voltage signal over the duration of the AE waveform packet.

3.3.2 Intensity Analysis (IA)

This technique evaluates the structural significance of an event as well as the level of deterioration of a structure by calculating two values called the historic index (HI) and severity (S_r) (Fowler et al. 1989, 1992, Gostautas et al. 2005). The HI compares the signal strength of the most recent emissions to the signal strength of all emissions, which means estimating the slope changes in the plot of the cumulative signal strength (CSS) as a function of time. The presence of one or more peaks in the plots HI vs. time may reveal the occurrence of new damage or the propagation of damage, respectively. The severity is the average of the *J* largest signal strength emissions. As the severity is a measure of structural damage, an increase in severity often corresponds to new structural damage. Analytically, the HI and the S_r are defined, respectively, as:

$$HI = \frac{N}{N-K}\left(\frac{\sum_{i=K+1}^{N} S_{oi}}{\sum_{i=1}^{N} S_{oi}}\right) \tag{3.1}$$

$$S_r = \frac{1}{J}\left(\sum_{m=1}^{J} S_{om}\right) \tag{3.2}$$

where

N is number of hits up to time t;

S_{oi} is the signal strength of the i^{th} event;

K and J are empirical constants based on the material under investigation (Fowler et al. 1992).

S_{om} – signal strength of the m^{th} hit, where order of m is based on signal strength magnitude.

For composites, *K* values are related to *N* by the relations: For $N \leq 100$, *K* is not applicable; for $101 < N < 500$, $K = 0.8 \cdot N$; and for $N > 500$, $K = N - 100$. And *J* values for $N \leq 20$, *J* is not applicable, and for $N > 20$, $J = 20$. (Gostautas et al. 2005).

By plotting the maximum values of the HI and S_r the intensity chart is obtained for any given AE sensor Intensity values of high structural significance will plot toward the top right-hand corner of the chart while values of less significance near the bottom left. A typical "intensity chart" for metal piping is shown in Figure 3-4.

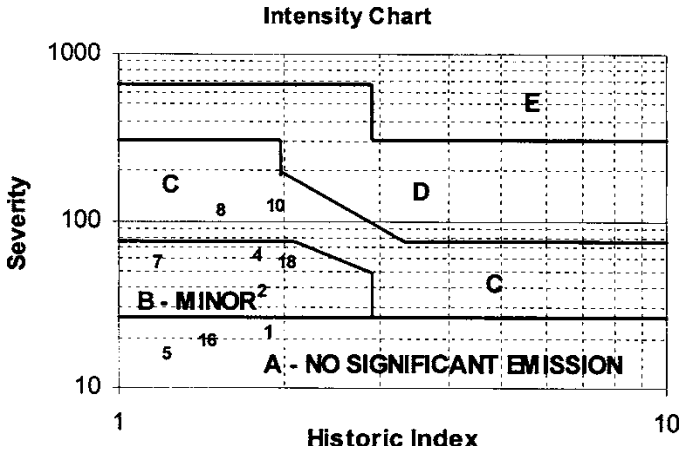

Figure 3-4 Typical intensity chart for metal piping systems (Gostautas et al. 2005)

The chart is divided into intensity zones A to E. The structural significance of the zones identified in Figure 3-4 is described and summarized in Table 3-1. The numbers shown on the chart represent the AE sensor channels

Table 3-1. Significance of intensity zones (Gostautas et al. 2005)

Zone Intensity	Recommended action
A – No significant emission	Insignificant acoustic emission. No follow-up recommended.
B – Minor	Note for reference in future tests. Typically minor surface defects such as corrosion, pitting, gouges, or cracked attachment welds.
C	Defect requiring follow-up evaluation. Evaluation may be based on further data analysis, or complementary nondestructive examination.
D	Significant defect requiring follow-up inspection.
E	Major defect requiring immediate shut-down and follow-up inspection.

3.3.3 Principal Component Analysis (PCA)

PCA is a mathematical approach used to reduce the dimensionality of a data set for compression, pattern recognition and data interpretation (Manson et al. 2001, Mustapha et al. 2005, and Mustapha et al. 2007). The principal components algorithm seeks to project by a linear transformation, the data into a new q-dimensional set of Cartesian coordinates (z_1, z_2. . . z_n). The new coordinates have the following property: z_1 is the linear combination of the original x_i with maximal variance; z_2 is the linear combination, which explains most of the remaining variance and so on. It should be clear, that if the p-coordinates are actually a linear combination of $q<p$ variables, the first q principal components will completely characterize the data and the remaining p–q will be zero. In practice, due to measurement uncertainty, the principal components will all be non-zero and the user should select the number of significant components for retention. (Sharma 1996)

Calculation is as follows, where $\{x\}$ and $\{z\}$ denote vectors in the measured and reduced space respectively,

Given data $\{x\}_i = (x_{1i}, x_{2i}, \ldots\ldots, x_{pi})$, $i = 1,2,\ldots,N$, form the Covariance Matrix $[\Sigma]$,

$$[\Sigma] = \sum_{i=1}^{N} (\{x\}_i - \{\bar{x}\})(\{x\}_i - \{\bar{x}\})^T \tag{3.3}$$

and decompose so,

$$[\Sigma] = [A][\Lambda][A]^T \tag{3.4}$$

where $[\Lambda]$ is diagonal. (Singular value decomposition can be used for this step.) The transformation to principal components is then,

$$\{z\}_i = [A]^T (\{x\}_i - \{\bar{x}\}) \tag{3.5}$$

where $\{\bar{x}\}$ is the vector of means of the x-data.

Considered as a means of dimension reduction, PCA works by discarding those linear combinations of the data which contribute least to the overall variance or range of the data set.

3.4 AE FOR CONCRETE RETROFITTED WITH CFRP

The heterogeneous composition of RC constitutes a challenge for all ultrasound-based testing methods (Schechinger et al. 2006). The detection of AE in RC slabs retrofitted with CFRP strips is even more complex. Both RC and fiber composites release discrete bursts of AE energy when undergoing stress. AE sources in concrete may include micro cracking, cracking, friction associated with aggregate interlock, and debonding of aggregate and mortar (Chen et al. 2000). Also AE sources in RC systems can be from rebar bond failure and rupture due to the interaction of concrete with steel reinforcement. AE sources in composites may include debonding between the matrix and the fibers, matrix cracking, delamination, and fiber breakage (Rizzo et al. 2001). In RC systems retrofitted with CFRP, other sources of AE are associated with the debonding phenomenon as discussed in Chapter 2.

The AE event may be originated in one of the following: the internal steel reinforcement, the inner concrete, the concrete surface, the CFRP strip, or the adhesive layer. A stress wave originating in the slab propagates as a bulk wave with velocity independent of the wave frequency; at the interface between the concrete and the strip, the bulk wave is partially reflected back into the slab and is partially refracted into the CFRP. If the AE signal is generated instead on the slab surface, the wave travels as a surface (Rayleigh) wave and at the interface with the strip, part of the wave motion is converted into a guided wave. If the AE event is generated in the steel reinforcement, the CFRP strip, or the adhesive layer, it propagates as a guided wave in that medium. Wave motions in a waveguide are dispersive (frequency dependency of the wave velocity and attenuation), and can propagate in symmetric and anti-symmetric modes. Moreover, the characteristics of the wave propagating on the CFRP strip will also be dependent on the direction of the wave propagation with the respect of the fiber orientation.

4.0 EXPERIMENTAL PROGRAM

This section reports the testing preparation, i.e. the specimen casting, instrumentation, and the loading protocol.

4.1 SPECIMEN DETAILS

Nine reinforced concrete slab specimens were cast from a single batch of Portland Cement Concrete in the Watkins Haggart Structural Engineering laboratory at the University of Pittsburgh. The specimen details, CFRP application, and test setup were firstly reported in Ramanathan (2008) and are summarized here for completeness. The slabs were 50 in. (1270 mm) x 30 in. (762 mm) and 3 in. (76 mm) thick. The concrete had a measured 28 day compressive strength of 4860 psi (33.5 MPa). Details of the properties of concrete are presented in Table 4-1. Each slab contained seven #3 (9.5 mm diameter) longitudinal reinforcing steel bars at a spacing of 4 in. (100 mm) as primary flexural reinforcement.

Table 4-1 Concrete's properties.

Design Property	Value	Notes
Strength, *psi (MPa)*	5000 (34)	28 day cylinder strength = 4860 psi
Unit Weight, *pcf (kg/m^3)*	139.3 (2231.5)	
Slump, in. (mm)	5 (127)	pumpable
Entrained air	4-5 to 7.5%	

Additionally, four #3 transverse bars were provided to resist handling stresses due to inverting the slab for the application of CFRP. No additional shear reinforcement in the form of stirrups was provided. Details of the slab reinforcement are shown in Figure 4-1.

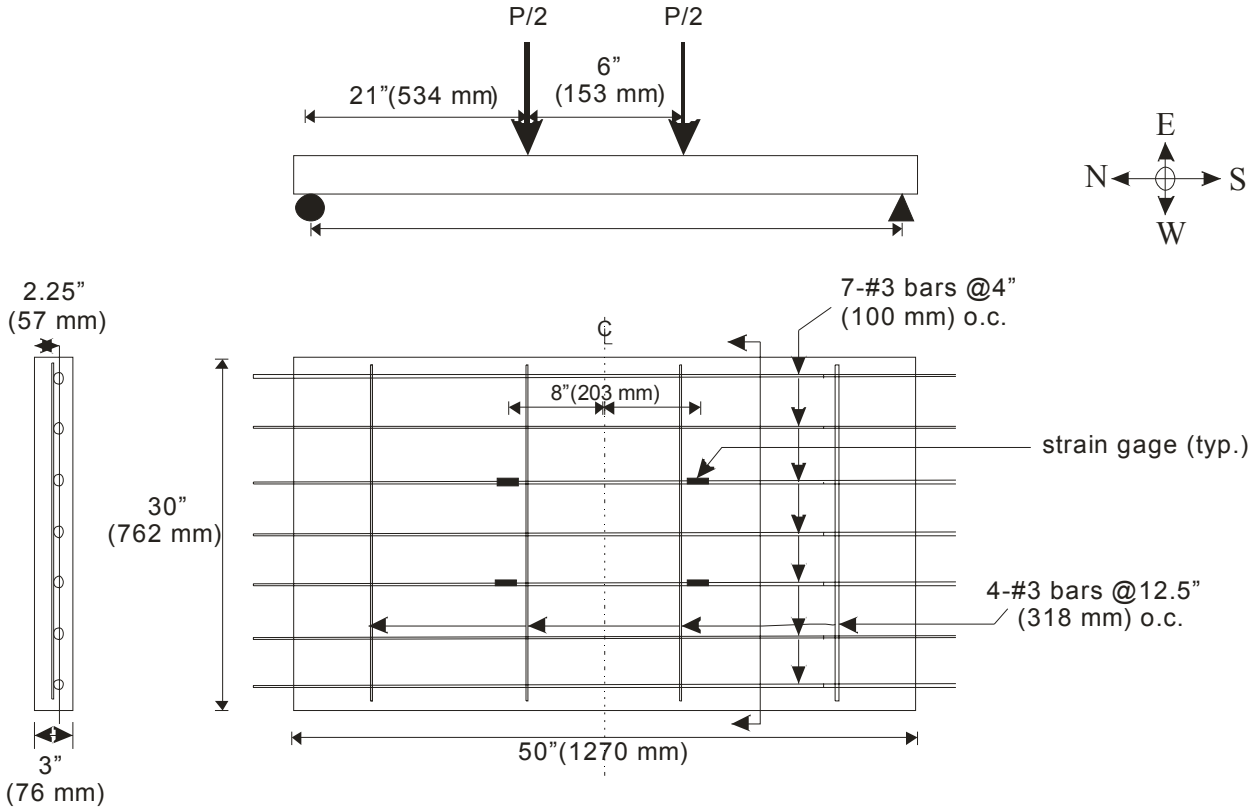

Figure 4-1 Details of slab reinforcement.

Figure 4-2a and Figure 4-2b show the picture of the formwork prior to casting and three slabs after casting.

The slabs were strengthened with various arrangements of CFRP strips. Commercially available 4 in. (102 mm) wide by 0.055 in. (1.4 mm) thick preformed unidirectional high strength CFRP composite strips were used (Fyfe, 2005). The CFRP properties reported by the manufacturer are given in Table 4-2.

(a) typical formwork

(b) three slabs after casting

Figure 4-2 Typical Formwork and casting of slabs

Table 4-2 Manufacturer's reported properties of CFRP strips (Fyfe Tyfo UC).

Property	ASTM Test Method	Fyfe Tyfo UC
Material Type	NA	High Strength Carbon
Tensile Strength, *ksi (MPa)*	D3039	405 (2800)
Tensile Modulus, *ksi (GPa)*	D3039	22500 (155)
Elongation at rupture, *in. (mm)*	D3039	0.018 (0.5)
Perpendicular Strength, *psi (Pa)*	D3039	negligible
Strip Thickness, *in. (mm)*	NA	0.055 (1.4)
Widths used in testing, *in. (mm)*	NA	4 (102); 2 (51); 1(25)

The adhesive used to bond the FRP to the concrete substrate was a two-part ambient cure epoxy (Fox Industries FX-776) formulated for bonding to concrete and steel substrates. Manufacturer reported material properties of the adhesive are given in Table 4-3.

Table 4-3 Properties of adhesive system used to bond the CFRP strips to the concrete substrate as reported from the manufacturer (FX 776).

Property	ASTM Test Method	FX 776
Tensile Strength, *psi (MPa)*		4500 (31)
Elongation at rupture, *in. (mm)*	D638	0.025 (0.7)
Tangent Modulus of elasticity, *ksi (GPa)*	D790	575 (3.9)
Thickness of application, *in. (mm)*	measured	approx. 0.1 (2.54)

All nine slabs were tested in a monotonic load-to-failure protocol under displacement control and monitored using an AE instrumentation suite. Each slab possessed a different CFRP strip geometry described by the ratio of CFRP width-to-CFRP spacing (b_f/s). Typical retrofitted slab specimens are shown in Figure 4-3.

(a) Specimen 2x2 (b) Specimen 2x4

Figure 4-3 Typical retrofitted slab specimen

The following notation is used to denote the slabs: the first number indicates the number of CFRP strips bonded to the slab and the second number represents the width (in inches) of each strip.

1 x 4 is a slab with one strip, 4 inches wide.

2 x 2 is a slab with two strips, 2 inches wide.

4 x 1 is a slab with four strips, 1 inch wide.

2 x 4 is a slab with two strips, 4 inches wide.

4 x 2 is a slab with four strips, 2 inches wide.

8 x 1 is a slab with eight strips, 1 inch wide.

3 x 4 is a slab with three strips, 4inches wide.

6 x 2 is a slab with six strips, 2 inches wide.

12 x 1 is a slab with twelve strips, 1 inch wide.

4.2 APPLICATION OF CFRP TO THE TEST SPECIMENS

4.2.1 Preparation of concrete surface and CFRP strips

To avoid failure at the adhesive-to-concrete interface it is essential to properly prepare the concrete surface. The formed soffit of each test slab was prepared using an angle grinder with a wire wheel attachment to remove all laitance and dirt from the working surface of the concrete. Compressed air was then used to remove any concrete dust and dirt that settled on the slab. Once the surface was clean, the edge lines for strip alignment were marked.

The CFRP strips were cut to lengths of 46 in. (1168 mm) so that they did not extend to or beyond the end supports of the slab. The strips were then cut longitudinally to widths of 2 in. (51 mm) and 1 in. (25 mm) using a utility knife. Once the CFRP was cut, it was cleaned and protected from dust, dirt, moisture and mechanical damage.

4.2.2 Application of CFRP

With the slabs inverted and having an unobstructed working surface on the (eventual) tension face of the beam, the retrofit process was begun. The adhesive was applied to the tension face of the slab using putty spatulas between the lines that were laid out for CFRP location. All possible care was taken to ensure that a uniform layer of adhesive was laid out. The adhesive was also applied in a similar fashion to one of the side of the CFRP strips. Each CFRP strip was then applied to the slab soffit. The strip was pushed firmly into the adhesive to remove any voids in the adhesive and assure a uniform application. Starting at the

center of the strips and moving outward toward the supports locations, the strips were pressed onto the concrete with uniform pressure from fingertips. The exposed (unbonded) side of the CFRP strips was protected with masking tape in order to keep it clean of adhesive for eventual application of strain gages. The cross section of nine retrofitted one way slabs are shown in Figure 4-4.

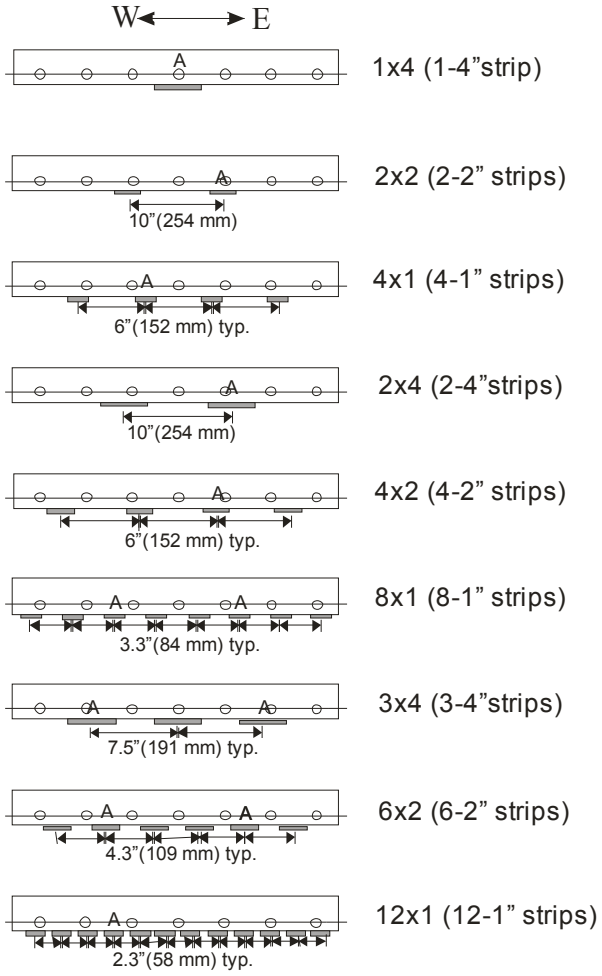

Figure 4-4 Cross section of the CFRP retrofitted slab specimens. (A – CFRP strip with AE sensors)

4.3 INSTRUMENTATION

An AE instrumentation suite from Physical Acoustics Corporation (PAC) was used to monitor the slabs under loading. The data acquisition board was a four-channel high speed PAC μDiSP (shown in Figure 4-5). Acquisition of acoustic emission signals and their digital processing was enabled with the implementation of the PCI/DSP cards in the μDiSP workstation. Broadband AE piezoelectric transducers (Physical Acoustics PICO transducers) used in conjunction with preamplifiers set at a 40 dB gain were used to detect the propagating waves. The AE sensors were attached to the strips using hot melt glue (Figure 4-6). A schematic picture of AE sensor placement on the CFRP strip is shown in Figure 4-7. The real-time monitoring of AE data was enabled by a laptop dedicated with AEwin v2.11 software provided by PAC for signal processing and storage.

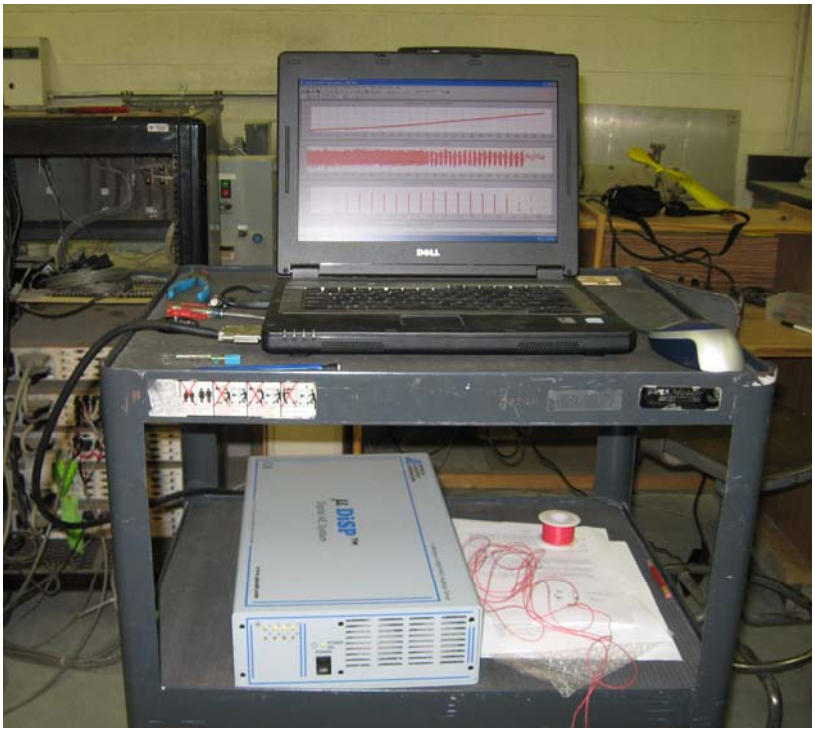

Figure 4-5 Four-channel Physical Acoustics μDiSP acquisition workstation

(a) Broad-band PICO sensor (AE) (b) AE sensors and strain gages

Figure 4-6 Details of the AE workstation and sensor employed.

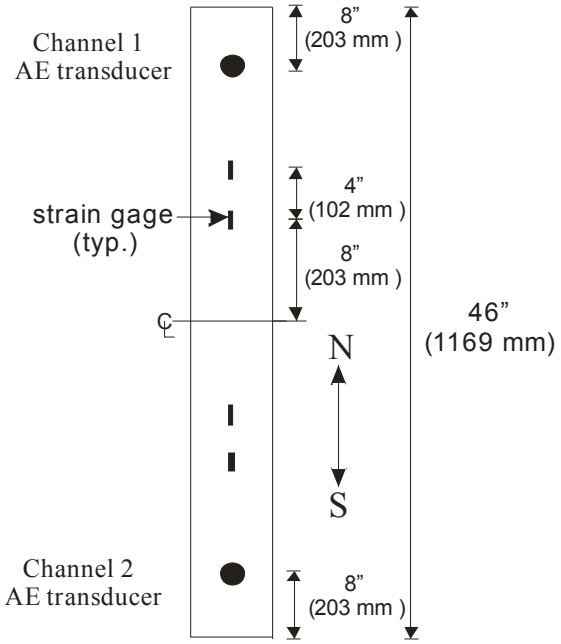

Figure 4-7 Instrumented CFRP strip

To conduct a successful AE monitoring certain parameters of the data acquisition systems need to be set according to the material being tested and the background noise level. Such settings are summarized in

Table 4-4 and were made to ensure adequate damage related acoustic signal capture. Acquisition threshold is a part of standard hardware setup which sets the detection threshold for the acquisition system, enabling reduction of background noise in the recorded data. HDT, PDT and HLT are all timing parameters of the signal acquisition process and have material specific values. HDT sets the extent of a signal to be accounted as one hit, PDT ensures the exact identification of signal peak and a proper HLT setting enables discarding of spurious signal decay measurements.

Table 4-4 AE Instrument settings

Parameter	Set Value
Acquisition Threshold	40dB
Peak Definition time (PDT)	300 μs
Hit Definition time (HDT)	600 μs
Hit Lockout time (HLT)	1000 μs

In order to determine the location of an acoustic event it is necessary to know and select the velocity of the stress waves in the material. For isotropic materials of bulk geometry this information can be calculated from stiffness and density properties, however for materials such as fiber composites, it is difficult to analytically determine the velocity. For instance, it is known, that bulk wave velocity in concrete is approximately 1.92 miles/sec (3.1 km/sec) but varies depending upon the concrete properties (Naik et al. 2004). In addition, the dispersive behavior (wave velocity is dependent on the frequency of propagation) of waves in waveguides like thin laminates complicates the selection of the wave velocity. In AE testing it is common practice to experimentally determine the velocity by measuring the time taken by a signal generated through the pencil lead break (PLB) The PLB is an established technique (ASTM E 2075) for generating a signal that is of similar amplitude and waveform to actual acoustic events. The procedure basically consists of breaking 0.3-0.5 mm pencil leads of 2.5 mm length at a 30 degree orientation to the surface and the amplitudes recorded at a given sensor are measured at different time intervals to ensure that the sensitivity at the sensor does not vary by more than 3dB. With this method, the

velocity of sound in the CFRP strip bonded to the concrete soffit was estimated to be approximately 0.62 miles/sec (1 km/sec). The PLB test was carried out before starting each test.

Electrical resistance strain gages (ERSG) were attached onto the CFRP strips and in the steel reinforcement. Strain gages were connected to a Vishay System 5100 Data Acquisition System. In this study, the data collected from these gages are used to compliment the results obtained from AE data where necessary. For more information on the placement, please refer to Ramanathan (2008) and Degala et al. (SPIE conf. 2008). Slab vertical displacement at midspan was monitored using two draw wire transducers (DWT) secured to the slab sides at mid-height. The Baldwin universal testing machine load cell, the two DWTs and all the AE sensors were connected to the AE data acquisition system.

4.4 TESTING PROTOCOL

All the slab specimens were tested in a monotonic load-to-failure protocol under a four point bending (flexural) load set-up. The test frame was mounted in a Baldwin universal testing machine (UTM) with a capacity of 200 kips (890 kN). Loading was applied at midspan using a system of two 1.5 in. (38 mm) diameter rollers spaced at 6 in. (152 mm) which loaded the slab uniformly across its entire width. The 30 in. (762 mm) wide by 50 in. (1270 mm) long one way slabs were simply supported over a clear span of 48 in. (1220 mm). Photographs of the test setup, support condition and instrumentation are shown in Figure 4-8.

(a) Overall test set-up

(b) Details of the loading arrangement

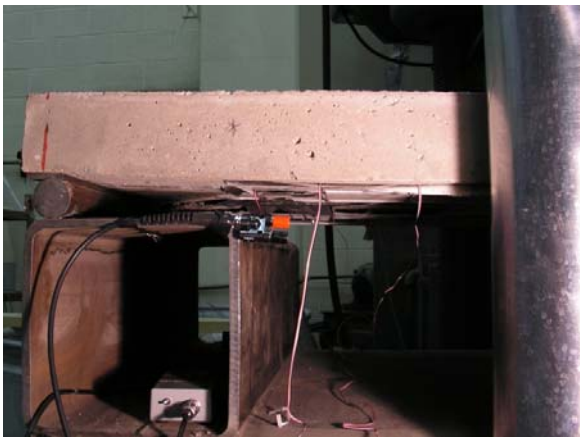

(c) Details of the support

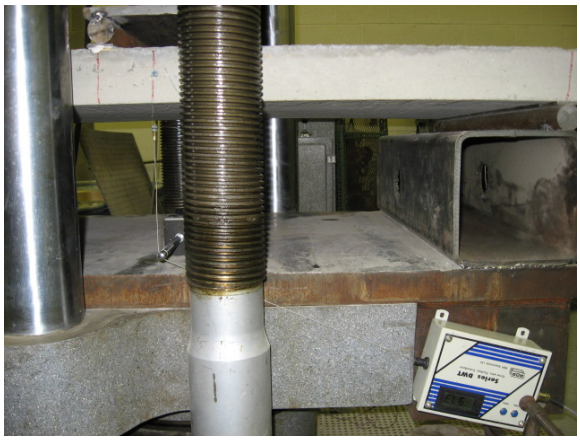

(d) Draw wire transducer details

Figure 4-8 Details of the test setup

The applied loading of the specimens in the Baldwin UTM was controlled manually under displacement control. Each monotonic test was completed at failure of the specimen. two main failure mechanisms were observed: debonding of the CFRP strip or shear failure of the concrete. Photos of these failures are

shown in Figure 4-9. For each specimen, the load at failure, the failure mode (debonding or shear), and the number of AE transducers used for monitoring are summarized in Table 4-5. Full details of the slab test program are reported by Ramanathan (2008). Typical representative failure modes observed from the CFRP slab specimens can be seen in Figure 4-9.

Table 4-5 Results showing ultimate load, failure type and number of sensors used for each slab specimen.

Slab No	Ultimate Load (UL) (kips)	Failure Type (through visual inspection)	Number of AE Transducers
1x4	13.44	Debonding	2
2x4	17.00	Shear	2
4x1	16.67	Debonding	2
8x1	22.00	Shear	4
2x2	14.80	Debonding	2
6x2	22.11	Shear	4
4x2	22.89	Shear	2
3x4	20.52	Shear	4
12x1	21.11	Shear	2

(a) debonding of CFRP (Specimen 1x4). (b) shear failure of Specimen 4x2.

Figure 4-9 Representative failure modes (Ramanathan et al. 2008)

5.0 EXPERIMENTAL RESULTS

This section presents the AE results from each test specimen. Specimens 1x4, 2x2 and 4x1 had the least increase in equivalent flexural reinforcement and were therefore dominated by flexural behavior as their ratio of shear capacity to retrofit flexural capacity remained below unity. Intermediate crack induced debonding (IC debonding) failures characterized the behavior of these slabs. In each of these retrofit slab specimens failure was relatively brittle and was characterized by complete CFRP debonding initiating beneath one of the point loads and progressing toward the nearest supports. A thin layer of concrete remained attached to the strips indicating that failure occurred in the concrete, adjacent to adhesive-to-concrete interface (see Figure 4-9a).

The increased flexural reinforcement in slab specimens 2x4, 4x2, 8x1, 3x4, 6x2 and 12x1 increased the flexural capacity of the slabs without affecting the shear capacity. In these cases, the shear capacity provided was insufficient to develop the full flexural capacity of the retrofitted slabs. As a result of the increased flexural capacity, shear failure characterized the ultimate behavior of these specimens. The failure was extremely brittle and occurred at the slab ends emanating from the supports as shown in Figure 4-9b. This behavior highlights the need to consider all limit states in a strengthening project rather than simply the limit states for which the strengthening is intended.

5.1 SLAB SPECIMEN 1X4

Counts, cumulative energy, amplitude and rise time of the acoustic activity are plotted as functions of time in Figure 5-1a-d, respectively. The values of total applied load (twice the shear carried by the slab) are superimposed on the plot of acoustic count history (Figure 5-1a).

During the first 50 seconds, up to an applied load of 1.3 kips (5.8 kN), the slab was settling onto its supports; emissions during this initial portion of the test are artifacts of the test set-up and disregarded. Significant acoustic activity was detected in two instances around 2.0 kips (8.9 kN) and 4.95 kips (22.2 kN), respectively. This activity was associated with the initiation of flexural cracks in the concrete matrix and is confirmed by the readings from the DWT (Figure 5-2a) and the strain gages (Figure 5-2b) (Ramanathan et al. 2008). The strain gage S2 shows an anomaly around 5 kips (23 kN) with respect to the strain gage recordings from CFRP strips (C1, C2, C3, C4) because S2 was attached to the steel reinforcement with in the concrete matrix and readily shows the initiation of flexural crack in the concrete matrix. Figures 5.1c and 5.1d show that high-amplitude AE events do not always correspond to high-rise time AE events. Such emissions are impulsive phenomena that originate short events of high energy. At 11.86 kips (53.4 kN) the density of AE events (number of AE events per unit of time or load) increased. Figure 5.1b reveals that much of the AE energy was detected by channel 2, which was located on the south side of the slab. At 13.3 kips (59.8 kN) the strip de-bonded from the concrete substrate. The intermediate crack induced debonding failure initiated along the southern part (see Figure 4.1) of the slab, and is confirmed by the higher AE activities observed in sensor 2, in comparison with those of sensor 1. At the instant of failure, AE events of amplitudes above 70 db and risetime above 400 microseconds were recorded. The residual load capacity observed following debonding is associated with the ability of the concrete slab to sustain the displacement rate.

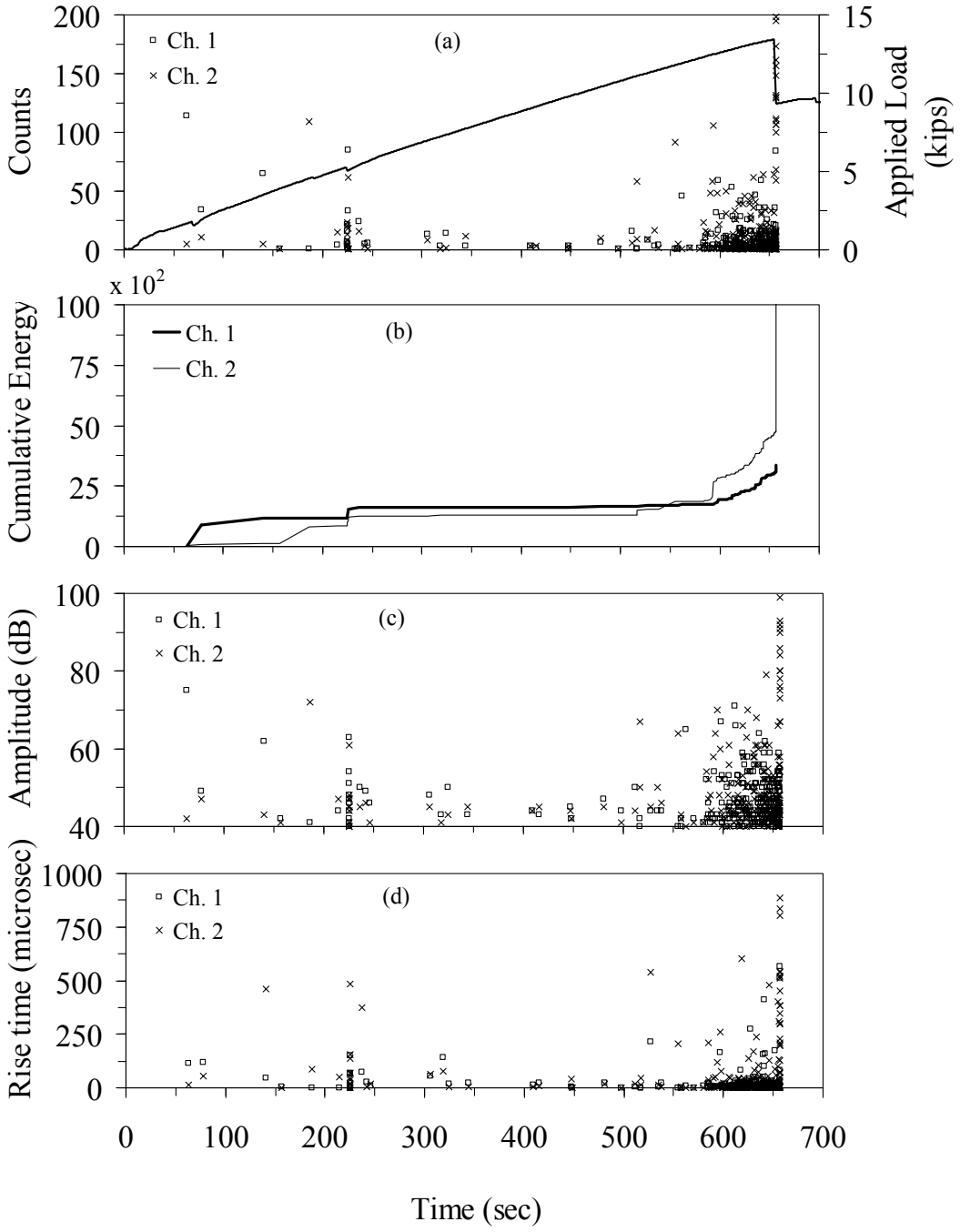

Figure 5-1 Acoustic emission results during quasi-static loading to failure for slab 1x4. Counts and applied load (a), cumulative energy (b), amplitude (c), and rise time (d) as a function of time.

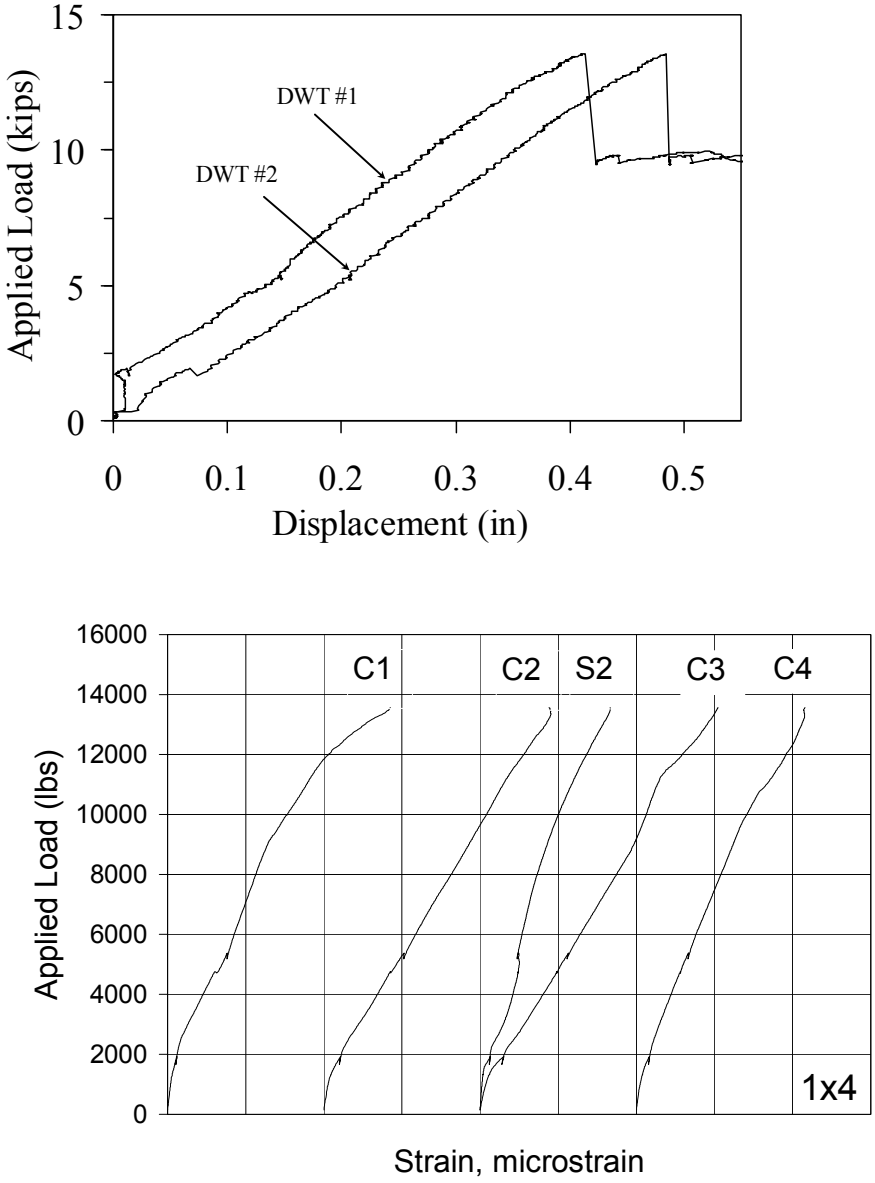

Figure 5-2 Load-displacement curves and strain data from different strain gages for the slab 1x4. (a) Load vs. displacement. (b) Plot of load vs. strain for the specimen 1x4. Vertical gridlines spaced at 1000 microstrain. Curves are horizontally offset 2000 microstrain for clarity (adapted from Ramanathan. 2008)

Figure 5-3 shows the locations of the AE sources determined using a linear algorithm. In order to identify the location of AE source, a set of preliminary pencil lead break tests were conducted to set the wave

velocity. The speed was set to 1 km/sec. The time occurrence of the event is plotted as a function of the X position (longitudinal) along the CFRP strip

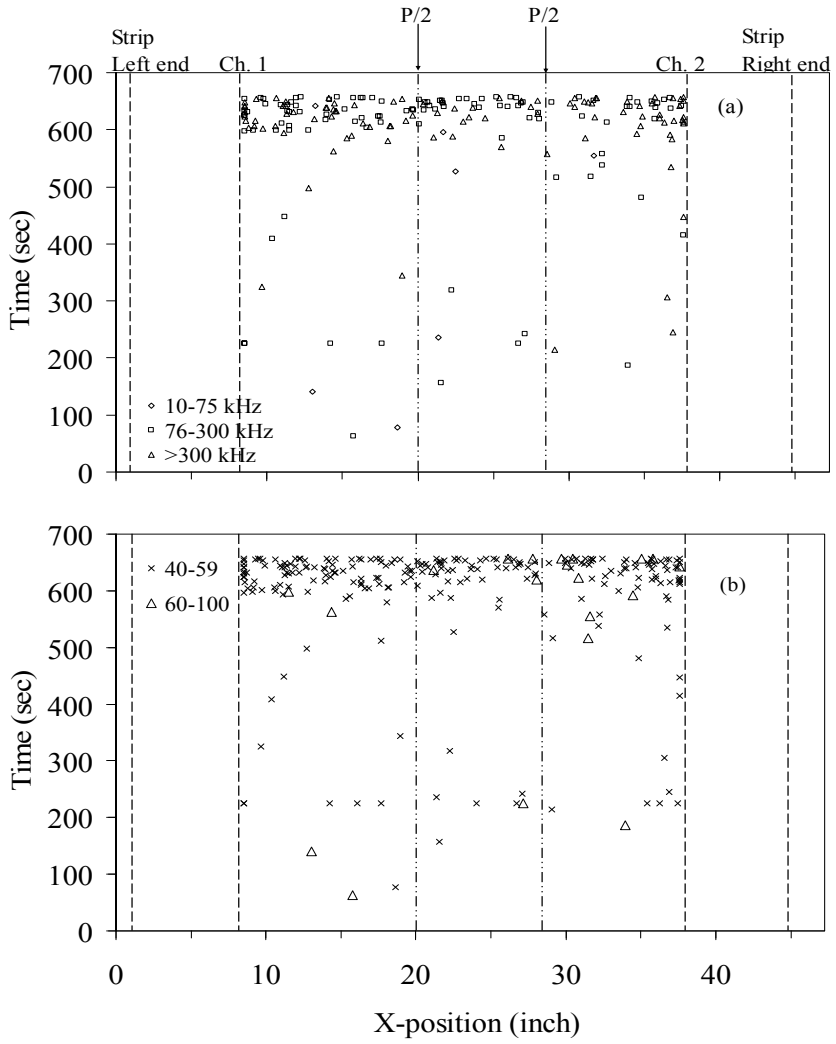

Figure 5-3 AE source location as a function of time for slab 1x4: (a) AE peak frequencies in the range 10-75 kHz, 76-300 kHz, >300 kHz are discriminated. (b) AE amplitudes in the range 40-59 dB and 60-100 dB are distinguished.

Figure 5-3a shows the location of the AE events as a function of time clustered by frequency content. It can be observed that higher frequency events are mainly localized in the shear span of the south side of

the slab. Event amplitudes between 40-59 dB and 60-100 dB are distinguished in Figure 5-3b. Higher amplitude events occurring prior to final failure were localized closer to channel 2. This validates that the de-bonding initiated toward the south end of slab.

Figure 5-4 shows the peak frequency and the centroidal frequency as a function of time. The plot of the applied load is superimposed. The peak frequency is concentrated mainly in two distinct clusters: between 100 and 200 kHz and between 400 and 500 kHz. The centroidal frequency is concentrated in a single cluster between 200 and 350 kHz. Lower values were observed especially during the first portion of the test, when cracks on the concrete surface were observed.

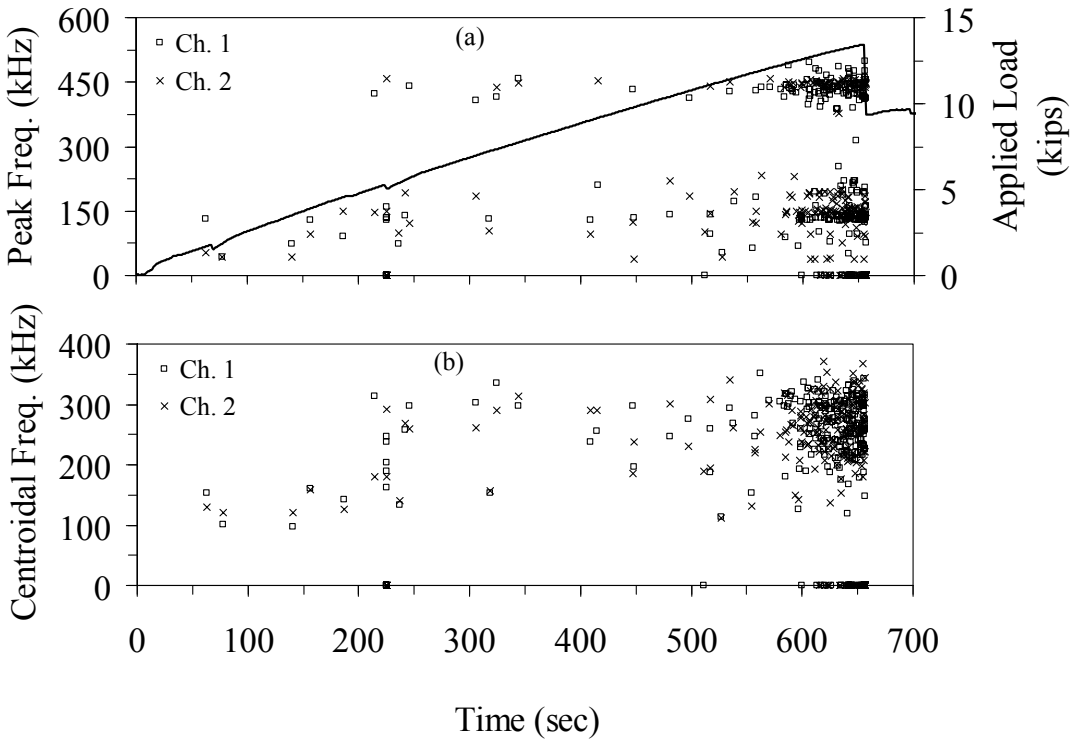

Figure 5-4 Spectral analysis of AE monitoring during quasi-static loading to failure for slab 1x4. (a) Peak frequency and applied load, (b) centroidal frequency as a function of time. The load history is superimposed.

When evaluating AE events by spectral analysis, which determines the frequency content of individual events, parameters such as the location of the AE source with respect to the transducer and the characteristics of the transducer itself must be considered (Mirmiran et al. 1999). Mirmiran et al. (1999) and Maji et al. (1994) showed that the frequency content of an AE signal in concrete beams is a function of the transducer's frequency response. The authors, in these cases, used narrowband transducers (R15, R15I) resonant at 150 kHz. The PICO transducers used in the present work possess a broad sensitivity in the range 250 – 750 kHz, which allows extension of the analysis up to 800 kHz. The peak frequency, rather than being uniformly distributed over the broad spectrum of the PICO, is concentrated in the two frequency ranges discussed above. This is most likely associated to the type of event that generated the AE and the characteristics of wave propagation in the multi-layer system composed of concrete substrate, adhesive, and CFRP strip (Rose 1999). Moreover, as the debonding failure progresses, the sensitivity of the sensing system to detect AE activity in concrete decreased and increased in terms of detection of AE sources from adhesive and CFRP strip. The reduced area of the bond decreased the area of acoustic coupling between concrete and CFRP.

Figure 5-5a shows the HI as a function of time. The plot of the CSS is superimposed. For clarity a magnified portion of Figure 5-5a is presented in Figure 5-5b. The presence of an AE knee, defined as a point of significant change in the slope of the CSS, is highlighted in the time history of the CSS. The AE knees may be used to identify possible damage mechanisms and to locate the onset of failure (Gostautas et al. 2005). Prior to debonding, in the time interval 580-650 seconds, a higher density of peaks was observed. The values of such peaks however are not necessarily the highest. This is because the value of a HI peak is associated with the variation in slope rather than to the slope itself. Figure 5-5c shows the severity, S_r, as a function of time with a plot of CSS superimposed. Both plots are qualitatively very similar to each other. Moreover the plot of the severity index is similar to the plot of the cumulative energy (Figure 5-1b). This signifies that the large amount of energy being released from high energy events generates a significant increase in the slope of the severity line. As for the plot of the cumulative energy, there is a significant increase in slope prior to the CFRP strip debonding. The increase is larger in

channel 2 which was closer to the area of debonding. Using the maximum value from each channel for both HI and severity, the intensity chart can be plotted (Figure 5-5d). Generally, this chart may be divided into intensity zones that identify the structural significance of a given sequence of AE events. Intensity values clustered toward the top right-hand corner are associated with phenomena of high structural significance, while less structurally significant events concentrate near the bottom left (Gostautas et al. 2005). In Figure 5-5d the fact that the value from sensor 2 is in the upper right corner compared to the value from sensor 1 confirms that the greater amount of damage occurred in the area of sensor 2.

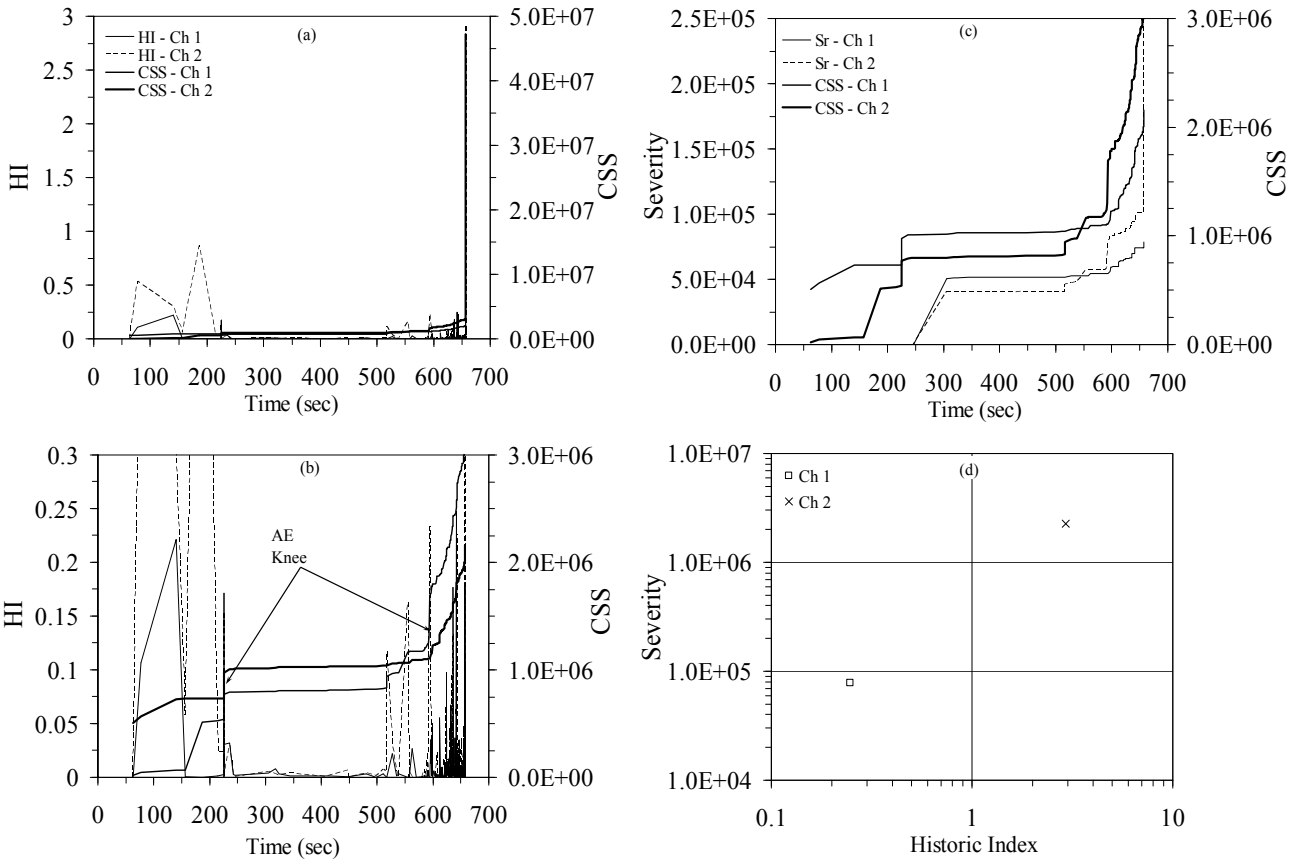

Figure 5-5 Intensity analysis for slab 1x4. (a) Historic index as a function of time. The plot of the cumulative signal strength is superimposed. (b) Magnified portion of plot (a). (c) Severity index as a function of time. The plot of the cumulative signal strength is superimposed. (d) Intensity chart.

Figure 5-6 shows the PCA visualization of the AE data for slabs 1x4. The analyses reduced the dimension from three AE parameters (Amplitude, counts, and risetime) (Figure 5-6a) and from five AE parameters (Amplitude, energy, counts, duration, and risetime) (Figure 5-6b) to two principal components. For AE events associated with damage onset or propagation, no relevant data can be identified. However all low signature AE events are clustered at the origin (0, 0). The results show that data move away from the origin toward the negative values of the first principal component. All data from the instant prior to failure are located away from the main cluster at the origin. The fact that such data are associated with channel-two transducer confirms that the CFRP disbond was localized in the area close to senor 2. Moreover, the scattering behavior of the data clusters varies with the selection of the AE parameters used in the input vector. As such, further study of AE parameter selection for PCA analysis can be employed to maximize the outputs in terms of clustering.

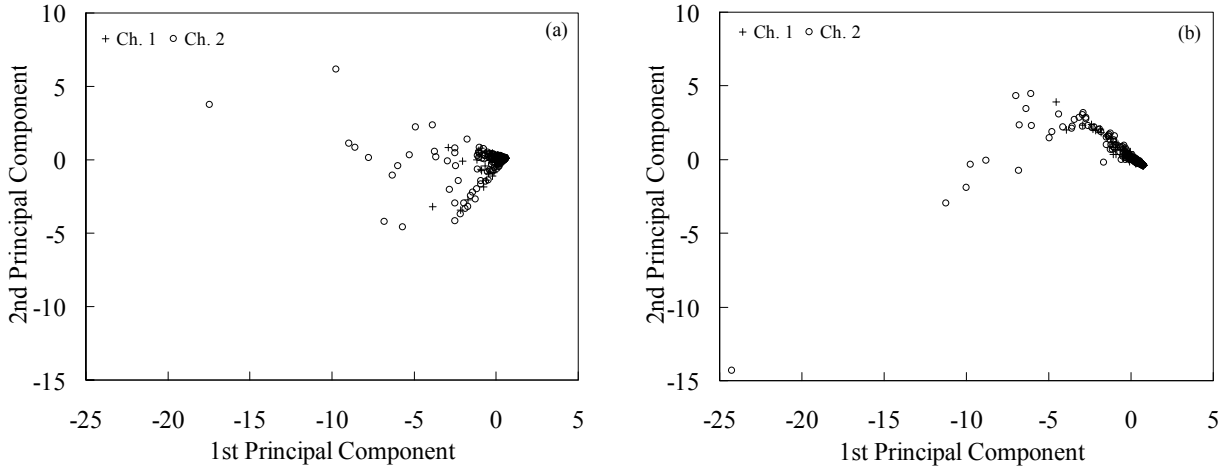

Figure 5-6 PCA reduction of standardized traditional AE features from AE monitoring of slab 1x4 (a-b) (a) AE amplitude, counts, and risetime in the input vector. (b) Amplitude, energy, counts, duration, and risetime in the input data vector.

5.2 SLAB SPECIMEN 2X4

Counts, cumulative energy, amplitude and rise time of the acoustic activity are plotted as a function of time in Figure 5-7a-d, respectively. The values of total applied load are also superimposed. The load profile shows a discontinuity around 70 seconds. This discontinuity was probably related to the formation of flexural cracks. Cracks initiated at the level of rebar were also observed. However the nature of the crack and its distance from the AE transducers suggest that no significant acoustic activity were expected to be detected. The variation of the applied load-time plot observed around 180 seconds was associated with a manual variation of the loading rate. This more heavily reinforced slab (twice the CFRP of previously described 1x4) failed at 16.8 kips (75.6 kN) due to a concrete shear failure occurring at the north support, i.e.: close to sensor 1 but not between sensors 1 and 2. Despite the preliminary pencil lead break tests having determined that the sensitivity of the attached AE transducers was similar to the sensitivity observed for specimen 1x4, the signals obtained from this slab were weaker. This is associated to the fact that many AE events were related to the onset and propagation of cracks in concrete. Except for two isolated events, all AE amplitudes were below 60 dB (Figure 5-7c). The outcomes from the location source (Figure 5-8) did not highlight the accurate occurrence of shear failure above the north support (Channel 1). The approximate estimation of the source location of shear failure may be attributed to the choice of wave speed of 1 km/sec in the location algorithm which is different from the wave speed in concrete. This is most likely associated with the choice of the wave speed in the location algorithm.

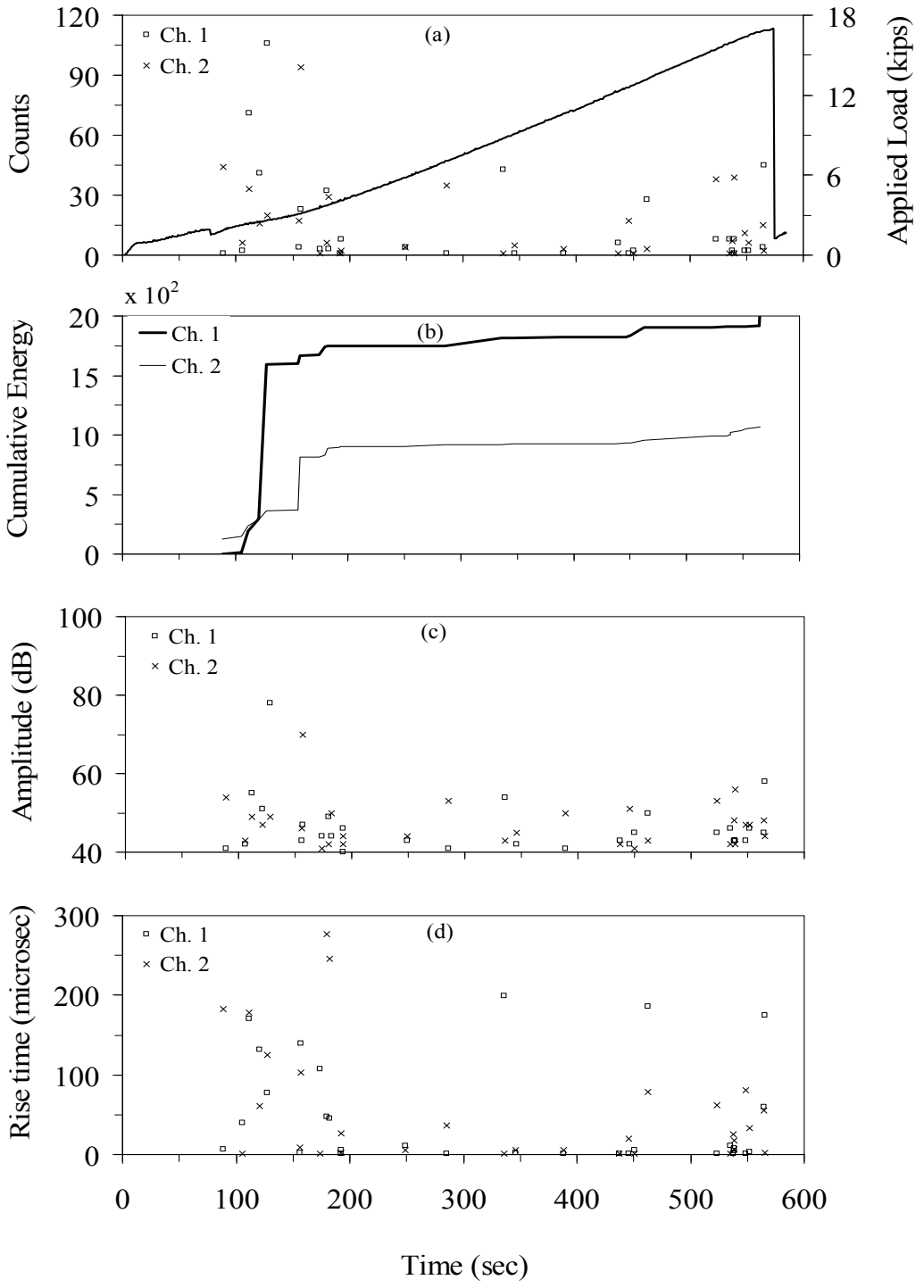

Figure 5-7 Acoustic emission results during quasi-static loading to failure for slab 2x4. Counts and applied load (a), cumulative energy (b), amplitude (c), and rise time (d) as a function of time.

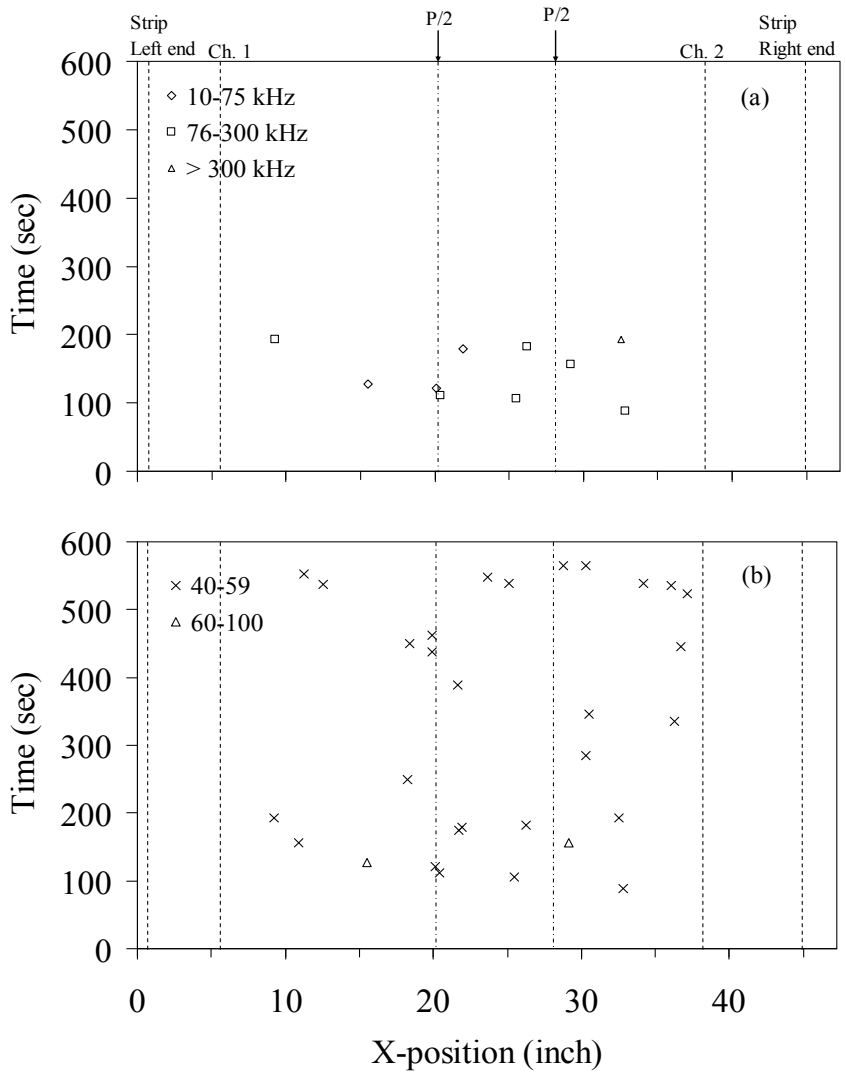

Figure 5-8 AE source location as a function of time for slab 2x4: (a) AE peak frequencies in the range 10-75 kHz, 76-300 kHz, >300 kHz are discriminated. (b) AE amplitudes in the range 40-59 dB and 60-100 dB are distinguished.

More interesting data are collected from the spectral analysis (Figure 5-9). The peak frequency (Figure 5-9a) and centroidal frequency (Figure 5-9b), both plotted as a function of time, show clusters below 100 kHz and between 100 and 150 kHz, respectively. Such lower values in comparison with the frequencies observed in Figure 5.4 are expected due to (a) the dominance of concrete behavior in this specimen and (b) the high attenuation of higher frequencies in concrete. The frequencies obtained towards the end of the experiment are below 10 kHz. These frequencies below 10 kHz are filtered and are not seen in the spectral analysis (Figure 5-9).

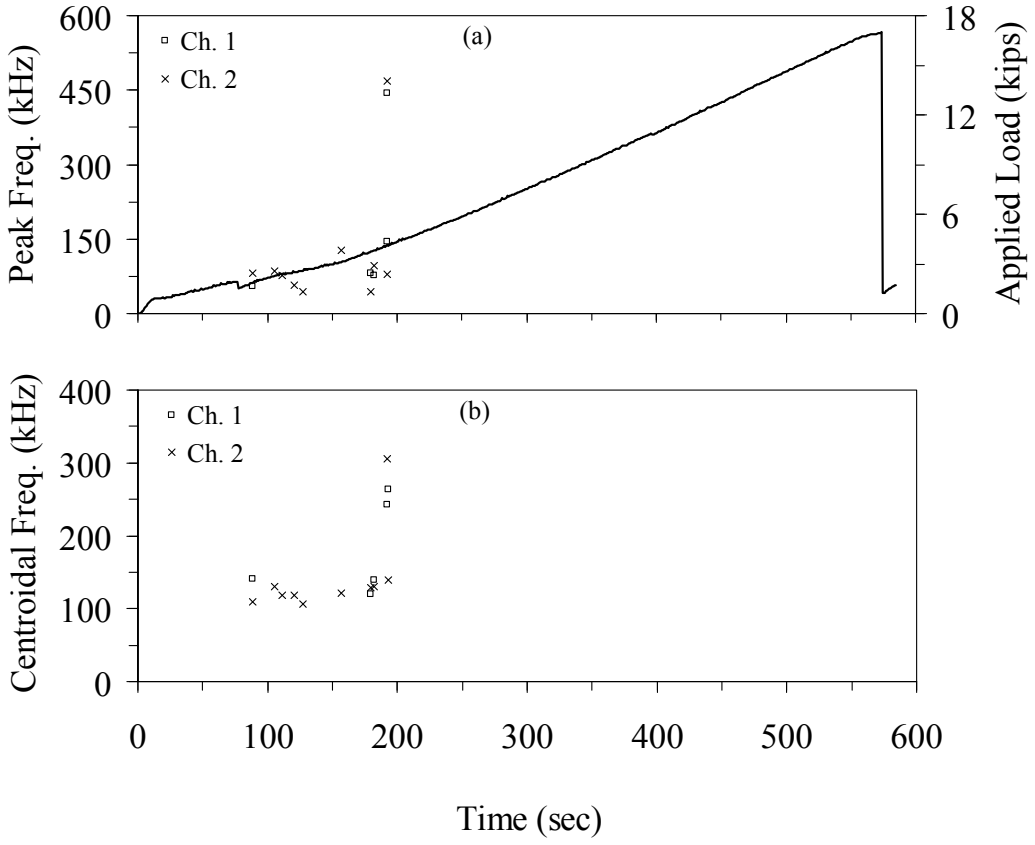

Figure 5-9 Spectral analysis of AE monitoring during quasi-static loading to failure for slab 2x4. (a) Peak frequency and applied load, (b) centroidal frequency as a function of time. The load history is superimposed.

Figure 5-10a shows HI as a function of time. The plot of the CSS is superimposed. The presence of an AE knee was not observed as there is no debonding (or any other major damage) occurred until the final shear failure of slab. Around 150 seconds, a change in slope with peak values of HI are observed. Such peaks however are not associated with CFRP debonding. Figure 5-10b shows the severity, S_r, as a function of time with a plot of CSS superimposed. This plot signifies the severity of damage at the time frame of 450-600 seconds, i.e., before the final failure. The increase in severity is larger in channel 1 which was closer to the area of shear failure. Using the maximum value from each channel for both HI and severity, the intensity chart can be plotted (Figure 5-10c). The fact that the value from sensor 1 is in the upper right

corner compared to the value from sensor 2 confirms that the greater amount of damage occurred in the area closer to sensor 1.

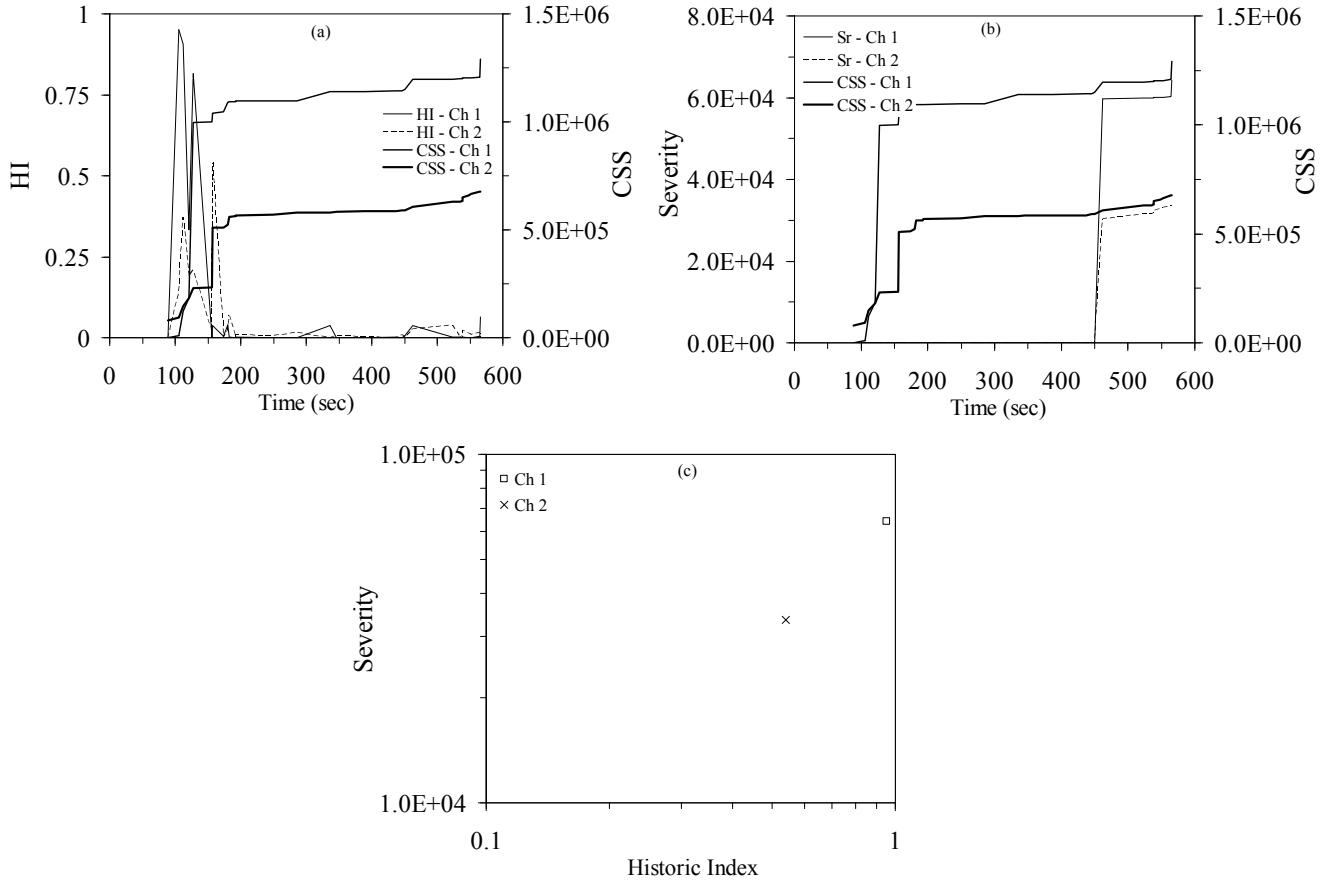

Figure 5-10 Intensity analysis for slab 2x4. (a) Historic index as a function of time. The plot of the cumulative signal strength is superimposed (b) Severity index as a function of time. The plot of the cumulative signal strength is superimposed. (c) Intensity chart.

Figure 5-11 shows the PCA visualization of the AE data. The analyses reduced the dimension from three AE parameters (Figure 5-11a) and from five AE parameters (Figure 5-11b) to two principal components. For AE events associated with damage onset or propagation, no relevant data can be identified. All low signature AE events are clustered at the origin (0, 0). The results from slab 2x4 (Figure 5-11a and Figure

5-11b) show that data move away from the origin toward the positive values of the first principal component. All data from the instant prior to failure are located away from the main cluster at the origin.

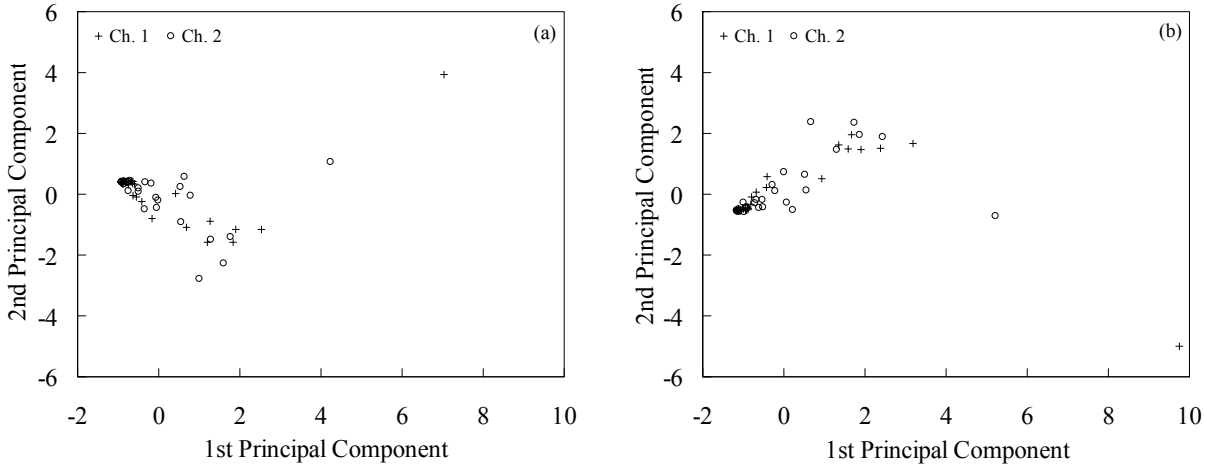

Figure 5-11 PCA reduction of standardized traditional AE features from AE monitoring of slab 2x4 (a-b) (a) AE amplitude, counts, and risetime in the input vector. (b) Amplitude, energy, counts, duration, and risetime in the input data vector.

5.3 SLAB SPECIMEN 4X1

The area of the CFRP in this slab was equal to the area of CFRP in slab specimen 1x4. Two PICO transducers were glued onto the second strip from west (see Figure 4-4). Counts and total applied load, cumulative energy, amplitude and rise time of the acoustic activity are plotted as a function of time in Figure 5-12a-d respectively. The step-like shape of the load history at failure is due to the progression of individual strip debonding from the slab. The load profile shows a small discontinuity around 8.9 kips (40 kN), which is due to flexural cracks in the slab. The third strip from west debonded at 16.5 kips (74.25 kN), followed by second, first, and fourth strips. All strips exhibited intermediate crack induced

debonding and debonded toward the south side of the slab in the area close to channel 1 transducer; the north end of the strips remained bonded to the concrete.

The result from the PA (Figure 5-12) shows that sensor 1 detected higher activity than sensor 2. Because the third CFRP strip failed first (at 550 seconds) and second strip failed 30 seconds later, the AE system was able to record the emissions from both debonding events. Due to the proximity to the channel 1 transducer of the area of third strip that debonded, the AE parameters (counts, energy, and rise time) associated with both failures have similar values. The other two strips failed shortly afterward, at 590 seconds, and 598 seconds, respectively. It is not surprising that the AE transducers were able to also detect the AE originating in first and fourth strips. The fact that only a portion of second strip is bonded from the concrete substrate allows the continued acoustic transmission from concrete into the laminate. As the acoustic energy enters the laminate, the stress wave undergoes less attenuation as it travels along the debonded strip since no leakage into surrounding material is possible. As such, AE parameters recorded during the failure of both first and fourth strips have comparable or even higher values. No relevant information with respect to debonding was revealed by studying the location history plot (Figure 5-13). Therefore, the location history plots are not provided for the subsequent slab specimens. The analysis in the frequency domain (Figure 5-14) provides results very similar to those discussed in Figure 5.4 for the case of the slab specimen 1x4.

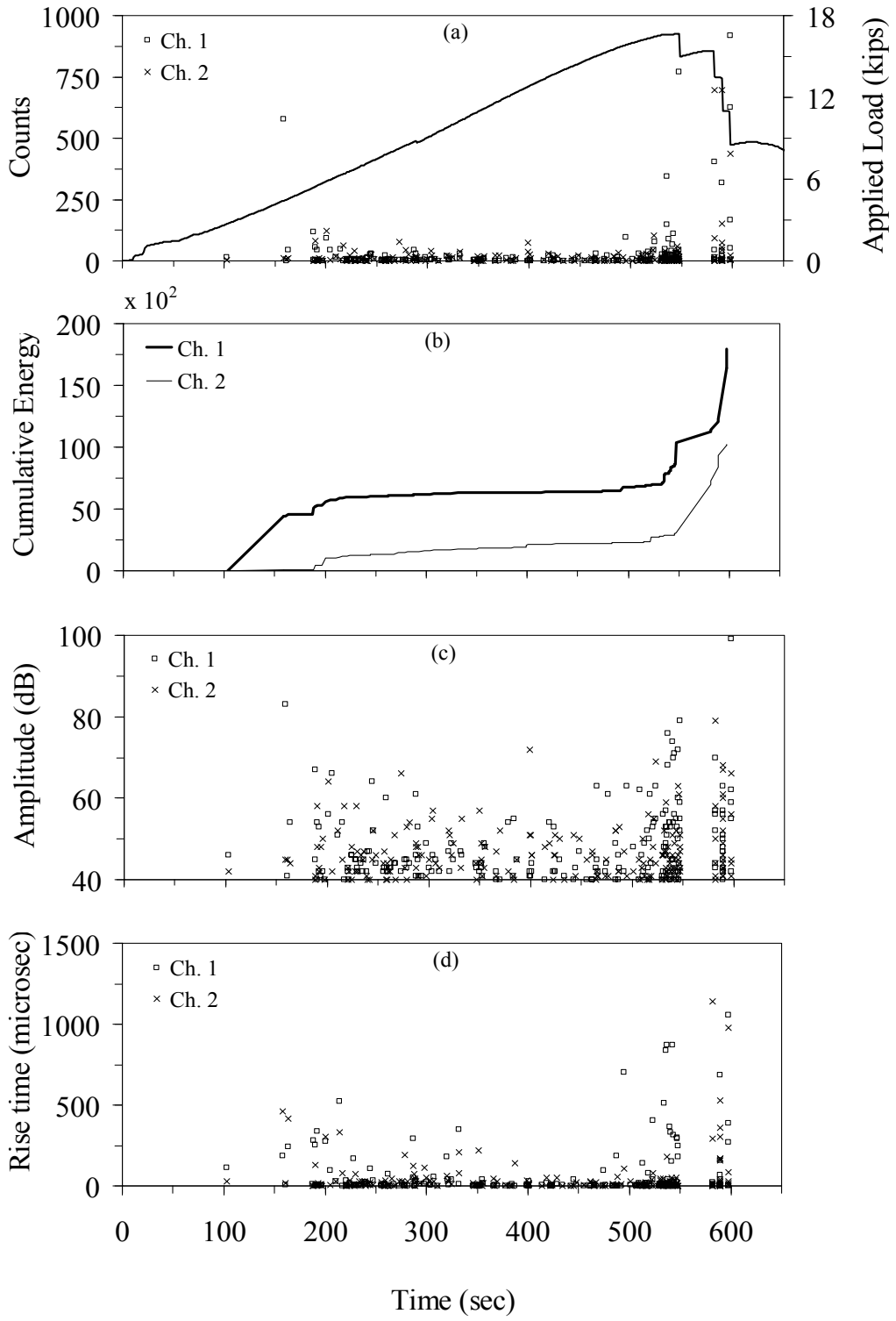

Figure 5-12 Acoustic emission results during quasi-static loading to failure for slab 4x1. Counts and applied load (a), cumulative energy (b), amplitude (c), and rise time (d) as a function of time.

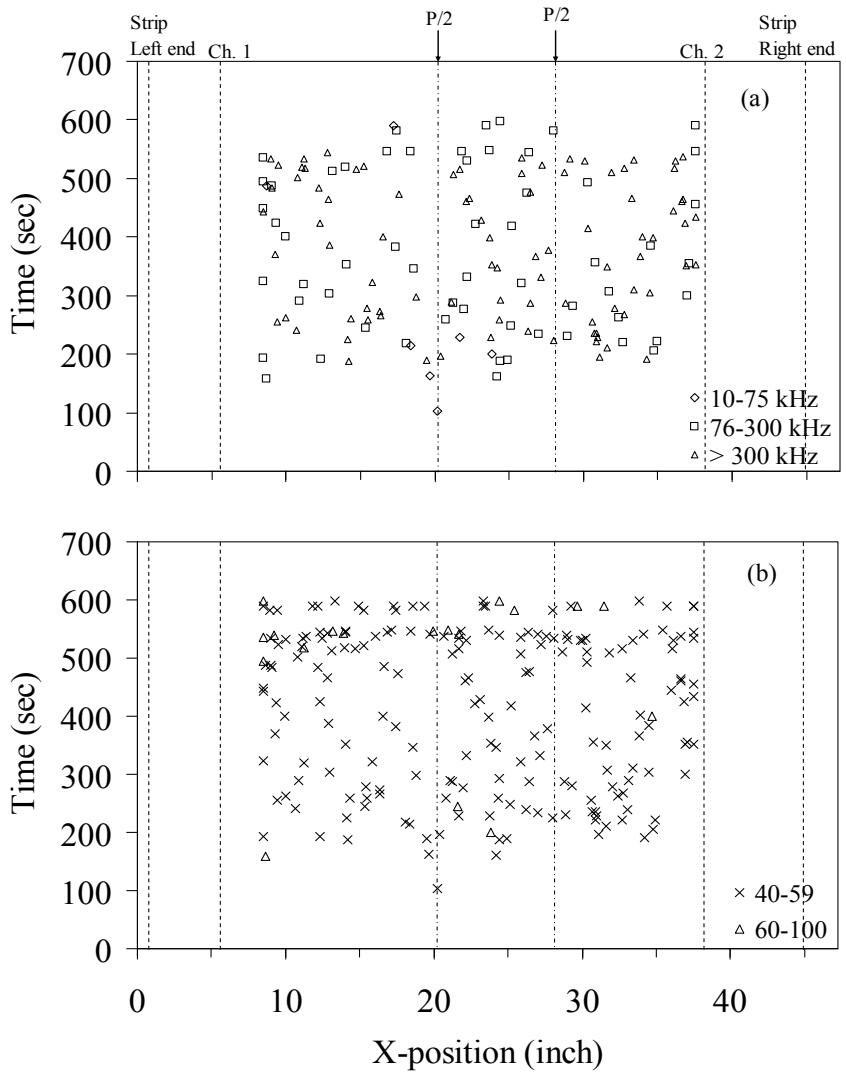

Figure 5-13 AE source location as a function of time for slab 4x1: (a) AE peak frequencies in the range 10-75 kHz, 76-300 kHz, >300 kHz are discriminated. (b) AE amplitudes in the range 40-59 dB and 60-100 dB are distinguished.

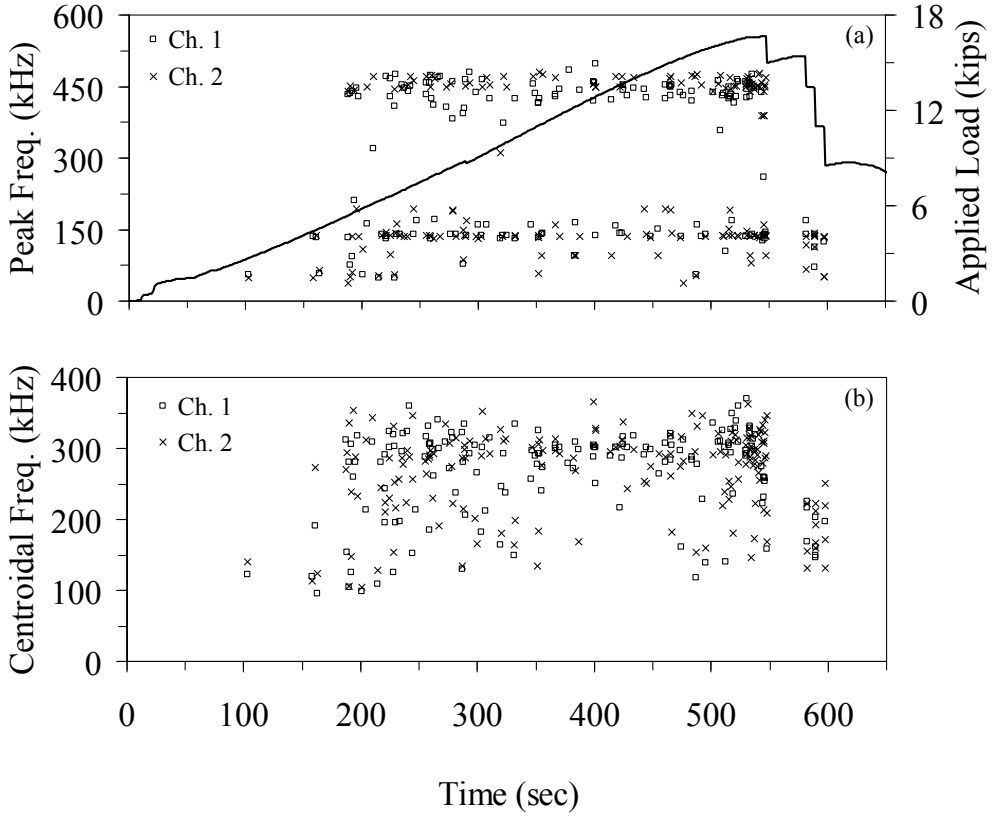

Figure 5-14 Spectral analysis of AE monitoring during quasi-static loading to failure for slab 4x1. (a) Peak frequency and applied load, (b) centroidal frequency as a function of time. The load history is superimposed.

From the IA, although the AE knee was clearly highlighted at the initiation of debonding, the sequence of debonding of individual CFRP strips is not established from HI. Similar observations are made from the severity index. Moreover, the intensity chart for this slab did not correlate well with the regular trend (Gostautas et al. 2005) followed by a typical intensity chart. The value from sensor 1 is in the upper left corner compared to the value from sensor 2, which is located towards bottom right.

The Intensity charts for slab specimens mentioned in this section and subsequent sections are illustrated in Chapter-6.

For AE events associated with damage onset or propagation, no relevant data can be identified through the PCA. Moreover, the results are not satisfactory in this case with the scattering data moving

away from origin towards the positive values of the first principal component. All data from the instant prior to failure are located away from the main cluster at the origin.

The PCA plots for slab specimens mentioned in this section and subsequent sections are presented in Chapter-6. The plots for slab specimens that differentiate between debonding and shear failure are also shown in Chapter-6.

5.4 SLAB SPECIMEN 8X1

Four PICO transducers were placed on the 3rd strip and 6th strips from the west side of the slab (see Figure 4-4). Counts and total applied load, cumulative energy, amplitude and rise time of the acoustic activity are plotted as a function of time in Figure 5-15a-d respectively. Before 80 seconds the load profile seems to be non-linear indicating some settlement of the slab in the test frame. At 86 seconds and 260 seconds, the load profile shows two small discontinuities associated with flexural cracks in the tensile zone of the slab. While the first event created enough energy to be detected by sensor 2 (count number above 100), the energy released during the second event was detected by the sensor 3. The second event is validated by a crack observed on west face of slab closer to the north support i.e., close to channel 3 transducer. A significant change in the slope of the cumulative energy from channel 3 (Figure 5-15b) is observed at 525 seconds and 580 seconds, which can be associated to the AE activity released from the CFRP fiber damage. AE amplitude also provided similar indications at this stage (Figure 5-15c). This observation is validated from the load history (Figure 5-15a) as the there is no visible load drop which can be associated with any activity in concrete such as cracks. Shear failure of the slab occurred at 21.75 kips (97.85 KN) at the south support in the area closer to the channel 1 transducer. This was confirmed by the parameter analysis which shows a significant event at the instance of the failure with number of counts close to 2,000 and signal amplitudes up to 78 dB. The rise time also provided similar indications. The Intensity chart and PCA plot are presented in Chapter-6.

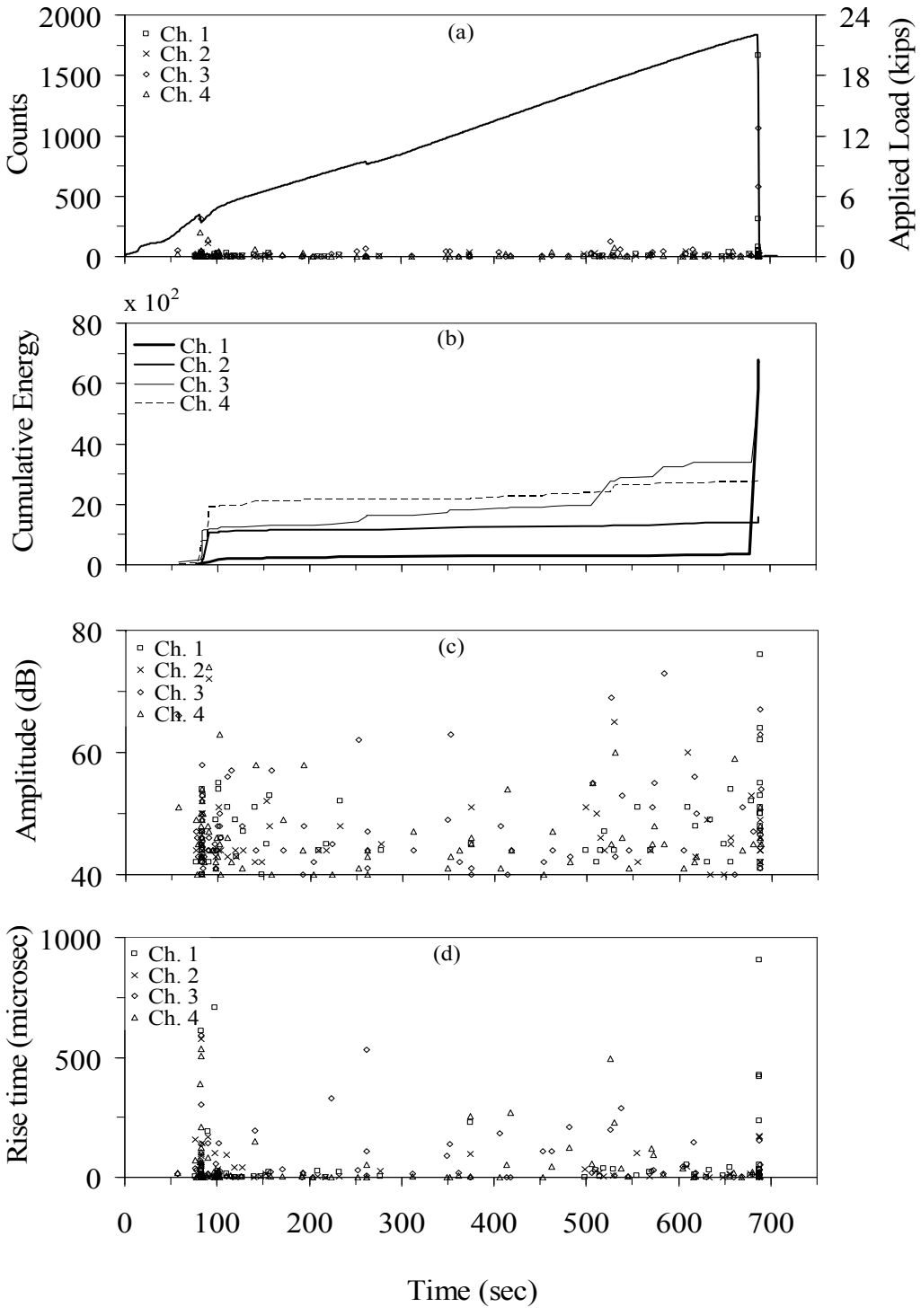

Figure 5-15 Acoustic emission results during quasi-static loading to failure for slab 8x1. Counts and applied load (a), cumulative energy (b), amplitude (c), and rise time (d) as a function of time.

5.5 SLAB SPECIMEN 2X2

In slab 2X2 the total area of CFRP was also equal to the area of CFRP in slab 1X4. Counts and total applied load, cumulative energy, amplitude and rise time of the acoustic activity are plotted as functions of time in Figure 5-16a-d, respectively. The step-like response of the load profile and AE activity recorded at the beginning of the test were associated with an unintended initial rapid increase in applied load. At a load of approximately 6 kips an audible sound was detected. A visual inspection identified the presence of a splitting crack on the west side of the slab along the 3rd rebar from north. At the same instant some AE activity was recorded, anticipated by an event at 5.55 kips (25 kN). Between 6 kips (27 kN) and 12 kips (54 kN) no activity above 60 dB was recorded, and the slope of the cumulative energy curve was constant. Although there seems no load drop or any discontinuity from load history, the AE parameters i.e. cumulative energy and amplitude recorded some activity, around 12 kips (54 kN). This event can be associated with some damage occurred in CFRP strip prior to debonding. The slab failed at 14.8 kips (66.6 kN) due to intermediate crack induced debonding.

The debonding initially occurred along the strip instrumented with the AE transducers toward the south end of the slab in the area closer to the channel 2 transducer. The failure of the second strip, fifteen seconds later, could not be monitored because the AE transducers were attached to the strip that debonded first. The parameter analysis shows that both transducers recorded the same type of activity. As such it is proved that the most severe events were equally spread over the bond between the CFRP strip and the concrete subsurface. The Intensity chart and PCA plot are presented in Chapter-6.

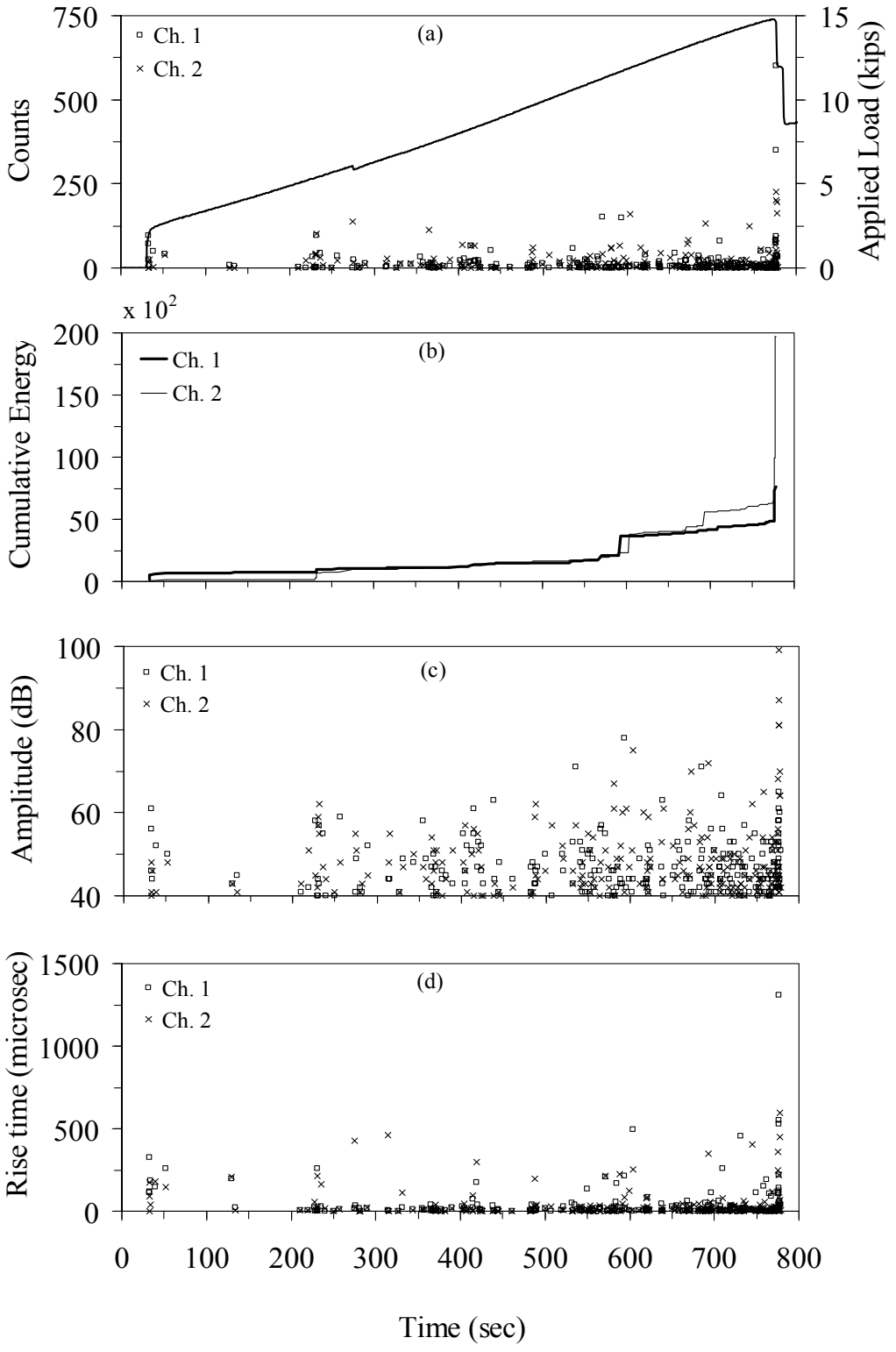

Figure 5-16 Acoustic emission results during quasi-static loading to failure for slab 2x2. Counts and applied load (a), cumulative energy (b), amplitude (c), and rise time (d) as a function of time.

5.6 SLAB SPECIMEN 6X2

Counts, cumulative energy, amplitude and rise time of the acoustic activity are plotted as a function of time in Figure 5-17a-d, respectively. The nonlinear behavior of the loading profile in the initial 100 seconds was associated with settlement of the slab on the supports. All plots show an overall constant activity rate (number of events per unit of load or unit of time); in such sense the slope of the cumulative energy plot (Figure 5-17b) is constant until 90% of the failure load. The significant energy release associated with the catastrophic shear failure is clearly evident in Figure 5-17b. The concentrated AE amplitudes of 60 dB in Figure 5-17c was associated with flexural cracks occurred in the concrete. The slab failed at 22.11 kips (99.5 kN) due to shear failure closer to the north support, i.e. close to sensors in channels 1 and 3.The parameter analysis shows that the AE events recorded are higher for channels 1 and 3 around 825 seconds. This validates the experimental evidence that the shear failure occurred along the north side of the slab. The Intensity chart is not presented for this specimen as the data acquired is not sufficient enough to plot HI and severity. The PCA plot is presented in Chapter-6.

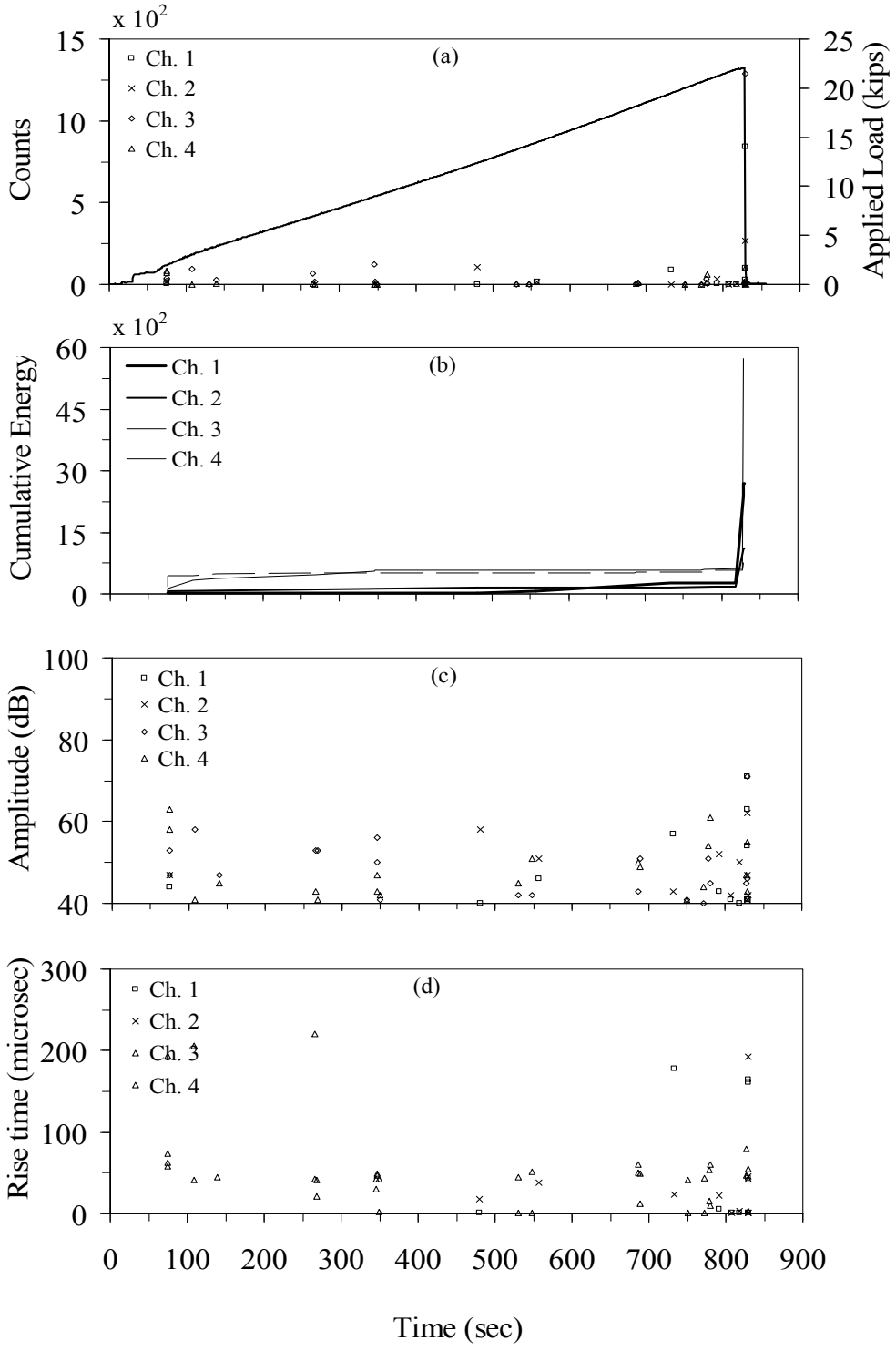

Figure 5-17 Acoustic emission results during quasi-static loading to failure for slab 6x2. Counts and applied load (a), cumulative energy (b), amplitude (c), and rise time (d) as a function of time.

5.7 SLAB SPECIMEN 4X2

Counts, cumulative energy, amplitude and rise time of the acoustic activity are plotted as a function of time in Figure 5-18a-d, respectively. In this test, the load rate was reduced at 140 seconds as the slab was being strained faster than predicted. All the plots in Figure 5-18 show an overall constant activity rate (number of events per unit of load or unit of time); in such sense the slope of the cumulative energy plot (Figure 5-18b) was constant until 80% of the failure load. The concentrated AE amplitudes of 60 dB in Figure 5-18c can be associated with flexural cracks occurred in the concrete (sub-surface cracks). The slab failed at 22.89 kips (103 kN) due to shear failure closer to the south support, i.e. close to sensor in channel 2. The parameter analysis shows that the AE events recorded are higher for channel 2 at the time of maximum load. This validates the experimental evidence that the shear failure occurred along the south side of the slab. The Intensity chart is presented in Chapter-6. As the results from the PCA did not provide meaningful results, the plots associated with this analysis are not presented.

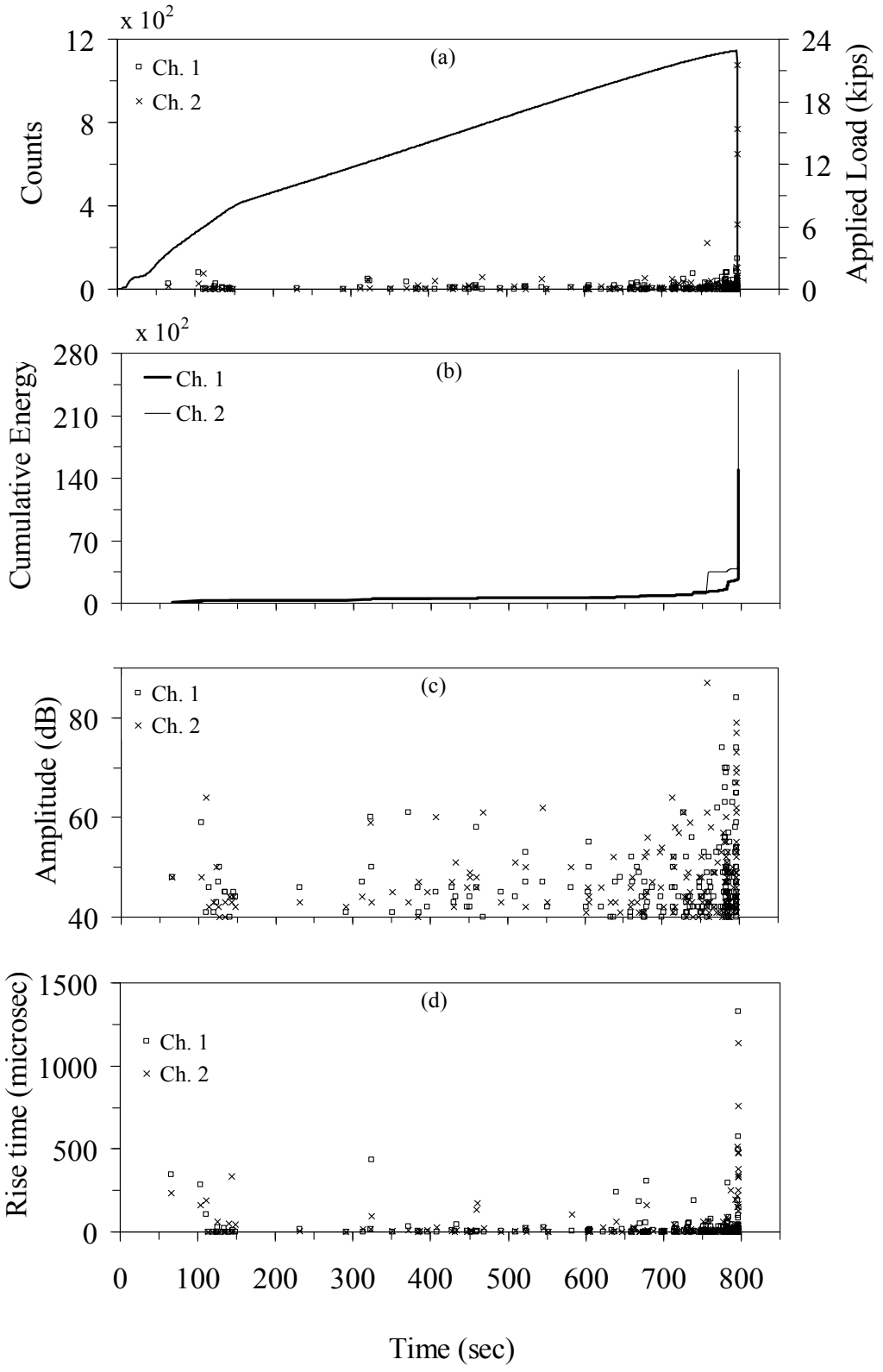

Figure 5-18 Acoustic emission results during quasi-static loading to failure for slab 4x2. Counts and applied load (a), cumulative energy (b), amplitude (c), and rise time (d) as a function of time.

5.8 SLAB SPECIMEN 3X4

Counts, cumulative energy, amplitude and rise time of the acoustic activity are plotted as a function of time in Figure 5-19a-d, respectively. In this test, the load rate was increased at 410 seconds as the slab was being strained slower than predicted. A visible crack occurred on the face of the concrete slab in the direction of south at 425 seconds. This activity can be seen from the load profile with a dip at 425 seconds. Then, the load rate was reduced at 710 seconds as the slab was being strained faster. Significant increase in AE amplitude (75 dB) and cumulative energy can be observed within the 550-800 seconds time frame due to increased rate of loading. The slab failed at 20.52 kips (92.34 kN) due to shear failure closer to the south support, i.e. close to sensors in channels 2 and 4. The location plot did not provide any relevant information and it is not shown here. The parameter analysis shows that the AE events recorded are higher for channel 2 at the time of maximum load. This validates the experimental evidence that the shear failure occurred along the south side of the slab. The Intensity chart is presented in Chapter-6.

As the results from the PCA did not provide meaningful results, the plots associated with this analysis are not presented.

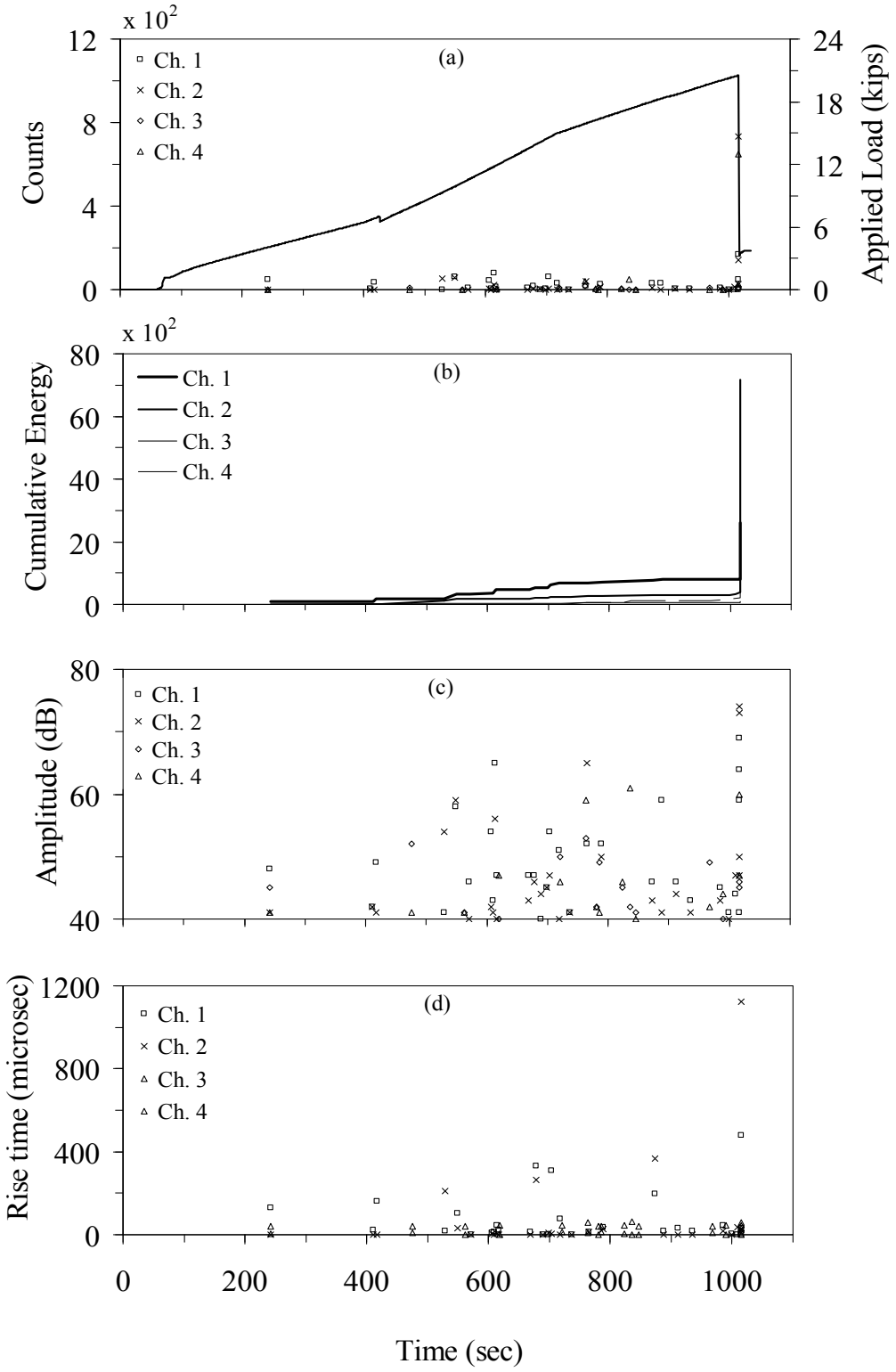

Figure 5-19 Acoustic emission results during quasi-static loading to failure for slab 3x4. Counts and applied load (a), cumulative energy (b), amplitude (c), and rise time (d) as a function of time.

5.9 SLAB SPECIMEN 12X1

Counts, cumulative energy, amplitude and rise time of the acoustic activity are plotted as a function of time in Figure 5-20a-d, respectively. The AE activity recorded at 150 seconds are due to settlement of slab on the supports. The AE counts plot (Figure 5-20a) shows that at 810 seconds there was a significant activity towards channel 2 which can be associated with crack in concrete near the same channel. The slab failed at 21.11 kips (95 kN) due to shear failure closer to the south support, i.e. closer to sensor in channel 2. The location plot did not provide any relevant information and it is not shown here. The cumulative energy plot shows that the AE events recorded are higher for channel 2 at the time of maximum load. This validates the experimental evidence that the shear failure occurred along the south side of the slab. The Intensity chart is presented in Chapter-6.

As the results from the PCA did not provide meaningful results, the plots associated with this analysis are not presented.

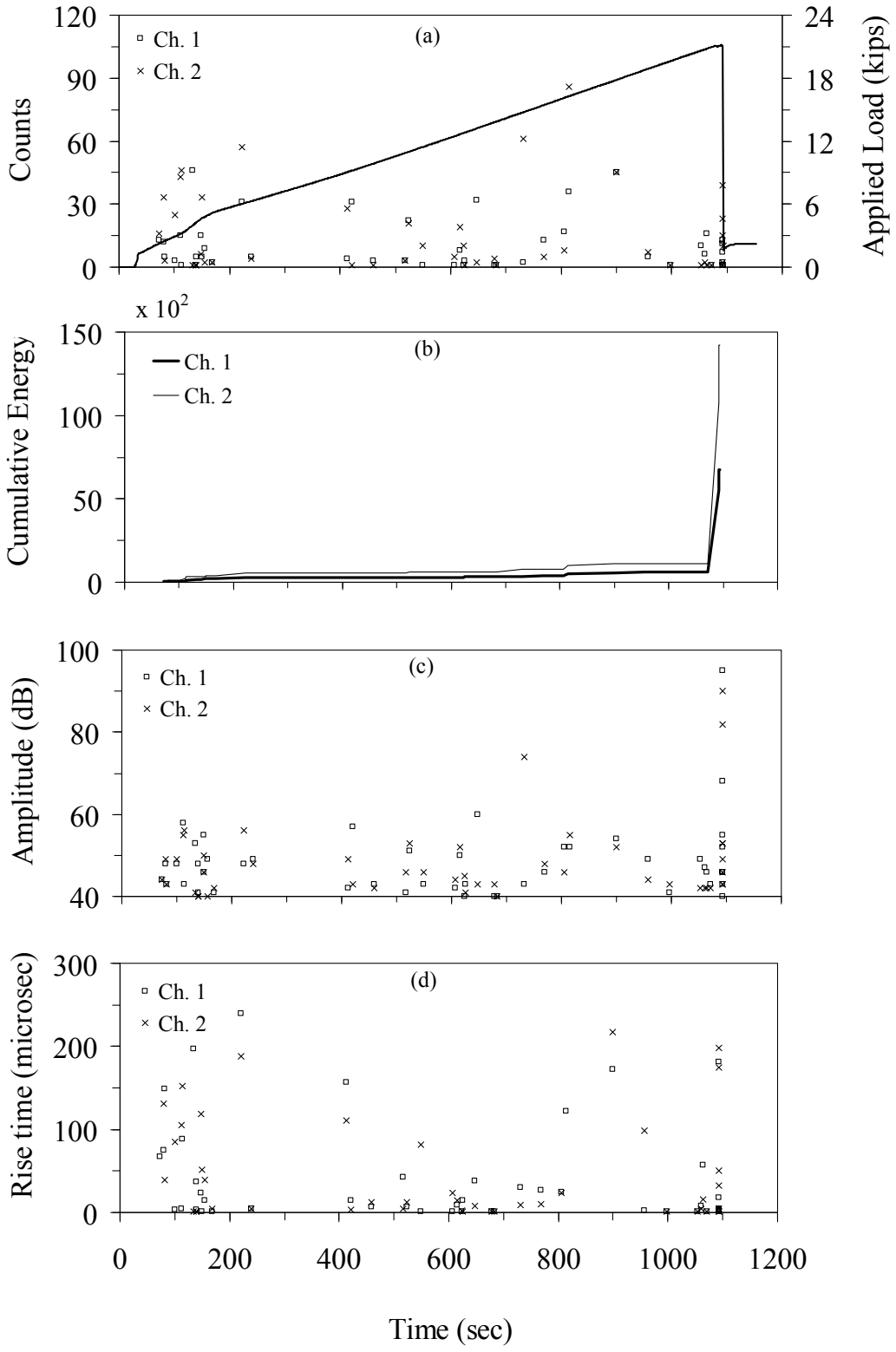

Figure 5-20 Acoustic emission results during quasi-static loading to failure for slab 12x1. Counts and applied load (a), cumulative energy (b), amplitude (c), and rise time (d) as a function of time.

6.0 DISCUSSION

Nine slabs retrofitted with different ratios of CFRP width-to-CFRP spacing were tested to assess the effects of CFRP geometry and placement on the structural response of such retrofitted systems (Ramanathan et al. 2008). Simultaneously the feasibility of AE to monitor the onset, growth and propagation of defects in such structural systems was carried out. Three different approaches to analyze AE data, namely, PA, IA, and PCA were used with the aim of identifying the different modes of structural failure and to provide a means to predict the onset of failure. Monitoring of the acoustic activities in the slabs subjected to monotonic load-to-failure allowed to follow the occurrence and progression of early damage that was not necessarily detectable by as macroscopic stiffness changes or visually observable phenomena. Amplitude, energy, and frequency components of the acoustic emissions were used to provide a qualitative correlation with the type of damage observed. The parametric analysis demonstrated that flexural cracks near the laminates and debonding produce AE activities much higher in terms of signal amplitude and frequency range than eventual shear cracking. Although initially counterintuitive (shear cracks release greater energy than flexural cracks), this observation is explained by the crack locations. Flexural cracks are expressed at the CFRP-concrete interface and thus their emissions are transmitted directly by the CFRP strip on which the AE sensors are mounted. Shear cracks, on the other hand, occur in the body of the concrete and do not affect the CFRP-concrete interface significantly.

In parameter analysis AE counts, cumulative energy, amplitude, and risetime typically differentiated the damage behavior due to initiation of CFRP debonding, complete debonding, and shear failure in the concrete matrix. Events of high amplitudes and low amplitudes tend to signify debonding and matrix cracking respectively. Although, not presented for all the slab specimens, location history

signified the points of AE source with respect to time. The choice of PICO transducers, for AE monitoring proved to be satisfactory as they possess a wide range of sensitivity about 250-750 kHz. The spectral analysis plots helped in discriminating the frequencies observed for different types of damage characteristics, such as matrix cracking and debonding.

A comparative study of failure occurrences of the slabs conducted with the IA demonstrated that such an approach can be used to provide warning of severe structural events in real-time. This analysis approach showed that cumulative signal strength correlates well with the degree of damage sustained by the slabs. Figure 6-1a and 6.1b show the intensity charts for the specimens that failed due to CFRP debonding and due to shear failure, respectively. In order to divide the intensity chart into intensity zones that can be used for providing a precursor to the onset of permanent damage, a larger number of samples needs to be tested. Although no generalization can be made at this stage, a trend is readily observed. The values associated with CFRP strip debonding are localized in right side of the chart whereas the values associated with shear failure are localized in the lower left side of the chart. The observation that CFRP debonding is in upper right and shear in the lower left of the IA plots can be easily explained as the CFRP serves as a waveguide. Thus one would expect this behavior as the CFRP hits are more significant.

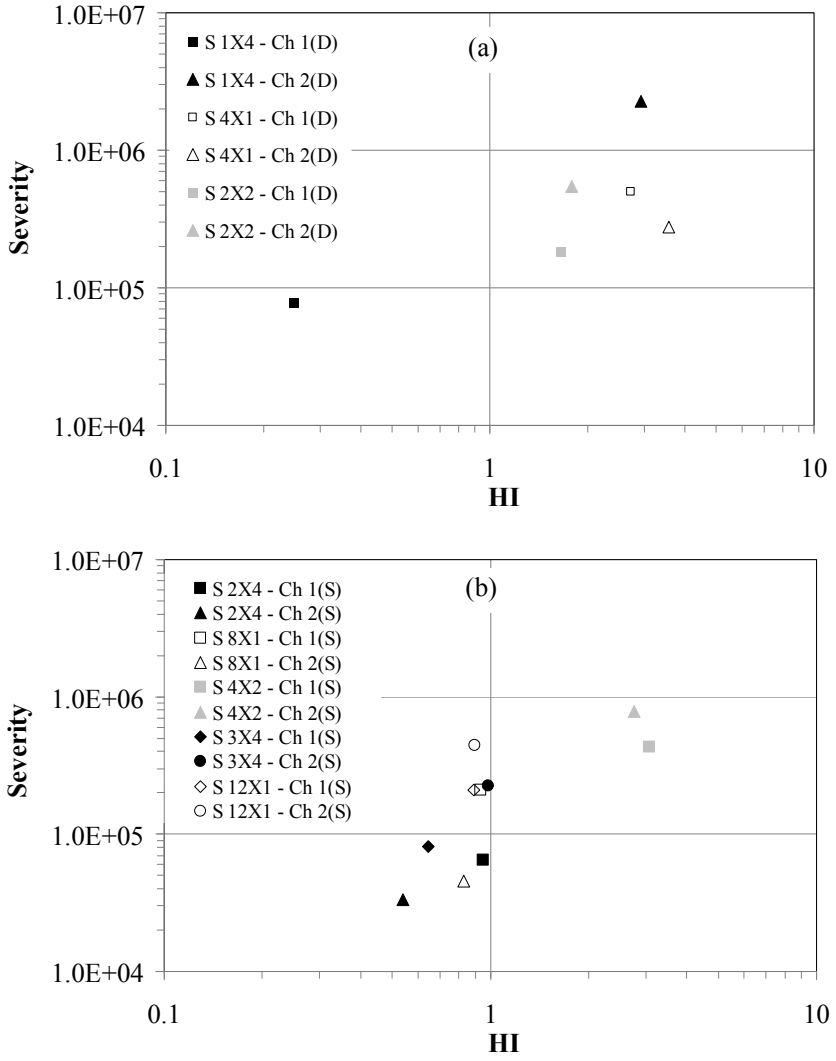

Figure 6-1 Intensity charts for all specimens discussed. (a) Slabs that failed due to CFRP debond. (b) Slabs that failed due to shear. In the legend (D) indicates slabs that failed due to debonding and (S) identifies those slabs that failed due to shear.

Rather than plotting the final maximum value of HI and severity for each sensor, the maximum values observed during the loading-to-failure test were plotted in Figure 6-2 for the slab specimen group that experienced CFRP debonding (1x4, 4x1, and 2x2) and other slab specimen group that experienced shear failure (2x4, 8x1, 4x2, 3x4, and 12x1). The progression of the intensity values moving from lower-left of

the chart to the upper-right can be used in real-time to flag combinations of HI and S_r which enter an intensity zone associated with severe damage. Although the slabs discussed in this study were slightly different to each other, the results from the intensity charts show promise for the application to provide quantitative information on the identification of areas of large damage and on the ability to classify different sources of damage.

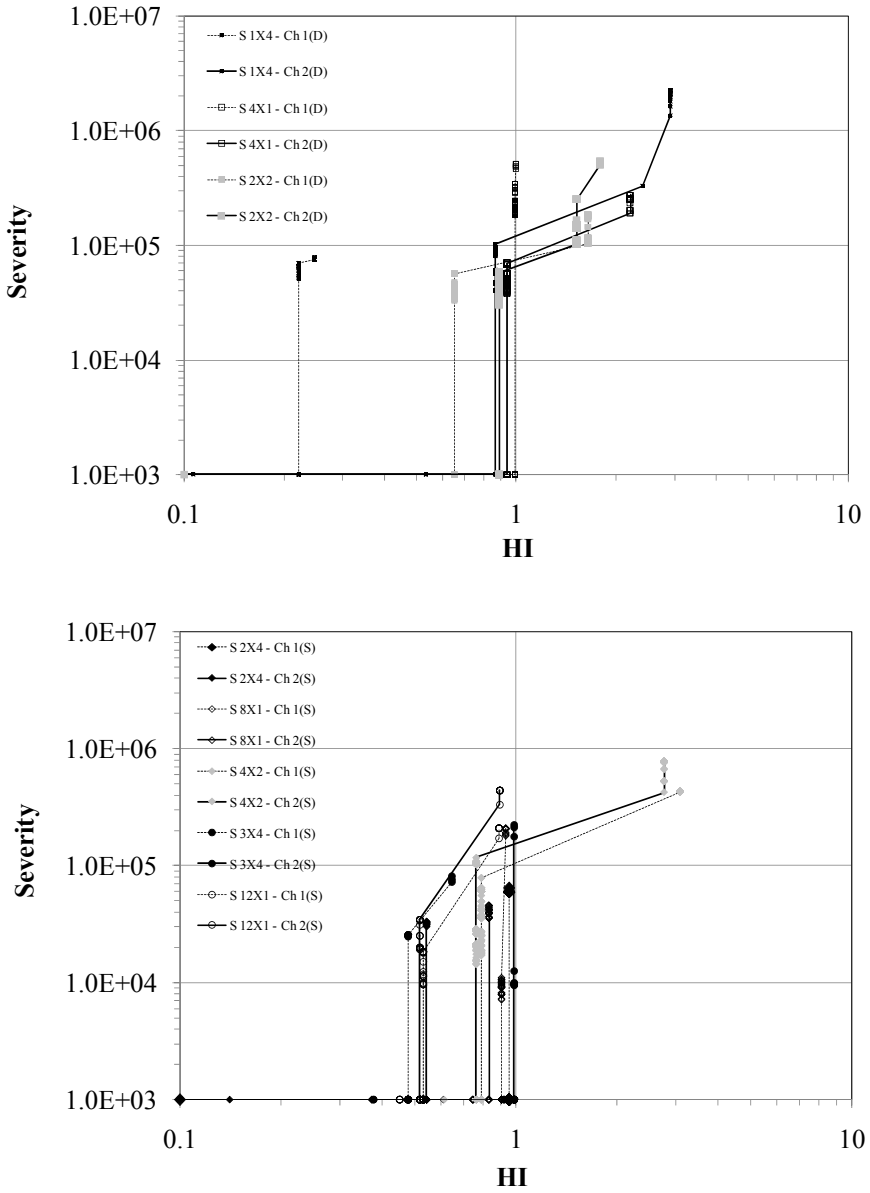

Figure 6-2 Progression of the intensity chart during quasi-static loading to failure of slabs. In the legend (D) indicates slabs that failed due to debonding and (S) identifies those slabs that failed due to shear.

The application of PCA to reduce the dimensionality of AE data in CFRP-retrofitted RC slabs is a novelty. Figure 6-3 shows the PCA visualization of the AE data for slabs 1x4, 4x1, 2x2 (Figure 6-3a, 6.3c, and 6.3e), 2x4, 8x1, and 6x2 (Figure 6-3b, 6.3d, and 6.3f).Overall it was observed that the PCA components scattered towards quadrants 1 and 4 (positive values of the first principal component) for slabs that experienced shear failure whereas the clustering of AE data from the slabs experienced debonding scattered towards quadrants 2 and 3. The reason for this kind of clustering concentrated at a single location and scattering towards different quadrants with respect to the damage can be associated to the type of damage observed in these specimens: flexural cracking in the concrete matrix, cracks in the adhesive layer, and CFRP debonding. This approach showed some degree of correlation between the type of failure and the location of the cluster in the plot of the first two principal components. However the reason of such behavior needs to be fully understood prior to field implementation of this approach.

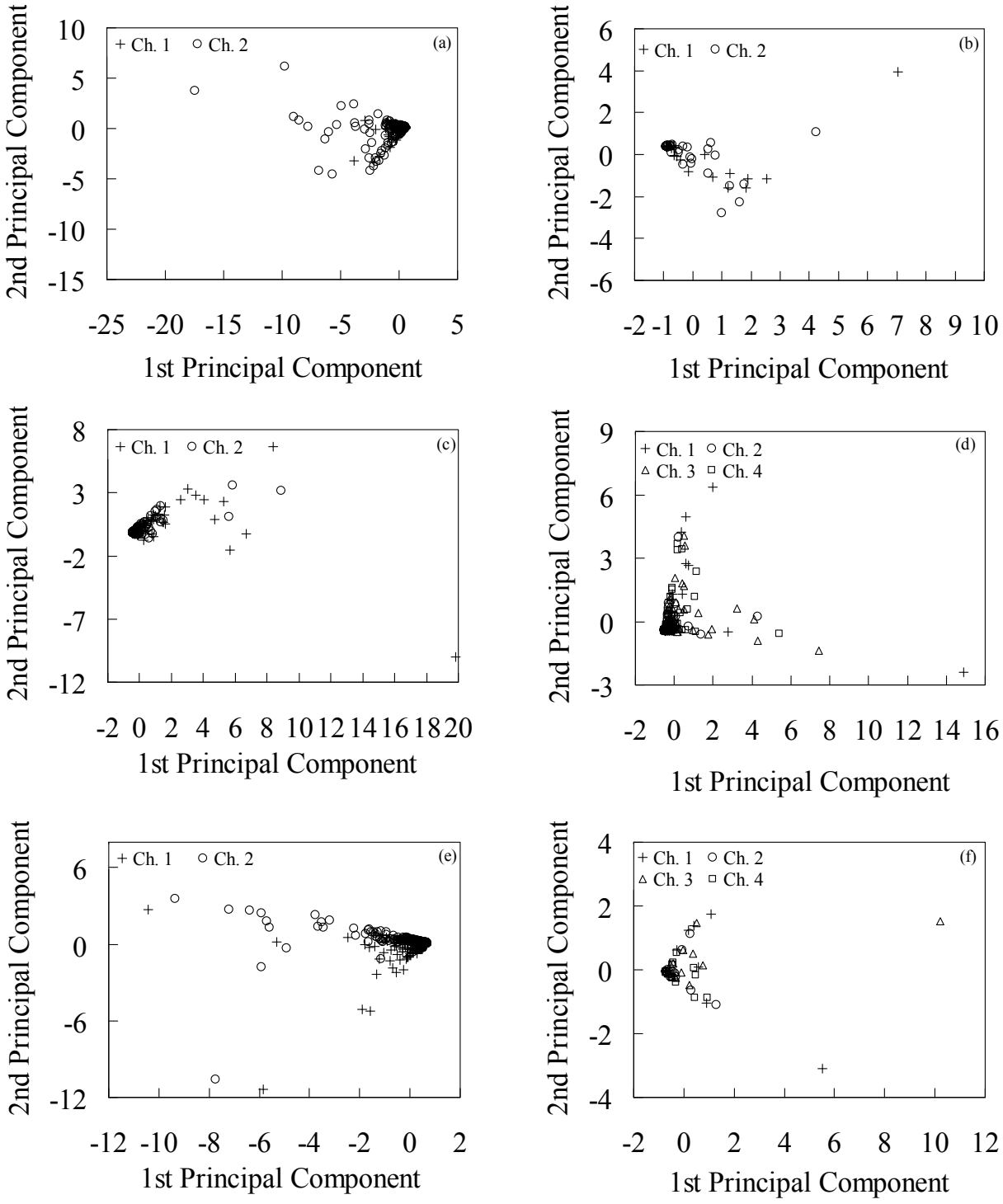

Figure 6-3 PCA reduction of standardized traditional AE features from AE monitoring of slab specimens 1x4, 4x1, 2x2 (a, c, and e), 2x4, 8x1, and 6x2 (b, d, and f).

7.0 ACOUSTIC EMISSION OF STEEL REINFORCING BARS

7.1 INTRODUCTION

A steel reinforcing bar (rebar) is an essential component of reinforced concrete structures. It is usually formed of carbon steel and available in ribbed shape to provide better mechanical bond to the concrete. Steel rebars provide reinforced concrete the tensile strength, stiffness, and ductility needed to make it efficient, durable and safe building material.

The structural response of an ASTM A615 steel rebar subjected to tensile test can be schematized through the engineering stress-strain (similar to load-displacement) curve in Figure 7-1 where four main regions are visible. These regions are: elastic, yielding, strain hardening, and necking and failure.

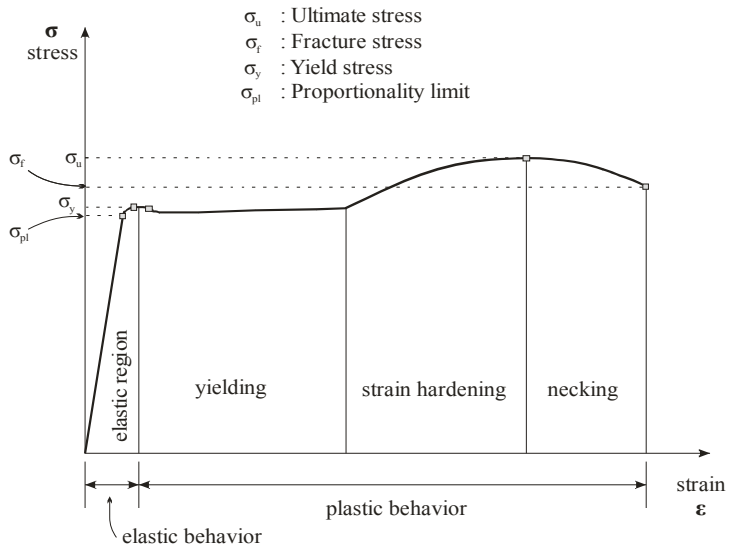

Figure 7-1 Plot showing the general behavior of steel rebar under tension

When the load (stress) is applied, a proportional strain is observed i.e., the initial behavior is linear. This behavior is termed as linear-elastic as the specimen would essentially regain its original state once the load is removed. As the stress is increased, the specimen eventually deviates from its linear proportionality, the point of departure being termed the proportional limit, σ_{pl}. This nonlinearity is usually attributed to stress-induced "plastic" flow in the material mainly associated with a rearrangement of its internal molecular or microscopic structure, in which atoms are being moved to new equilibrium positions. These micro structural rearrangements associated with plastic flow are usually not reversed when the load is removed, so the proportional limit is often the same as or at least close to the material's yield stress. The yield stress, σ_y is the stress needed to induce plastic deformation in the specimen. Since it is often difficult to pinpoint the exact stress at which plastic deformation begins, the yield stress is often taken as the intersection of the vertical line drawn parallel to the stress axis at 0.5% of the strain (not shown here). Beyond the yield region, the material requires an ever-increasing stress to continue straining, a mechanism termed strain hardening. Once the curve reaches ultimate stress, σ_u, the cross sectional area of the specimen starts reducing and localized reduction in that area leads to necking in the gage length. On further increase of strain, the specimen fails, termed as fracture, σ_f. It should be emphasized that the extent of each region explained above in stress-strain space is specimen dependent.

Tension tests provide information on the strength and ductility of materials. Such information is useful in material's quality control, structural analysis and design. The major threat to a structure's integrity is the crack occurrence due to the material's permanent deformation and it is also the best recognized source of high amplitude AE (Hellier 2001).

Four ASTM A615 steel rebar specimens were tested in the laboratory to assess and quantify the damage under tensile loading conditions. The objective was to monitor the AE activity of rebar under tension and to characterize the regions identified in Figure 7-1 by means of AE. The PA and IA approaches were used. Study on AE monitoring of steel specimens under tension were reported by Mukhopadhyay et al. (1993, 1998).

In commercial grade flat stainless steel specimens, the AE is generated by the motion of dislocations and fracture of non-metallic inclusions (Mukhopadhyay et al. 1998). AE occurs during tensile deformation of stainless steel due to transient rapid release of energy from localized sources, such as regions of relaxation of stress and strain fields. AE generated during tensile deformation strongly depends on the micro structural features, deformation processes and phase transformations (Mukhopadhyay et al. 1993).

7.2 EXPERIMENTAL SETUP AND TESTING PROTOCOL

Axial tensile tests were conducted to determine and monitor the behavior of three different sizes of steel rebars (#4, #5, and #6). A total of 4 specimens were tested in tension. All the tests were conducted in the Watkins Haggart Structural Engineering Laboratory at the University of Pittsburgh. The sequential order of the tested rebar, rebar size and length, the theoretical values of the yield strength and ultimate strength of rebar, the final displacement observed and the rupture load are summarized in Table 7-1.

Table 7-1 Summary of observations from rebar tensile tests.

Steel rebar. No.	Rebar size	Length (ft)	Experimentally observed yield and ultimate stress (ksi)	Final Displacement (inch)	Peak (rupture) load (kips)
1[1]	#4	4	61.0 , --	0.48	12.9
2 [1]	#5	4	64.5 , --	0.46	20.4
3 [1]	#6	4	62.5 , --	0.53	28.0
4 [2]	#6	8	61.3 , 95.4	6.40	43.1 (rupture)

[1] Rebar under tension loaded up to its yield strength
[2] Rebar under tension loaded up to failure
-- represents that ultimate stress was not observed as those rebars were not loaded until rupture.

The same suite of AE instrumentation used to monitor the mechanism failure of RC retrofitted with CFRP was adopted in this study. Four AE transducers were used (three PAC-WD wideband transducers and one

PICO transducer). The sensor arrangement information, number of transducers used for different tests, and AE settings are summarized in Table 7-2.

Table 7-2 AE Sensor arrangement and software settings

Steel rebar. No.	No. of transducers	Type and position of the transducers	AE Settings		
			PDT	HDT	HLT
1	4	One WD [1] [1] at top and one WD [2] at bottom and a WD [4] and PICO [3] on the circumference of rebar close to top end	300	600	1000
2	3	One WD [1] at top and one WD [2] at bottom and a PICO [3] on the circumference of rebar close to top end	300	600	1000
3	4	One WD [1] at top and one WD [2] at bottom and a WD [4] and PICO [3] on the circumference of rebar close to top end	300	600	1000
4	2	Two WDs at top [1] and bottom [2]	300	600	1000

[1] Channel/Transducer number denoted in [ ]

A 200 kips (890 kN) Baldwin universal testing machine (UTM) was used under displacement control. Rebars 1, 2, and 3 were subjected to cyclic tensile load until yielding while rebar 4 was subjected to cyclic tensile load until failure. The displacement was monitored using a draw wire transducer (DWT) secured to the moving cross head of the UTM. AE transducers were mounted at the top and bottom of the specimen using hot glue. A figure representing the test setup for the tensile testing of rebars with 4 ft height is shown in Figure 7-2. Also photographs of the test setup and the AE sensor arrangement over the top of the rebars are shown in Figure 7-3.

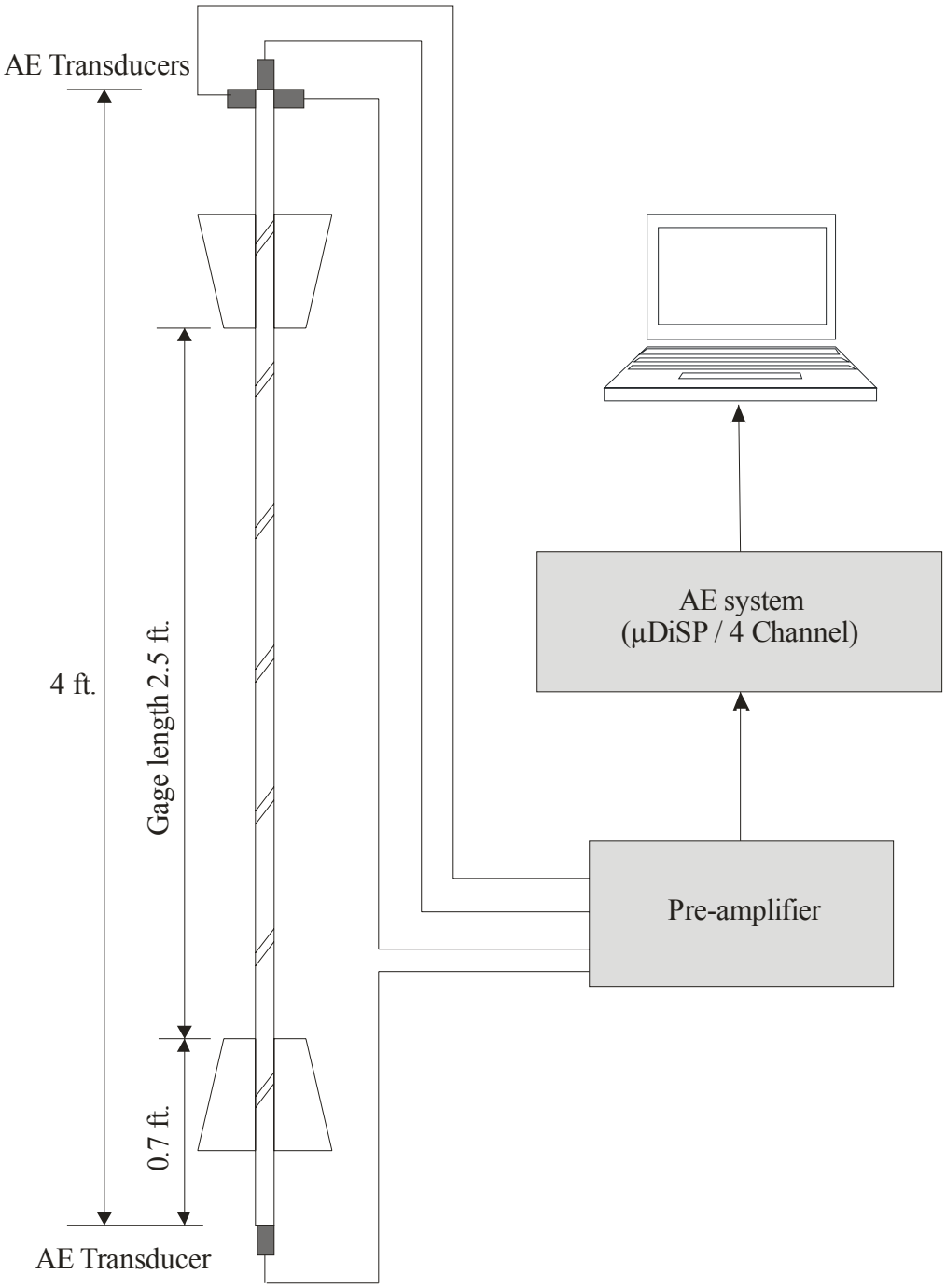

Figure 7-2 Details of the test setup

(a) Test setup

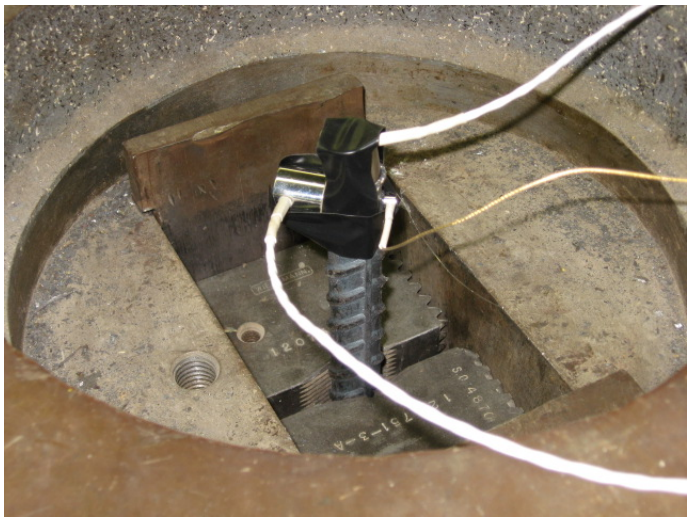

(b) AE sensor arrangement on top of rebar

Figure 7-3 Photographs of the test setup and AE sensor arrangement

7.3 EXPERIMENTAL RESULTS

7.3.1 Steel rebar 1

Counts, cumulative energy, and amplitude of the acoustic activity are plotted as functions of time in Figure 7-4(a, b, c). The plot of total applied load is also superimposed on the plot of acoustic count history. The load-displacement history is shown in Figure 7-4d.

The rebar was loaded up to its yield strength with a series of load-unload cycles. From Figure 7-4(a, b, c), it can be seen that from the initial phase of loading, until about 180 seconds high AE activity can be seen. This can be characterized with an AE count of about 1500 and amplitude of 80dB. This

activity can be associated to the initial elongation in the rebar due to tensile loading. Between 185 and 205 seconds the specimen's displacement was held constant. Upon reloading the specimen at 300 seconds, the acoustic activity is not seen until the applied load reaches the previous peak load of 6.08 kips (27 kN) at 333 seconds. At this juncture, the Kaiser effect is seen, i.e. no acoustic activity was seen prior to crossing the peak load. This effect was observed from all AE parameters considered. The cumulative energy shows a constant line in the time frame of 300-333 seconds which supports the evidence of Kaiser Effect as no energy is released from the specimen upon second phase of reloading. The displacement was again held at about 370 seconds until 380 seconds corresponding to a load of about 11.04 kips (49.5 kN) upon which the specimen was unloaded. Again after 528 seconds the specimen was reloaded and the subsequent load passes previous peak load of 11.04 kips (49.5 kN) at 605 seconds. Although the counts show some activity just before the peak load, the cumulative energy and amplitude provides the evidence of Kaiser Effect as the constant line of cumulative energy was constant from 528 seconds to 605 seconds and also amplitude shows no activity in the time frame of 528-600 seconds. The third loading ramp was completed at 12.90 kips (57.5 kN) slightly above the theoretical yield strength. However, significant AE activity corresponding to the initiation of yield in the rebar was not seen at the observed yield point from the applied load profile. The acoustic activity released for the unloading phase is reducing from cycle to cycle. It can be noticed that the counts and amplitude associated with the unloading phase reduces significantly in subsequent cycles. This can be clearly seen from Figure 7-4a and Figure 7-4c where the AE counts and AE amplitudes corresponding to the unloading phase of the second cycle are lower when compared to the first cycle. Similar results are seen in the third cycle in comparison with the second and first cycles. As the AE sensors in channels 1 and 2 were attached at each rebar's cross-section end, they sensed the in-plane displacement of the propagating longitudinal mode. AE sensors in channels 3 and 4 were located on the circumference of the rebar close to channel 1. As such AE sensors 3 and 4 mainly detected the out-of-plane displacement of the propagating stress waves, which is lower than the in-plane displacement. Thus the activities from channels 3 and 4 were expected to be lower than the AE activities detected by channels 1 and 2.

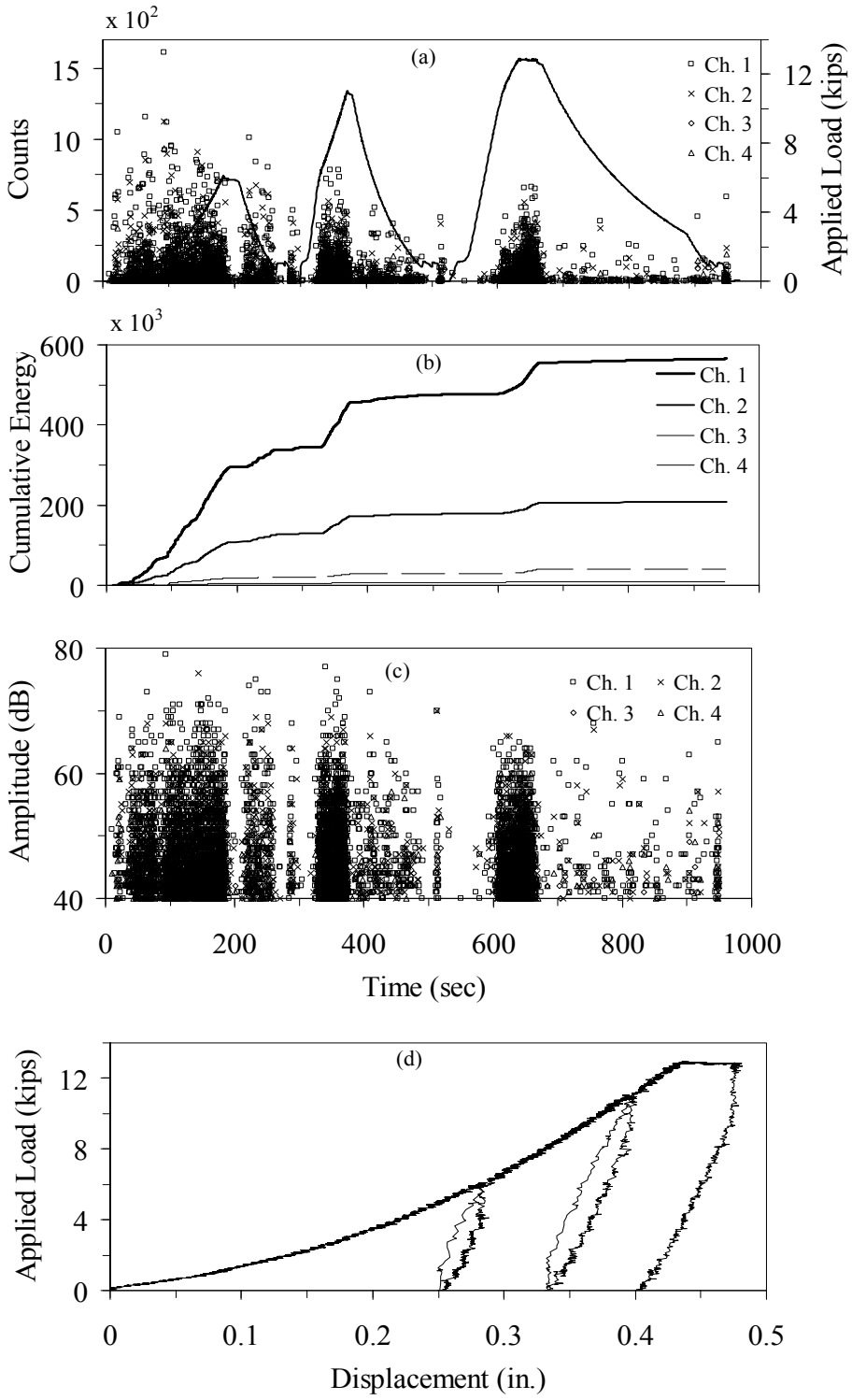

Figure 7-4 Acoustic emission results during repetitive loading for #4 steel rebar (test-1). Counts and applied load (a), cumulative energy (b), and amplitude (c) as a function of time. (d) Load vs. displacement plot

Figure 7-5 shows the locations of the AE sources as function of time clustered on the basis of amplitude determined using a linear algorithm. In order to identify the location of AE source, a set of preliminary pencil lead break tests were conducted to set the wave velocity. The speed was set to 4.5 km/sec. The time occurrence of the event is plotted as a function of the X position (longitudinal) along the rebar. Event amplitudes between 40-100 dB and 55-100 dB are distinguished in Figure 7-5a and b respectively. Although, the AE events generated during the elongation of rebar is visualized from Figure 7-5a, it can be observed that higher amplitudes are mainly localized near the grips (Figure 7-5b).

Figure 7-6a and b shows HI as a function of time for the steel rebar-1. The plot of the CSS is superimposed. At 220 seconds, 330 seconds, 600 seconds, change in the slopes of the CSS line resulted in decrease of historic index. The occurrence at 220 seconds was due to the manual release of unloading knob in the test machine, whereas the occurrences at 330 seconds and 600 seconds were associated to the crossing of the maximum loads. This phenomenon is directly related to Kaiser Effect. The decrease of historic index at time intervals 330-390 seconds, 600-650 seconds can also be seen. These occurrences were compared to the severity plot beside HI plot. The change of load profile was identified to be the onset for the decrease of HI. The increase in HI at 620 seconds corresponds to initiation of yield in the rebar, at a load of about 12.9 kips (Figure 7-6b). This can be validated from the load-displacement plot, wherein the yield can be seen to occur at a load of approximately.12.9 kips, when the load was constant with increasing displacement. There was no significant indication of severity after 350 seconds (Figure 7-6c), but the initial strain developed in rebar can be seen from the first sequence of loading. Figure 7-6d shows the maximum HI and severity values plotted on log-log scale.

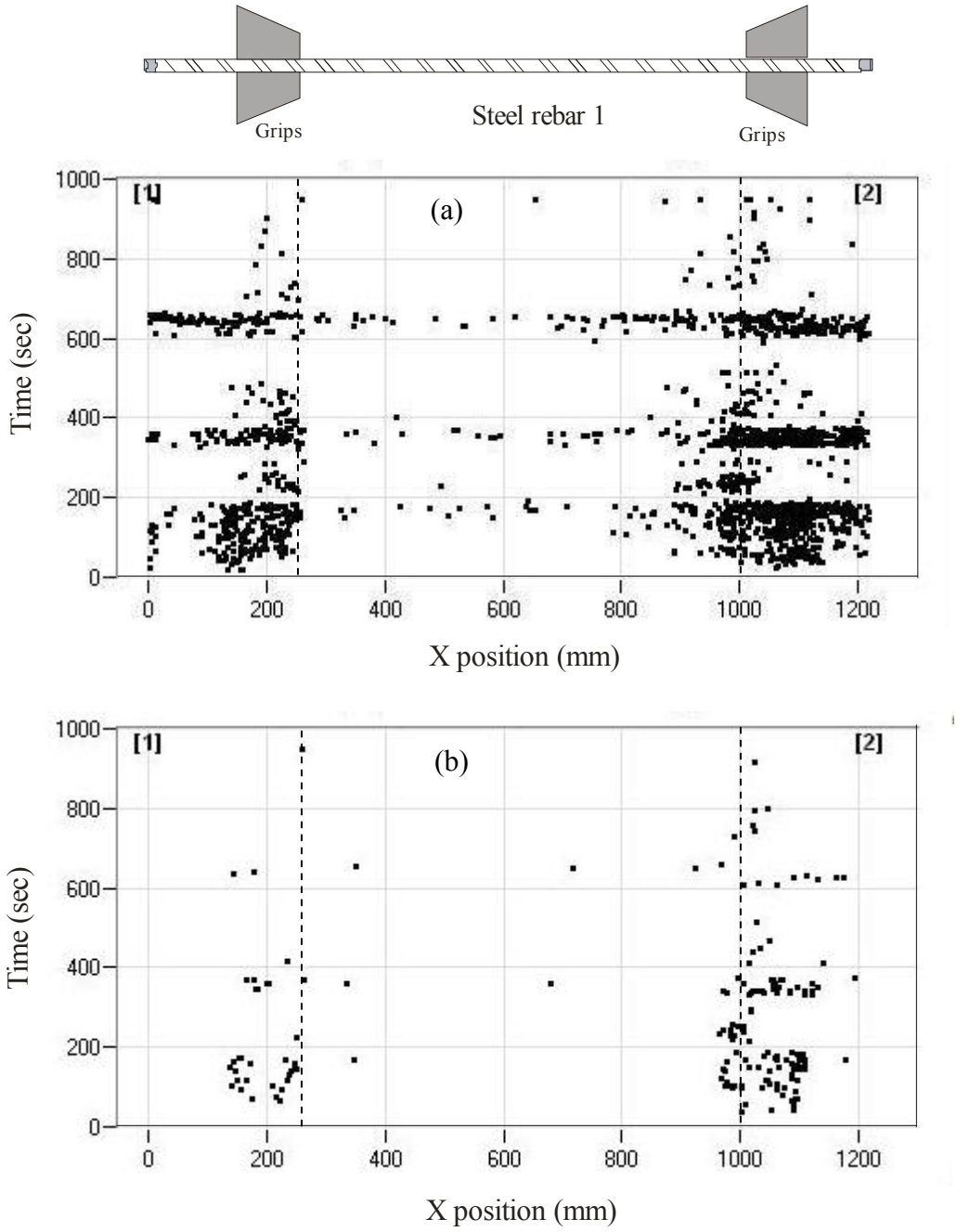

Figure 7-5 AE source location as a function of time for steel rebar 1: (a-b) AE amplitudes in the range 40-100 dB (a) and 55-100 dB (b) are discriminated.

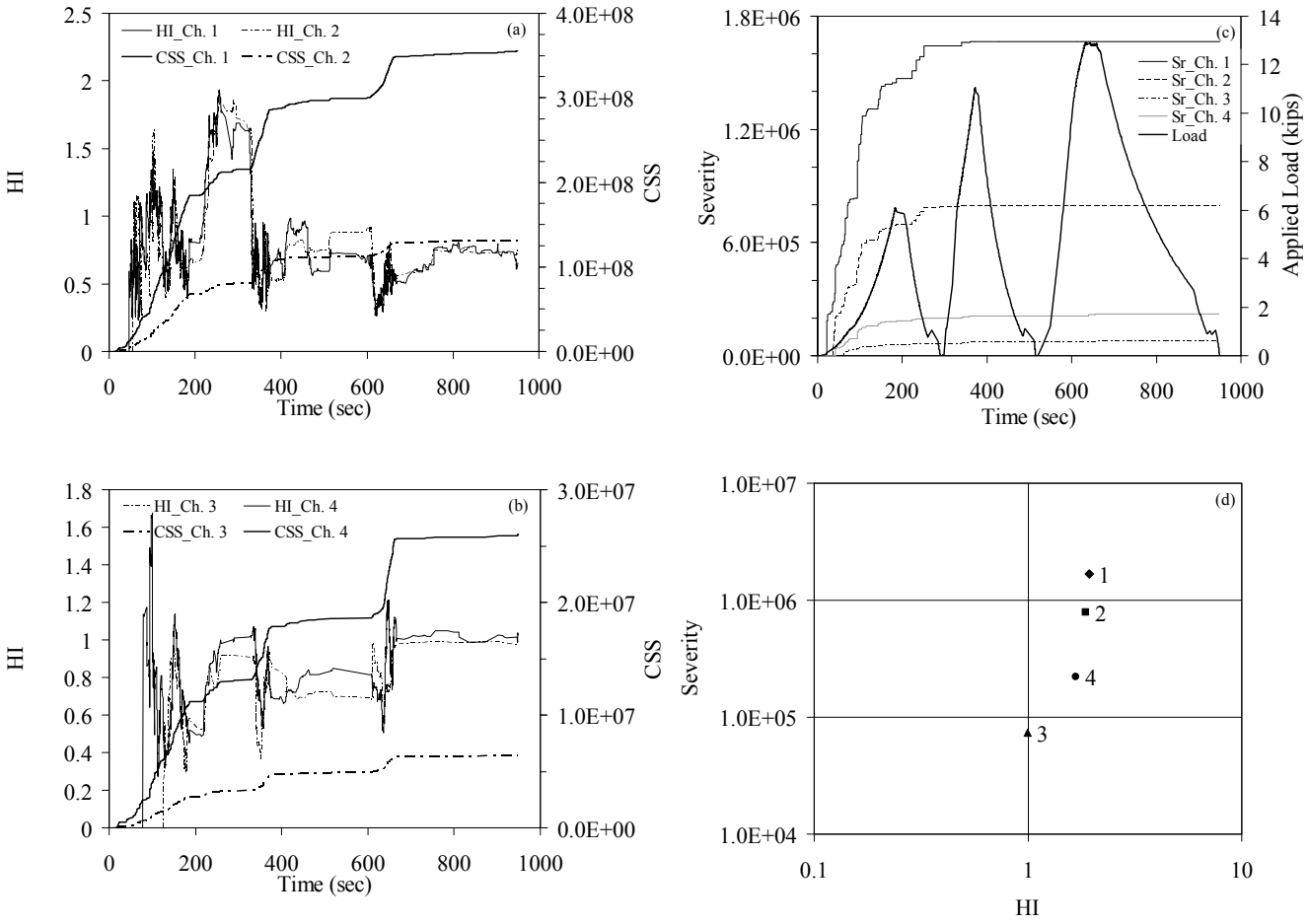

Figure 7-6 Intensity analysis for steel rebar 1. (a-b) Historic index as a function of time. The plot of the cumulative signal strength is superimposed. (c) Severity index as a function of time. The plot of the applied load is superimposed. (d) Intensity chart.

7.3.2 Steel rebar 2

A #5 rebar was subjected to four load-unload cycles. During the fourth cycle the theoretical yield strength was exceeded. Counts, cumulative energy, and amplitude of the acoustic activity are plotted as functions of time in Figure 7-7(a, b, c). The plot of total applied load is also superimposed on the plot of acoustic count history. The load-displacement history is shown in Figure 7-7d. Three AE transducers were used following the scheme described in Table 7-2.

From Figure 7-7 (a, b, c), it can be seen that from the initial phase of loading, until about 80 seconds high AE activity can be seen. This can be characterized with an AE count of about 1300 and amplitude of 75dB. This activity can be associated to the initial elongation in the rebar due to tensile loading. During the second cycle AE activity was observed only after the applied load exceeded the previous peak load of 5.06 kips. This behavior was associated with the Kaiser effect and was observed also in the last two cycles. The cumulative energy shows no activity in the time frames of 236-276 seconds, 504-544 seconds, and 680-725 seconds which supports the evidence of Kaiser Effect as no energy is released from the specimen. AE amplitude also depicts the same. Also, significant AE activity corresponding to the initiation of yield in the rebar was not seen at the observed yield point from the applied load profile. The acoustic activity released for the unloading phase is reducing from cycle to cycle. A maximum load of 20.4 kips was applied on the specimen.

Figure 7-8 shows the locations of the AE sources as function of time clustered on the basis of amplitude determined using a linear algorithm. Event amplitudes between 40-100 dB and 55-100 dB are distinguished in Figure 7-8a and b respectively. Although, the AE events generated during the elongation of rebar is visualized from Figure 7-8a, it can be observed that higher amplitudes are mainly localized near the grips (Figure 7-8b).

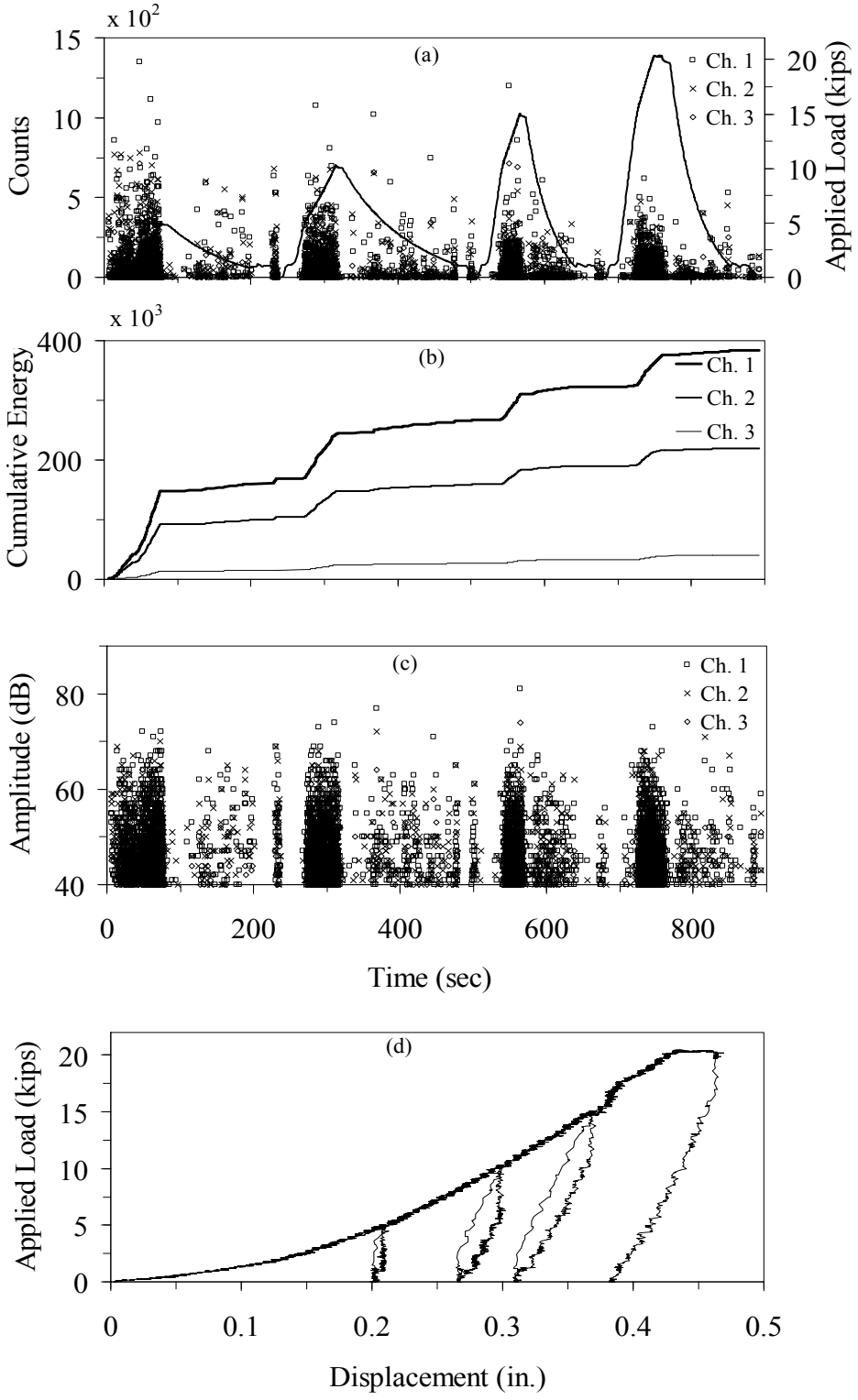

Figure 7-7 Acoustic emission results during repetitive loading for #5 steel rebar (test-2). Counts and applied load (a), cumulative energy (b), and amplitude (c) as a function of time. (d) Load vs. displacement plot

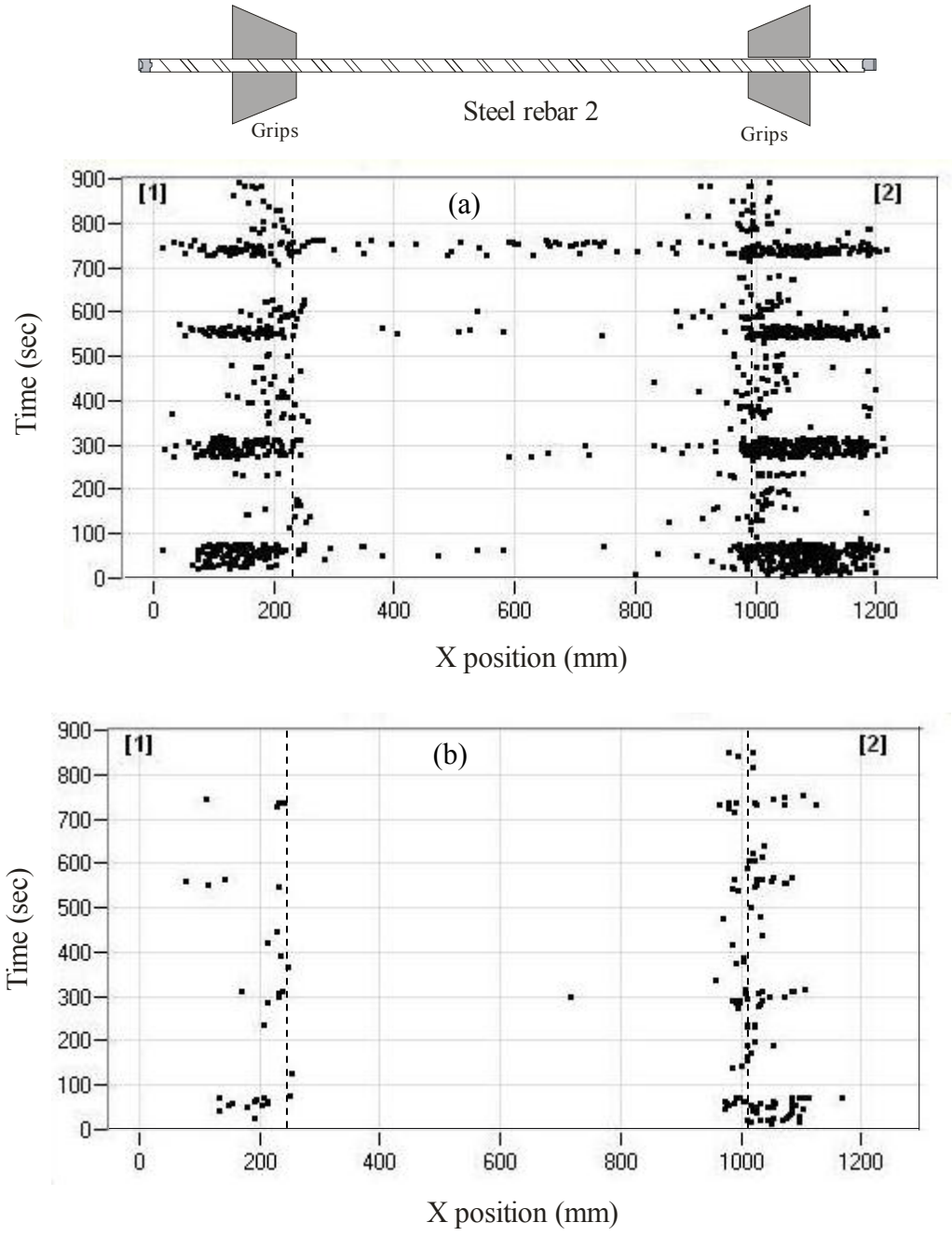

Figure 7-8 AE source location as a function of time for steel rebar 2: (a-b) AE amplitudes in the range 40-100 dB (a) and 55-100 dB (b) are discriminated.

Figure 7-9 shows the intensity analysis charts. Figure 7-9a shows HI as a function of time for the steel rebar-2. The plot of the CSS is superimposed. The behavior is similar to that explained in Figure 7-6, Section 7.3.1. However, significant change in the values of HI indicating the initiation of yield in rebar was not seen. The general trend of the intensity chart is readily observed. In Figure 7-9c the fact that the value from sensor 1 is in the upper right corner compared to the value from sensor 2 suggests that the greater amount of activity occurred in the area of sensor 1.

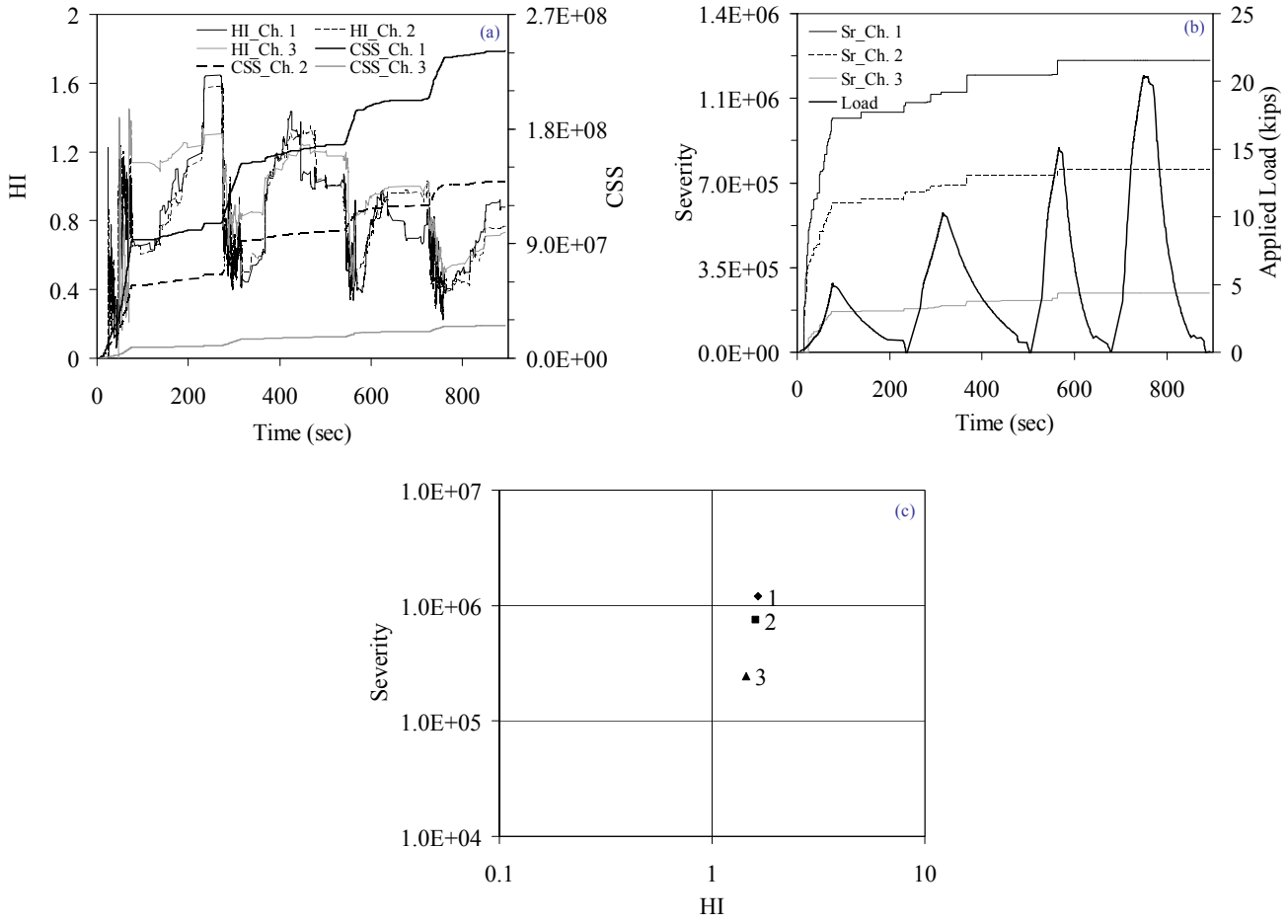

Figure 7-9 Intensity analysis for steel rebar 2. (a) Historic index as a function of time. The plot of the cumulative signal strength is superimposed. (b) Severity index as a function of time. The plot of the applied load is superimposed. (c) Intensity chart.

7.3.3 Steel rebar 3

A #6 rebar was subjected to five load-unload cycles. During the fifth cycle the applied stress exceeded the theoretical yield strength of the specimen. As for steel rebar-1, four AE sensors were attached to the rebar. Counts, cumulative energy, and amplitude of the acoustic activity are plotted as functions of time in Figure 7-10. The plot of total applied load is also superimposed on the plot of acoustic count history. The load-displacement history is shown in Figure 7-10d.

During the first cycle, the specimen was loaded at constant displacement rate. From Figure 7-10 (a, b, c), it can be seen that from the initial phase of loading, until about 70 seconds high AE activity can be seen. This can be characterized with an AE count of about 2400 and amplitude of 85 dB. This activity can be associated to the initial elongation in the rebar due to tensile loading. At about 70 seconds the displacement was held constant until 120 seconds beyond which it was reversed. All cycles show the evidence of Kaiser Effect with respect to the acoustic parameters. The cumulative energy shows no activity in the time frames of 325-404 seconds, 645-780 seconds, 1015-1060 seconds, 1229-1289 seconds which supports the evidence of Kaiser Effect. Contrary to the previous specimens with same loading conditions, in this case the cumulative energy (Figure 7-10b) clearly establishes the onset of yielding in the rebar. As seen in Figure 7-10b, this is evident from the jump in the cumulative energy curve at about 1290 seconds. A maximum load of 28.03 kips (124.75 kN) was applied on the specimen.

Figure 7-11 shows the locations of the AE sources as function of time clustered on the basis of amplitude determined using a linear algorithm. Event amplitudes between 40-100 dB and 55-100 dB are distinguished in Figure 7-11a and b respectively. Although, the AE events generated during the elongation of rebar is visualized from Figure 7-11a, it can be observed that higher amplitudes are mainly localized near the grips (Figure 7-11b).

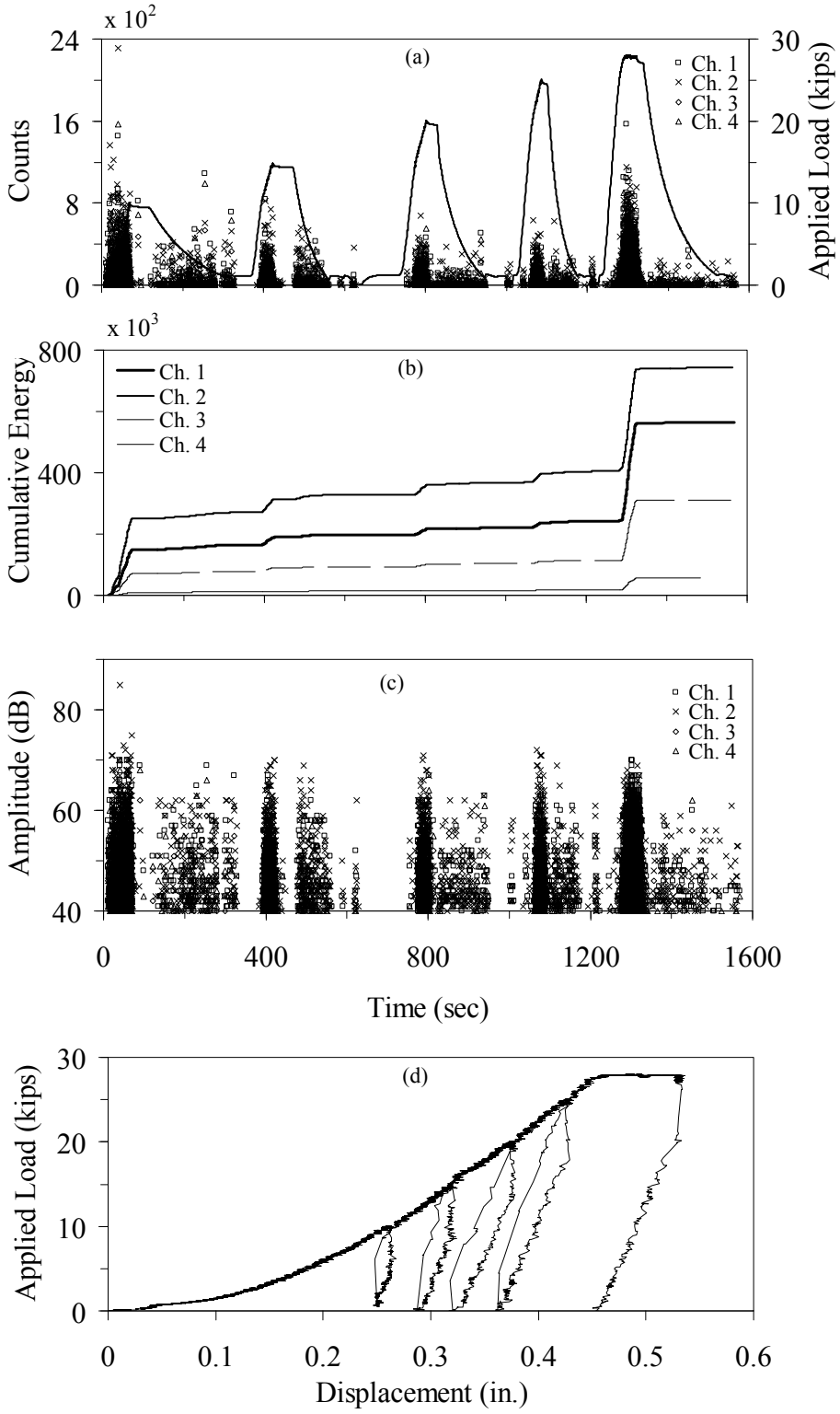

Figure 7-10 Acoustic emission results during repetitive loading for #6 steel rebar (test-3). Counts and applied load (a), cumulative energy (b), and amplitude (c) as a function of time. (d) Load vs. displacement plot.

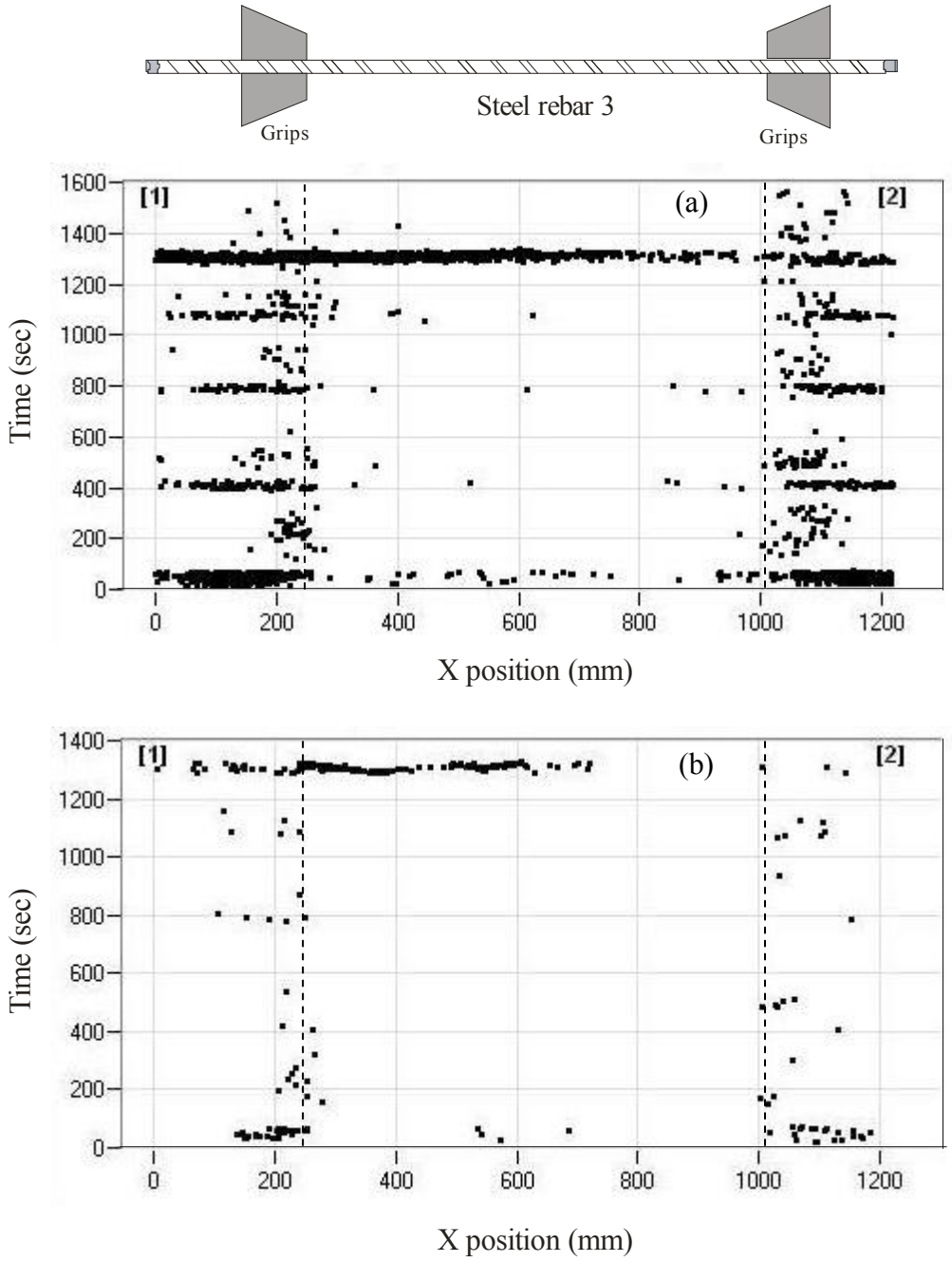

Figure 7-11 AE source location as a function of time for steel rebar 3: (a-b) AE amplitudes in the range 40-100 dB (a) and 55-100 dB (b) are discriminated.

Figure 7-12a and b shows HI as a function of time for the steel rebar-3. The behavior is similar to that explained in Figure 7-6, Section 7.3.1. It can be seen from the intensity chart that higher intensity value is located towards AE transducer in channel 2 (Figure 7-12d).

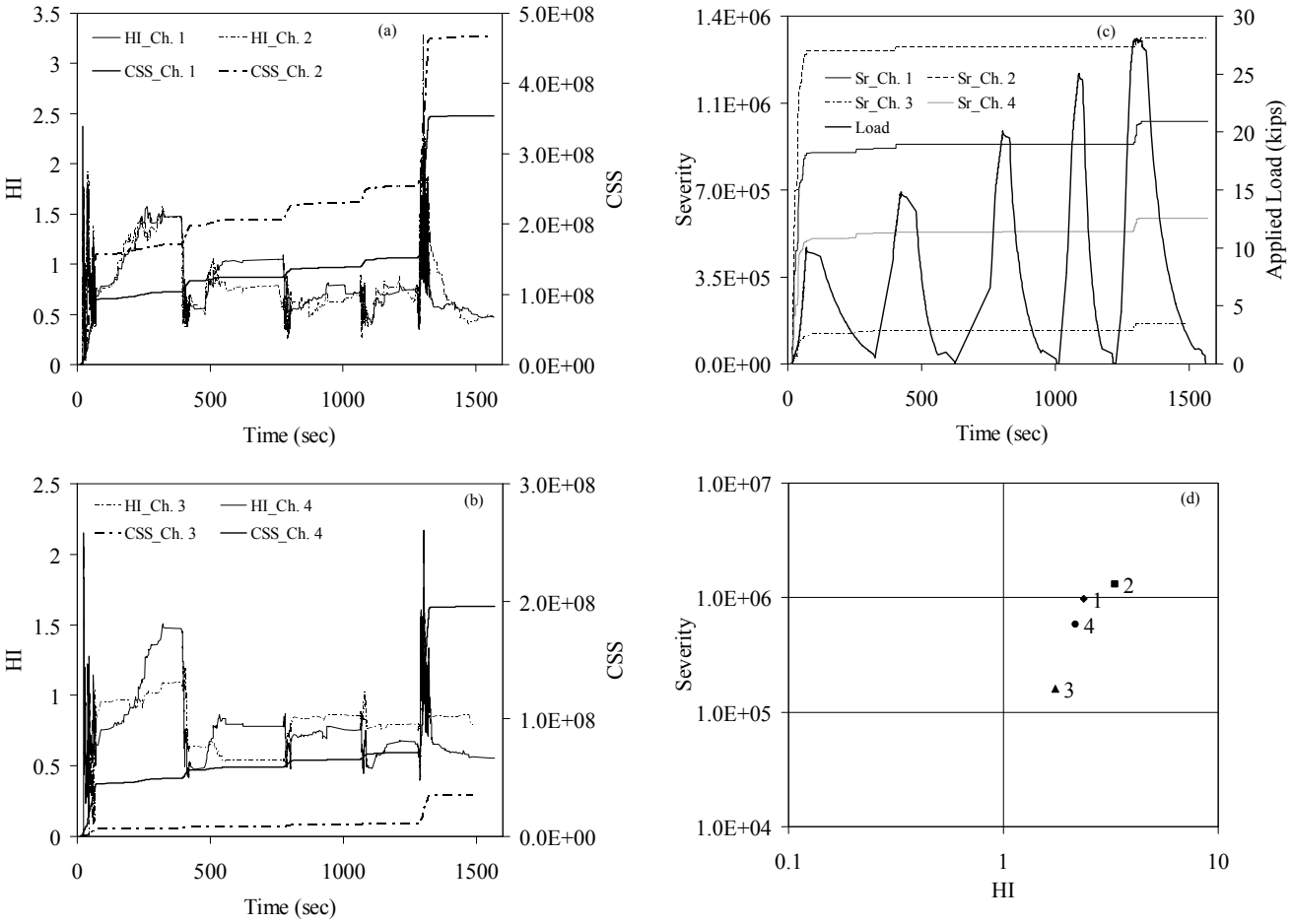

Figure 7-12 Intensity analysis for steel rebar 3. (a-b) Historic index as a function of time. The plot of the cumulative signal strength is superimposed. (c) Severity index as a function of time. The plot of the applied load is superimposed. (d) Intensity chart.

7.3.4 Steel rebar 4

A #6 rebar was subjected to tensile loading. Load hold method was introduced to differentiate the AE activity for different phases of structural response of the rebar. Overall, the testing comprised of two load holds, as explained in subsequent paragraph. Counts, cumulative energy, and amplitude of the acoustic activity are plotted as functions of time in Figure 7-13. The plot of total applied load is also superimposed on the plot of acoustic count history. Catastrophic failure of the specimen occurred at 43 kips (191.5 kN). The load versus displacement plot is also included for comparison. The rebar was monitored using two AE sensors mounted at each rebar's cross-section end.

The slope of the cumulative energy plot (Figure 7-13b) is flat in the elastic region. The slope of the curve changes at about 680 seconds indicating yield. An increase in the number of AE counts and cumulative energy was observed. The slope of the cumulative energy curve becomes steeper representing strain hardening in the specimen at around 870 seconds. This is also evident from the plots of other counts and amplitude. The number of counts was higher than those in the elastic region. However, no signs of failure were visible although an increase in the AE amplitudes (75-90 dB) was observed. No activity was seen when the displacement was held constant. In general, emissions during load holds are likely indicators of significant damage progression or the interference of electro-magnetic noise (Hellier 2001). AE amplitudes above 90 dB are also observed within 10% of the rebar failure. This behavior demonstrates the potential of AE amplitudes to provide a means to anticipate and predict the failure of rebar.

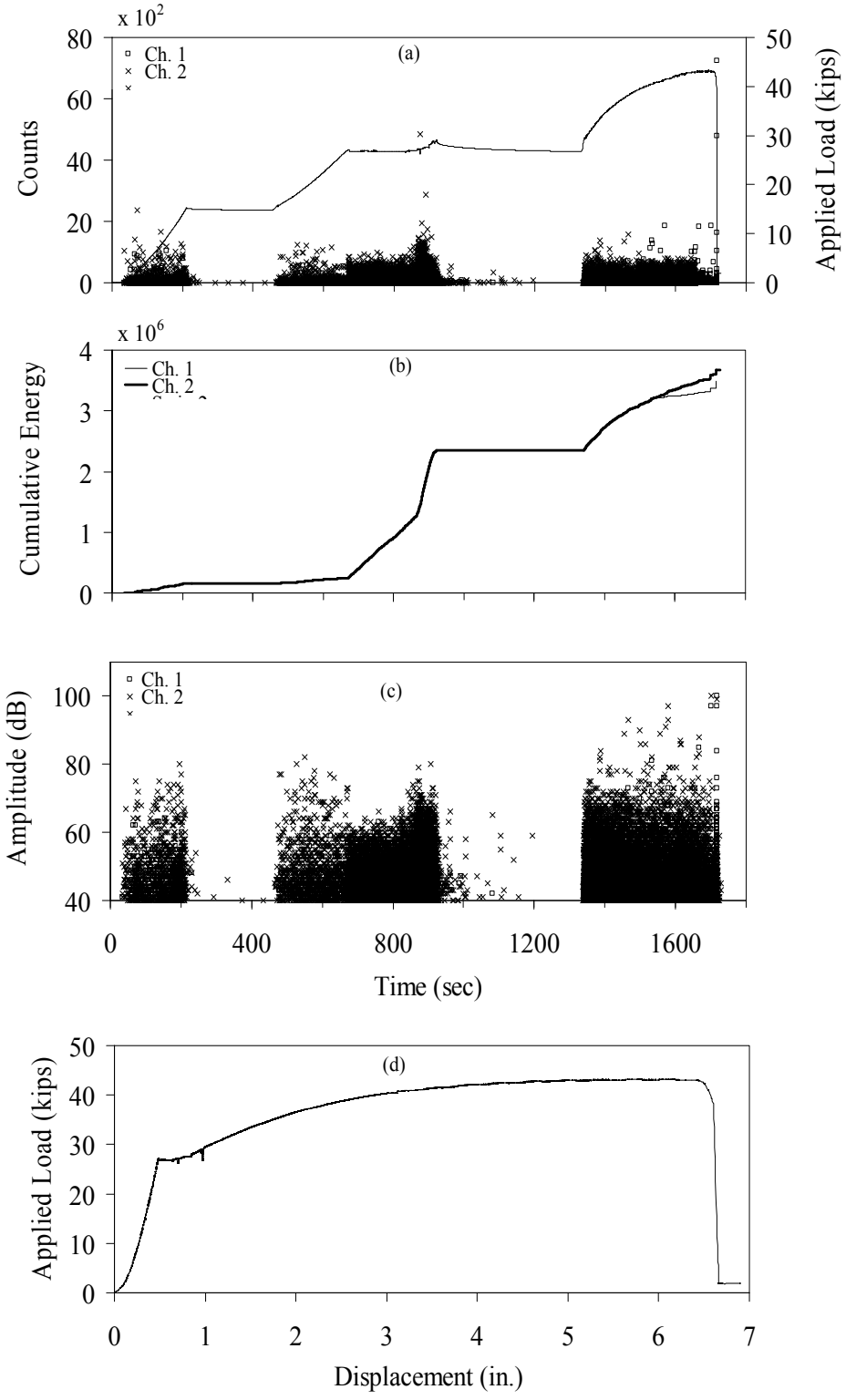

Figure 7-13 Acoustic emission results during repetitive loading to failure for #6 steel rebar (test-4). Counts and applied load (a), cumulative energy (b), and amplitude (c) as a function of time. (d) Load vs. displacement plot.

Figure 7-14 shows the load hold history of the steel rebar 4 with respect to time. The elastic and plastic regions are also identified. The plateau in the curve during the time interval of 220-460 seconds indicates that the applied load was held constant. Hereon the load was increased until about 650 seconds, beyond which the load remained constant at approximately 26.7 kips (119 kN) with an increase in displacement (see Figure 7-13d). This characterizes the yield plateau in the specimen. At about 900 seconds, the load was held constant and then the specimen was loaded again at 1320 seconds. Hereon the load increased with displacement signifying strain hardening in the specimen.

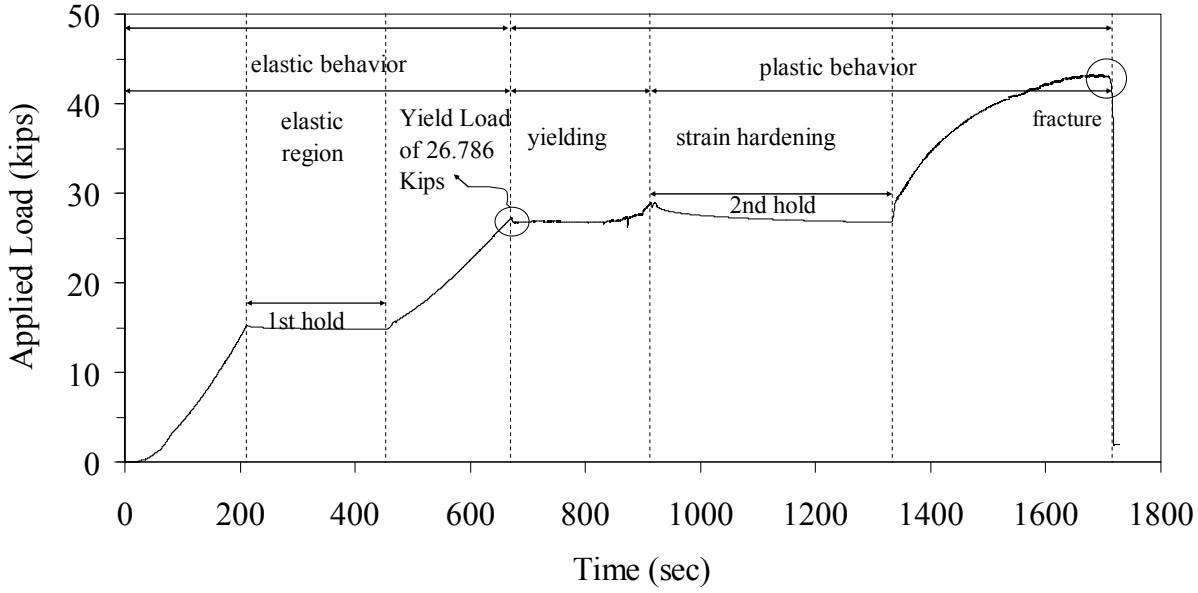

Figure 7-14 Load history for #6 steel rebar (test-4) showing elastic and plastic regions.

Figure 7-15 shows the locations of the AE sources as function of time clustered on the basis of amplitude determined using a linear algorithm. Event amplitudes between 40-100 dB and 55-100 dB are distinguished in Figure 7-15a and b respectively. The AE events are highly localized at the location where

the rebar ruptured finally. All the AE events localized in the stress free area of rebar can be associated with:

1) reflections of the main AE signal from the boundaries; or

2) stress wave having wave velocity different from that of the wave velocity set in the algorithm.

Figure 7-15b validates the generation of AE activity from the rebar between the conical wedge grips on either ends at the time instances where the regions in Figure 7-14 (elastic, yielding, strain hardening and rupture) were observed due to the deformation of the rebar.

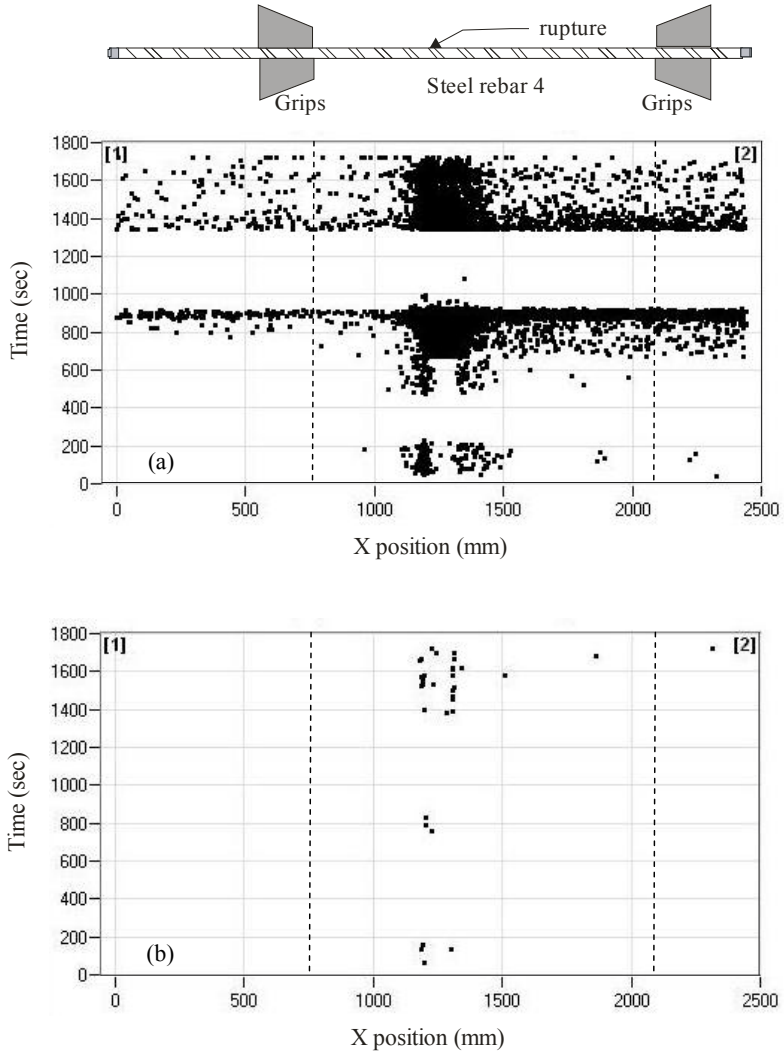

Figure 7-15 AE source location as a function of time for steel rebar 4: (a-b) AE amplitudes in the range 40-100 dB (a) and 55-100 dB (b) are discriminated.

Figure 7-16a shows HI as a function of time for the steel rebar-4. Figure 7-16b is a magnified portion of Figure 7-16a. The plot of CSS is superimposed. The plot associated with channel 2 showed the presence of AE knee (change in slope of CSS) at around 700 and 850 seconds at which the transition from the elastic regime to the yielding regime and from the yielding to the strain-hardening occurred, respectively. The strain hardening region can be identified from the increase in the HI and S_r at around 1250 seconds (Figure 7-16b and Figure 7-16c). Figure 7-16d shows the maximum HI and severity values plotted on log-log scale.

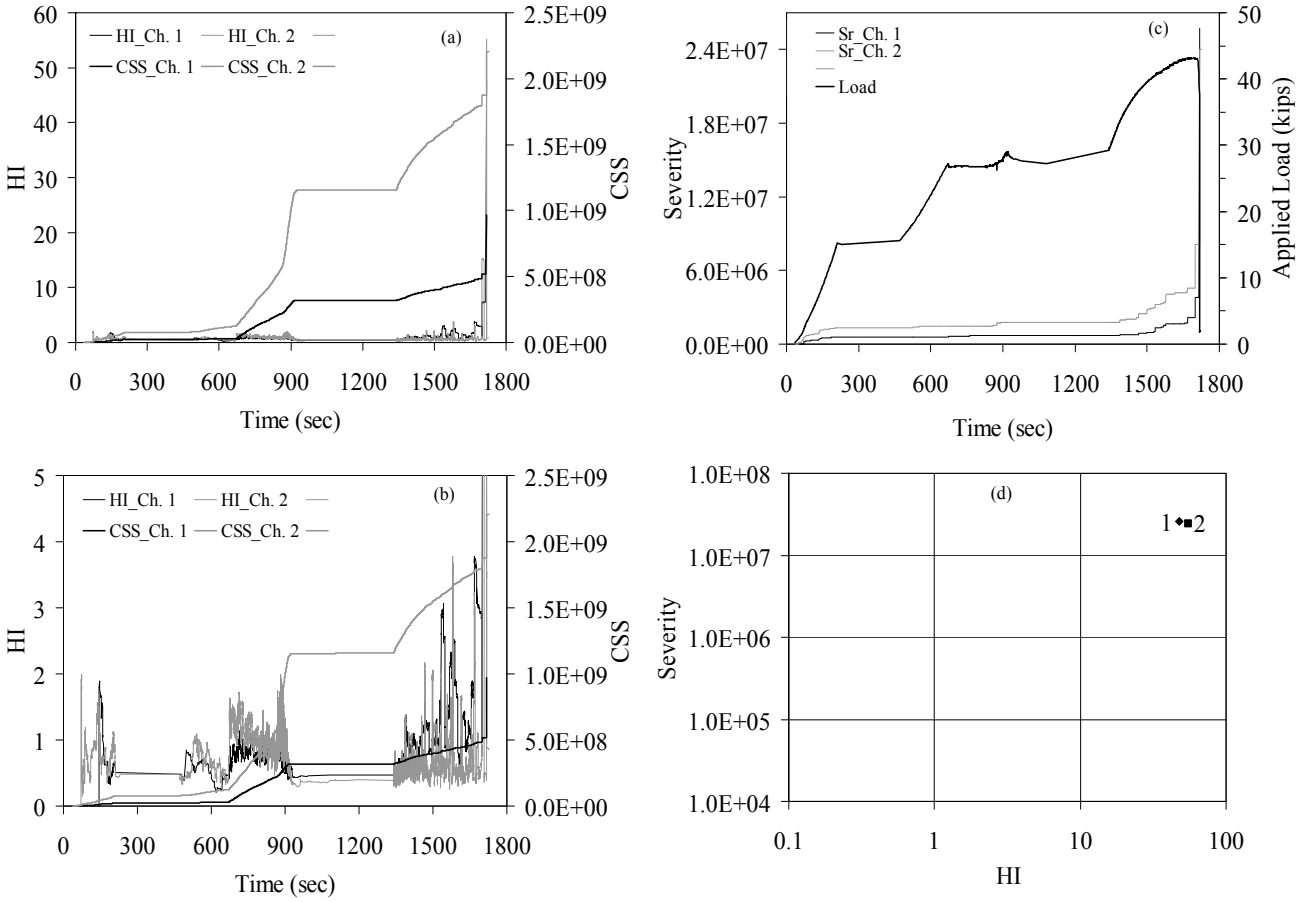

Figure 7-16 Intensity analysis for steel rebar 4. (a) Historic index as a function of time. The plot of the cumulative signal strength is superimposed. (b) Magnified portion of plot (a). (c) Severity index as a function of time. The plot of the applied load is superimposed. (d) Intensity chart.

7.4 DISCUSSION OF RESULTS

Four steel rebars under tension were monitored using AE technique. AE parameters such as signal counts, amplitude, and cumulative energy were considered. The behavioral patterns of a steel rebar are clearly explained with the help of a stress-strain curve, stating the elastic plateau, plastic region, strain hardening comparing to the results obtained from the signal counts, cumulative energy, amplitude, and risetime. All the rebars having same loading protocol, behaves structurally identical. PA did not provide any information regarding the onset of yield in the rebar specimens 1, and 2. However, in the case of rebar specimens 3 and 4, the cumulative energy plot helped in identifying the onset of yield. But in case of specimen 4 the strain hardening in the rebar specimen was clearly depicted by PA. The use of AE in comparison with load profile allowed checking for Kaiser Effect and felicity effect which proved to be a useful tool for identification of failure criteria.

Contrary to PA, the IA with the help of HI clearly depicted the yield, strain hardening and rupture in all the rebar specimens. This establishes the superiority of IA over PA in the tensile testing of rebars. Using the maximum values from historic index and severity, intensity charts are plotted. The values of the intensity charts readily show the general trend to be followed. Development of standard intensity charts require experimentation with numerous samples, but since this work involved just a few specimens only, a tentative chart showing the intensity values clustering towards the top right- hand corner associated with events of high structural significance, while events associated with less structural significance concentrating near the bottom left could be suggested rather than a definite established chart. Figure 7-17 shows a tentative intensity chart based on the results obtained from the IA done on the experimentally tested steel rebars. The zones identified are proposed based on the structural response of the rebars. This chart is valid only for evaluating ASTM A615 steel rebars. The quantitative values of the intensity chart may also be biased by all AE activities generated from the friction between the rebar and the conical wedge grips. As such no generalization should be made. Finally, more definite zones can be obtained by carrying out experiments on a large number of specimens with similar loading conditions.

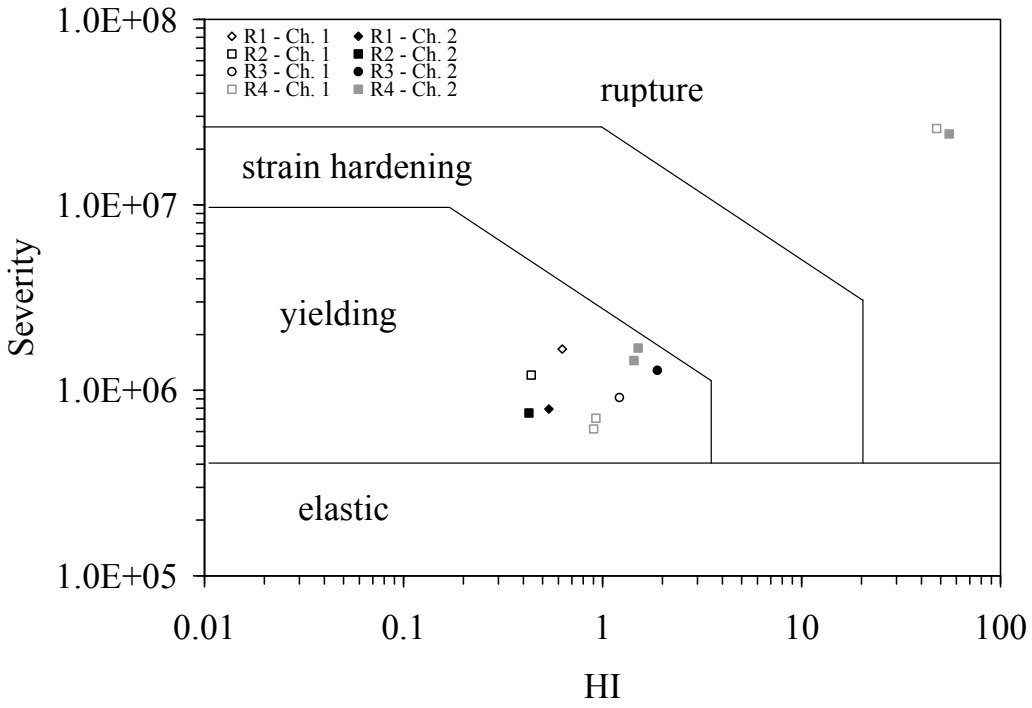

Figure 7-17 Tentative intensity chart zones proposed based on ASTM A615 steel rebars tested.

8.0 SUMMARY AND CONCLUSIONS

This thesis focused on a nondestructive evaluation approach based on acoustic emission to detect the onset, growth and propagation of different mechanism failures in reinforced concrete (RC) slabs retrofitted with carbon fiber reinforced polymers (CFRP). Nine reinforced concrete slab specimens were tested in the Watkins Haggart Structural Engineering laboratory at the University of Pittsburgh. The slabs were 50 in. (1270 mm) x 30 in. (762 mm) and 3 in. (76 mm) deep. Each slab was strengthened with a different CFRP strip geometry described by the ratio of CFRP width-to-CFRP spacing (b_f/s). By using a four-point bending test setup, the slabs were tested in a monotonic load-to-failure protocol under displacement control. An AE instrumentation suite from Physical Acoustics Corporation was used.

Three data analysis methods, namely parameter analysis (PA), intensity analysis (IA), and principal component analysis (PCA) were adopted. In the PA, AE features such as counts, amplitude, risetime, cumulative energy, peak frequency, and centroidal frequency were used to identify the AE source. IA was used for evaluating the conventional AE signal strength from slab specimens. Intensity charts were then generated from two main components: Historic index (HI) and Severity (S_r) values. PCA was used for dimensional reduction of AE data and to project the data vector into a new set of cartesian coordinates called the principal components.

Typically, results from PA demonstrated that flexural cracks near the laminates and debonding produce AE activities much higher in terms of signal amplitude and frequency range than eventual shear cracking. Although initially counterintuitive (shear cracks release greater energy than flexural cracks), this observation is explained by the crack locations. Flexural cracks are expressed at the CFRP-concrete interface and thus their emissions are transmitted directly by the CFRP strip on which the AE sensors are

mounted. Shear cracks, on the other hand, occur in the body of the concrete and do not affect the CFRP-concrete interface so significantly. The frequency and amplitude based AE source location plots seem promising in locating the source of AE events in the case of RC slabs experiencing CFRP debonding.

The results from IA reasonably signified the onset of damage propagation with the help of AE knee. A gradation of intensity points from the left end of the chart towards the right corner reflected the level of damage in the monitored region.

Although, the results from PCA were not satisfactory in identifying the location of cluster in the plot of the first two principal components for all the slab specimens, some degree of correlation between PA, IA, and PCA results were observed for discriminating the damage behavior between concrete cracking and CFRP debonding. Over all the results presented in this thesis showed that:

1. AE is well-suited for failure monitoring of RC structural elements retrofitted with CFRP;
2. Accurate AE data analyses identify different sources of damage (i.e. concrete cracking vs. CFRP debonding);
3. PA and IA can be used in-situ for real-time health monitoring of structural systems provided a higher number of sensors are deployed; and
4. PCA shows promising results but requires further study in this application.

Finally, a short term project was focused on AE monitoring of unbounded rebars subjected to quasi-static tensile cyclic loading. Four steel rebar specimens were tested with the aim of identifying and discriminating elastic, yielding, strain hardening and necking regions by means of AE. The AE instrumentation suite used for this testing was identical to that used in the case of CFRP slab specimens. The PA and IA were adopted to analyze the AE data. The Kaiser effect was observed in all specimens. The results from PA were reasonably efficient in identifying the elastic, yielding, and strain hardening regions typically observed during tensile deformation of a rebar. The results from IA stand as a supporting output for the observations made by PA. The intensity points satisfactorily reflected the degree of AE activity in the monitored region from the intensity charts.

8.1 FUTURE WORKS

The following are a few recommendations made for future works in structural health monitoring of the RC slabs retrofitted with CFRP and steel rebars using acoustic emission:

1. Additional testing and data analysis can provide validation and further characterization of damage mechanisms that can be utilized for real-time classification of events during AE monitoring.
2. Prior to field implementation RC elements subject to fatigue loads should be investigated.
3. Testing arrangement including sensor attached on both the CFRP and the concrete soffit should be carried out.

BIBLIOGRAPHY

Aidoo, J. (2004) "*Flexural Retrofit of Reinforced Concrete Bridge Girders Using Three CFRP Systems"*, Ph.D. Dissertation, Department of Civil and Environmental Engineering, University of South Carolina, 197 pp.

Akuthota, B., Hughes, D., Zoughi, R., Myers, J., and Nanni, A. (2004) "Near-field microwave detection of disbond in fiber reinforced polymer composites used for strengthening concrete structures and disbond repair verification", *ASCE Journal of Materials in Civil Engineering*, Vol. 16, No. 6, pp540-546.

American Concrete Institute (ACI) Committee 440 (2002) *ACI 440.2R-02 "Guide for the Design and Construction of Externally Bonded FRP Systems for Strengthening Concrete Structures"*, 45pp.

American Society for Testing and Materials (ASTM) E 1316 - 05, Section – B "*Standard Terminology for Nondestructive Testing*".

American Society for Testing and Materials (ASTM) E 2075-05, "*Standard Practice for Verifying the Consistency of AE-Sensor Response Using an Acrylic Rod*".

American Society for Testing and Materials (ASTM) A 615-07, "*Standard Specification for Deformed and Plain Carbon-Steel Bars for Concrete Reinforcement*".

Bastianini, F., Di Tommaso, A., Pascale, G. (2001) "Ultrasonic Nondestructive Assessment of Bonding Defects in Composite Structural Strengthenings", *Composite Structures*, Vol. 53, pp463-467.

Brown, J. R., and Hamilton, H. R. III. (2003) "NDE of Fiber-Reinforced Polymer Composites Bonded to Concrete using IR Thermography", *Proceedings of the SPIE*, 5405 – Thermosense XXVI, Vol. 5405, pp414-424.

Buyukozturk, O., Park, J., and Au, C. (2003) "NDE of FRP Confined Concrete using Microwaves", *International Symposium Nondestructive Testing in Civil Engineering*, Berlin, Germany, 2003. http://www.ndt.net/article/ndtce03/papers/v085/v085.htm

Buyukozturk, O., Gunes, O., and Karaca, E. (2004) "Progress on Understanding Debonding Problems in Reinforced Concrete and Steel Members Strengthened Using FRP Composites", *Journal of Construction and Building Materials*, Vol 18, pp. 9-19.

Carpinteri, A., Lacidogna, G., and Paggi, M. (2007) "Acoustic emission monitoring and numerical modeling of FRP delamination in RC beams with non-rectangular cross-section", *Journal of Materials and Structures*, Vol. 40, pp553–566.

Chen, H-L., Wissawapaisal, K. (2000) "Study of acoustic surface waveguides on reinforced concrete slabs", *Journal of Nondestructive Evaluation*, Vol. 19, No. 4, pp129-140.

Colombo, S., Main, I.G., Forde, M.C. (2003) "Assessing damage of reinforced concrete beam using "b - value" analysis of acoustic emission signals", *ASCE Journal of Materials in Civil Engineering*, Vol. 15, No. 3, pp280-286.

Ekenel, M., Stephen, V., Myers, J. J., and Zoughi, R. (2004) "Microwave NDE of Reinforced Concrete Beams Strengthened with CFRP Laminates Containing Surface Defects and Tested under Cyclic Loading", 16th World Conference on Nondestructive Testing, Montreal, Canada. http://www.ndt.net/article/wcndt2004/pdf/civil_structures/90_myers.pdf

Fowler, T.J., Blessing, J.A., Conslisk, P.J., and Swanson, T.L. (1989) "The MONPAC System", *Journal of Acoustic Emission*, Vol. 8, No. 3, pp1-8.

Fowler, T.J., Blessing, J.A., and Strauser, F.E. (1992) "Intensity analysis", *Proceedings of 4th International Symposium on Acoustic emission from Composite materials*, ASNT, Columbus Ohio, pp16-27.

Giurgiutiu, V., Harries, K.A., Petrou, M.F., Bost, J., Quattlebaum, J. (2003) "Disbond detection with piezoelectric wafer active sensors in RC structures strengthened with FRP composite overlays", *Journal of Earthquake engineering and Engineering Vibration*, Vol. 2, No.2, pp213-224.

Godinez-Azcuaga, V. F., Gostautas, R. S., Finlayson, R. D., and Miller, M. (2004) "Nondestructive Evaluation of FRP Wrapped Concrete Columns and Bridges", *Proceedings of Structural Materials VI- An NDT Conference*, Buffalo, NY, pp139-146.

Gostautas, R.S., Ramirez, G., Peterman, R.J., and Meggers, D. (2005) "Acoustic emission monitoring and analysis of glass fiber-reinforced composites bridge decks", *ASCE Journal of Bridge Engineering*, Vol. 10, No. 6, pp713-721.

Gros, X. E., and Takahashi, K. (2000) "Non-destructive Characterization of Delaminated Areas at Interfaces Between Plies in Carbon Fiber/epoxy Laminates with Foucault Currents", *Composite Interfaces*, Vol. 7, No. 3, pp. 177-192.

Grosse, C.U., Reinhardt, H.W., Finck, F. (2003) "Signal-based acoustic emission techniques in civil engineering", *ASCE Journal of Materials in Civil Engineering*, Vol. 15, No. 3, pp274-279.

Halabe, U.B., Vasudevan, A., Klinkhachorn, P., Gangarao, H.V.S. (2007) "Detection of subsurface defects in fiber reinforced polymer composite bridge decks using digital infrared thermography", *Journal of Nondestructive Evaluation* Vol. 22, Nos. (2–3), pp155–175.

Hellier, C. (2001) "Handbook of Nondestructive Evaluation", McGraw-Hill Professional.

Huguet, S., Godin, N., Gaertner, R., Salmon, L., Villard, D. (2002) "Use of acoustic emission to identify damage modes in glass fiber reinforced polyester", *Composites Science and Technology*, Vol. 62, No. 10, pp1433-1444.

Jackson, D., Islam, M., Alampalli, S. (2000) "Feasibility of evaluating the performance of fiber reinforced plastic (FRP) wrapped reinforced concrete columns using ground penetrating radar and infrared

thermography techniques", *Structural Materials Technology – An NDT Conference*. Atlantic City, NJ, pp390-395.
http://books.google.com/books?id=uczkKDKn5HYC&pg=PA390&lpg=PA390&dq=nondestructive+evaluation+of+frp+wrapped+concrete+columns+and+bridges&source=web&ots=Y4k83vdQgV&sig=z1Z6yOYdVbGrQze-aQkl_jkac38

Kaiser, J. (1950) "*Untersuchungen uber das Auftreten Geraushen beim Zugversuch*" (An Investigation into the Occurrence of Noises in Tensile Tests), Ph.D. dissertation, Technische Hochschule, munich, Germany.

Karbhari, V.M. (2001) "Materials considerations in FRP rehabilitation of concrete structures", *Journal of Materials in Civil Engineering*, Vol. 13, No. 2, pp90-97.

Kim, J.Y., De Flaviis, F., Jofre, L., and Feng, M. Q. (2001) "Microwave-Based NDE of FRP-Jacketed Concrete Structures", *International SAMPE Symposium and Exhibition (Proceedings)*, Vol. 46, pp439-450.

Kim, S.D., In, C.W., Cronin, K.E., Sohn, H., Harries, K.A. (2007) "A reference-free NDT technique for debonding detection in CFRP strengthened RC structures", *ASCE Journal of Structural Engineering*, Vol. 133, No. 8, pp1080-1091.

Maji, A., and Sahu, R. (1994) "Acoustic emissions from reinforced concrete", *Experimental Mechanics*, Vol. 34, No. 4, pp379–388.

Manson, G., Worden, K., Holford, K., and Pullin, R. (2001) "Visualization and dimension reduction of acoustic emission data for damage detection", *Journal of Intelligent Material Systems and Structures*, Vol. 12, pp529–536.

Mirmiran, A., Shahawy, M., and El Echary, H. (1999) "Acoustic emission monitoring of hybrid FRP-concrete columns", *ASCE Journal of Engineering Mechanics*, Vol. 125, No. 8, pp899-905.

Mirmiran, A., Wei, Y. (2001) "Damage assessment of FRP-encased concrete using ultrasonic pulse velocity", *ASCE Journal Engineering Mechanics*, Vol. 127, No. 2, pp126-135.

Mizutani, Y., Nagashima, K., Takemoto, M., Ono, K. (2000) "Fracture mechanism characterization of cross-ply carbon-fiber composites using acoustic emission analysis", *NDT & E International,* Vol. 33, No. 2, pp101-110.

Mukhopadhyay, C.K., Kasivishwanathan, K.V., Jayakumar, T., Baldev Raj. (1993) "Acoustic Emission during tensile deformation of annealed and cold-worked AISI type 304 austenitic stainless steel", *Journal of Materials Science*, Vol. 28, pp145-154.

Mukhopadhyay, C.K., Ray, K.K., Jayakumar, T., Baldev Raj. (1998) "Acoustic emission from tensile deformation of unnotched and notched specimens of AISI type 304 stainless steels", *Journal of Materials Science and Engineering*, Vol. A225, pp98-106.

Mustapha, F., Manson, G., Pierce, S.G., and Worden, K. (2005) "Structural Health Monitoring of an Annular Component using a Statistical Approach", *Strain*, Vol. 41, pp117-127.

Mustapha, F., Worden, K., Pierce, S.G., and Manson, G. (2007) "Damage detection using stress waves and multivariate statistics: an experimental case study of an aircraft component", *Strain*, Vol. 43, No. 1, pp47-53.

Naik, T.R., Malhotra, V.M., and Popovics, J.S. (2004) "The ultrasonic pulse velocity method in nondestructive testing of concrete" Chapter 8, Malhotra, V.M., CRC Press; Carino, NJ.

Nokes, J. P., and Hawkins, G. F. (2001) "Infrared Inspection of Composite Reinforced Concrete Structures", Ohio DOT, OH, 2001. http://www.dot.state.oh.us/research/2001/Structures/14688-FR.pdf

Oehlers, D.J. (2005) "Generic Debonding Mechanisms in FRP Plated Beams and Slabs", *Proceedings of the International Symposium on Bond Behavior of FRP in Structures (BBFS)*, Hong Kong, International Institute for FRP in Construction, pp35-44.

Oehlers, D.J. (2006) "Ductility of FRP plated flexural members", *Cement and Concrete Composites*, Vol. 28, No. 10, pp898-905.

Physical Acoustics Corporation (PAC), (2005) "*μDiSP with AEwin user's manual*", Rev. 3, Princeton Junction, NJ.

Qi, G. (2000) "Wavelet-based AE characterization of composite materials", NDT & E International, Vol. 33, No. 3, pp133–144.

Ramanathan, K., and Harries, K.A. (2008) "Influence of FRP width-to-concrete substrate width (b_f/b) on bond performance of externally bonded FRP systems" *Proceedings of 12th International Conference on Structural Faults and Repair*, Edinburgh.

Ramanathan. K. (2008) "*Influence of FRP width-to-spacing ratio on bond performance of externally bonded FRP systems on one way concrete slabs",* MS Thesis, Department of Civil and Environmental Engineering, University of Pittsburgh, Pittsburgh, PA, 151pp.

Rippengill, S.,Worden, K., Holford, K.M., and Pullin, R. (2003) "Automatic classification of AE patterns", *Strain*, Vol. 39, pp31-41.

Rizzo, P., and Lanza di Scalea, F. (2001) "Acoustic Emission Monitoring of Carbon-Fiber-Reinforced-Polymer Bridge Stay Cables in Large-Scale Testing", *Experimental Mechanics*, Vol. 41, No. 3, pp. 282-290.

Rose, J.L. (1999) "Ultrasonic Waves in Solid Media", Cambridge University Press, NY, 454pp.

Schechinger, B., Vogela, T. (2006) "Acoustic emission for monitoring a reinforced concrete beam subject to four-point-bending", *Journal of Construction and Building Materials*, Vol. 21, No. 3, pp483-490.

Sharma, S. (1996) "Applied Multivariate Techniques*"*, John Wiley, New York, USA.

Shih J. K. C., Tann, D. B., Hu, C. W., Delapk, R., and Andreou, E., (2003) "Remote Sensing of Air Blisters in Concrete-FRP Bond Layer Using IR Thermography", *International Journal of Materials and Product Technology*, Vol. 19, Nos. 1-2, pp174-187.

Shull, P. (2002) "Nondestructive evaluation: theory, techniques, and applications", Edited by Peter J. Shull, New York: M. Dekker.

Stephen, V., Kharkovsky, S., Nadakuduti, J., and Zoughi, R. (2004) "Microwave Field Measurement of Delaminations in CFRP Concrete Members in a Bridge", *Proceedings of the World Conference on Nondestructive Testing (WCNDT)*, 5pp, Montreal, Canada.

Published Work Stemming from this Research

Degala, S., Rizzo, P., Ramanathan, K., and Harries, K.A. (2008). "Acoustic Emission Monitoring of CFRP Reinforced Concrete Slabs," *Construction Buildings and Materials*, submitted.

Degala, S., Rizzo, P., Ramanathan, K., and Harries, K.A. (2008). "Structural Health Monitoring of CFRP Reinforced Concrete by Acoustic Emission," *5th International Conference on Advanced Composite Materials in Bridges and Structures*, ACMBS-V, Manitoba, Canada, submitted.

Degala, S., Rizzo, P., Ramanathan, K., and Harries, K.A. (2008). "Acoustic Emission Monitoring of FRP Reinforced Concrete," *Proceedings of SPIE's 15th Annual International Symposium on Smart Structures and Materials – Sensors and Smart Structures Technologies for Civil, Mechanical and Aerospace System*, San Diego, USA, to appear.